INVESTIGATING SMALL-SCALE MICROPHYSICAL AND DYNAMICAL MECHANISMS WITHIN A WINTER OROGRAPHIC SNOWFALL EVENT AND A SPRING SQUALL LINE INTERACTING WITH MOUNTAINS

by

JOSHUA DANIEL AIKINS

B.S., The Pennsylvania State University, 2008

A thesis submitted to the

Faculty of the Graduate School of the

University of Colorado in partial fulfillment

of the requirement for the degree of

Doctor of Philosophy

Department of Atmospheric and Oceanic Sciences

2018

This thesis entitled:
Investigating Small-Scale Microphysical and Dynamical Mechanisms within A Winter Orographic Snowfall Event and A Spring Squall Line Interacting With Mountains
written by Joshua Daniel Aikins
has been approved for the Department of Atmospheric and Oceanic Sciences.

_____

Prof. Katja Friedrich

_____

Prof. John Cassano

Date:_____

The final copy of this thesis has been examined by the signatories, and we find that both the content and the form meet acceptable presentation standards of scholarly work in the above mentioned discipline.

Aikins, Joshua Daniel (Ph.D., Department of Atmospheric and Oceanic Sciences)
Investigating Small-Scale Microphysical and Dynamical Mechanisms within A Winter Orographic Snowfall Event and A Spring Squall Line Interacting With Mountains
Thesis directed by Prof. Katja Friedrich

Abstract

The first part of this dissertation investigates natural small-scale microphysical and dynamical mechanisms identified in a winter orographic snowstorm over the Sierra Madre mountain range of Wyoming during the AgI Seeding Clouds Impact Investigation (ASCII). A turbulent shear layer was observed in a cold post-frontal environment that was created by a mid-level cross-barrier jet riding over a decoupled Arctic air mass. Similar turbulent shear layers have been observed over blocked low-level air masses along coastal maritime mountain ranges, but little research has focused on inland continental ranges. The multi-instrument analysis suggests 1) shear-induced turbulent overturning cells do exist over cold continental mountain ranges like the Sierra Madre, 2) the presence of cross-barrier jets favor these turbulent shear zones, 3) this turbulence is a key mechanism in enhancing snow growth, and 4) snow growth enhanced by turbulence primarily occurs through deposition and aggregation in these cold (< -15°C) post-frontal continental environments.

The second part of this dissertation utilizes a high-resolution observational network from the Integrated Precipitation and Hydrology Experiment (IPHEx) to document the orographic modification of a prefrontal squall line that passed over the southern Appalachian Mountains. Little previous research exists documenting

the interaction of squall lines with mountainous terrain, especially observationally, so this study is one of the first. The squall line studied was embedded within an Atmospheric River (AR), where southerly low-level moisture transport was impeded by the southern Appalachian Mountains, favoring rapid fallout of precipitation on its southeastern slopes. A growing research interest exists in the role ARs play in extreme precipitation events over the eastern US, and this study highlights the importance of small-scale terrain and convective features within AR environments in generating heavy rainfall.

The third part of this dissertation describes i) my first-of-its-kind NOAA G-IV tail Doppler radar analysis over the Pacific Ocean aimed at documenting cloud and precipitation structures within an offshore AR during the CalWater-2 field project, and ii) my role in collecting ground-breaking radar data during the SNOWIE field project that is being used to document the formation and fallout of snow initiated by man-made airborne glaciogenic cloud seeding.

Acknowledgements

I want to thank my parents for their motivation and support of me following my dreams, no matter the cost. My father received his doctoral degree while raising me and my two siblings, and he was the first in our family to receive such a high degree. This has motivated me to continue what he started, although I don't know how he did it with three kids!

I want to thank Dr. Ken Davis, Dr. Natasha Miles, and Dr. Elizabeth Boyer from The Pennsylvania State University for giving me my first research experiences and spurring my interest in instrumentation and observations. My experience working with Picarro gas analyzers (carbon cycle) and PARSIVEL disdrometers (hydrology) may have been used for vastly different scientific areas of study, but it has bolstered my passion for working with instrumentation and the real-world observations they provide. Additionally, this experience has helped me with my graduate field work.

I want to thank Ann Thorne from the National Oceanic and Atmospheric Administration (NOAA) Earth Systems Research Laboratory (ESRL) for providing so much support during my undergraduate internship and graduate school work. Her kind and caring personality was refreshing while working at NOAA ESRL over the summer of 2011 as a young undergraduate intern. She was also vital in securing my graduate school funding for the second half of my PhD work. Her dedication to students is unparalleled.

I want to thank my academic/research advisor, Dr. Katja Friedrich, for supporting me in my graduate studies and allowing me to work with instruments in the field. Dr. Friedrich allowed me to pursue my passion for snow and mountains by doing research on the incredible dataset from the AgI Seeding of Clouds Impact Investigation (ASCII). Additionally, she allowed me to be the lead University of Colorado graduate student in the field for the Seeded and Natural Orographic Wintertime Clouds: The Idaho Experiment (SNOWIE) field project, where I gained valuable experience operating research radars and maintaining surface in-situ instrumentation in harsh winter conditions. I was also able to practice my public speaking through a live television interview with The Weather Channel while deployed during SNOWIE. Additionally, she allowed me to set up and maintain her instrumentation at the Niwot Ridge Long-Term Ecological Research Station at 10,000-11,000 ft elevation in the Rocky Mountains of Colorado. My graduate work with Dr. Friedrich also allowed me to learn a programming language (IDL), which has spurred my interest in scientific data visualization, a skill I can use in any private or public sector job.

I want to thank my fellow University of Colorado Atmospheric and Oceanic Sciences (ATOC) graduate students, especially Josh Pettit, Dr. Rochelle Worsnop, Dr. Evan Kalina, Chris Maloney, Victoria Hartwick, Dr. Anondo Mukherjee, Dr. Brian Vanderwende, and Dr. Clara St. Martin, for providing captivating conversations about life and research and the numerous adventures. Your friendship and support has made graduate school one of the best years of my life.

Finally, I would like to thank my wife, Ruth Aikins, for supporting me as I navigated graduate school 1800 miles from our family. I know moving away from home and venturing into the “Wild Wild West” of Colorado was the scariest experience you’ve ever had, but I’m so grateful that you stuck it out with me as I achieved my professional degree and followed my dreams. Your love and support was unwavering. I couldn’t have done it without you!

Table of Contents

List of Figures

1 Introduction

Mountains are not just great for screensaver pictures, they are vital to the water supply of millions of humans on Earth. Mountains modify the air flowing through the atmosphere, creating orographic lift along windward slopes, downslope flow along leeward slopes, and sometimes even exciting gravity waves throughout the depth of the troposphere. This modification of the ambient atmosphere leads to enhancement and suppression of precipitation at the surface, usually over rather short distances (1's to 10's km). Additionally, mid-latitude mountains typically extend above the freezing level and store this precipitation as snowpack. This snowpack builds up over the colder winter months and then fills rivers and aquifers at lower elevations downstream during the warmer summer months as the snowpack melts.

The mountainous region of the western United States (US) is one location that relies heavily on mountain snowpack, and rising populations and a warming climate are threatening this water supply (Bureau of Reclamation 2016). Orographic winter snowfall over the western US comprises over 60% of the annual precipitation for some mountain ranges (Serreze et al. 1999), with regional differences in snowpack accumulation and melt patterns (Trujillo and Molotch 2014). Warming temperatures allows more precipitation to fall as rain rather than snow, which results in immediate runoff downstream rather than being stored in mountain snowpack for later use. Additionally, the smaller snowpack volume that does build up melts earlier (e.g., Stewart et al. 2005), leaving less runoff later in the

summer months when reservoir supplies are dwindling. Reduced runoff also impacts hydropower production, a renewable energy source that helps keep consumer power costs low. The earlier shift in peak runoff and reduced runoff in the summer leaves less hydropower production in the late summer months when peak power demand occurs for cooling. Population increases boost the water and power demands, which further exacerbates the problem and has lead to localized studies attempting to quantify the impacts of these water supply changes and address adaptation strategies (e.g., Bardsley et al. 2013). Although the snowpack changes caused by warming are fairly understood, changes in future precipitation is less understood.

Due to the importance of mountain snowpack in the western US, understanding the natural dynamical and microphysical mechanisms that influence snowfall over mountain barriers is vital. However, limited operational observations within the mountainous western US make this difficult. A key observational facility useful for observing precipitation and airflow in complex mountainous terrain is scanning weather radar. Operational NEXRAD radars in the western US tend to be positioned within flat terrain or valleys near major cities, which leaves large portions of the region largely un-observed due to beam blockage (Figure 1.1). This has lead to the partial dependence on operational numerical weather models to provide guidance on the timing and distribution of precipitation within the mountainous western US (e.g., Wetzel et al. 2004), but the coarse resolution of global (10+ km) and regional models (3+ km) does not fully capture the small-scale

variability caused by interactions with complex mountainous terrain (e.g., Cosma et al. 2002; Gowan et al. 2018).

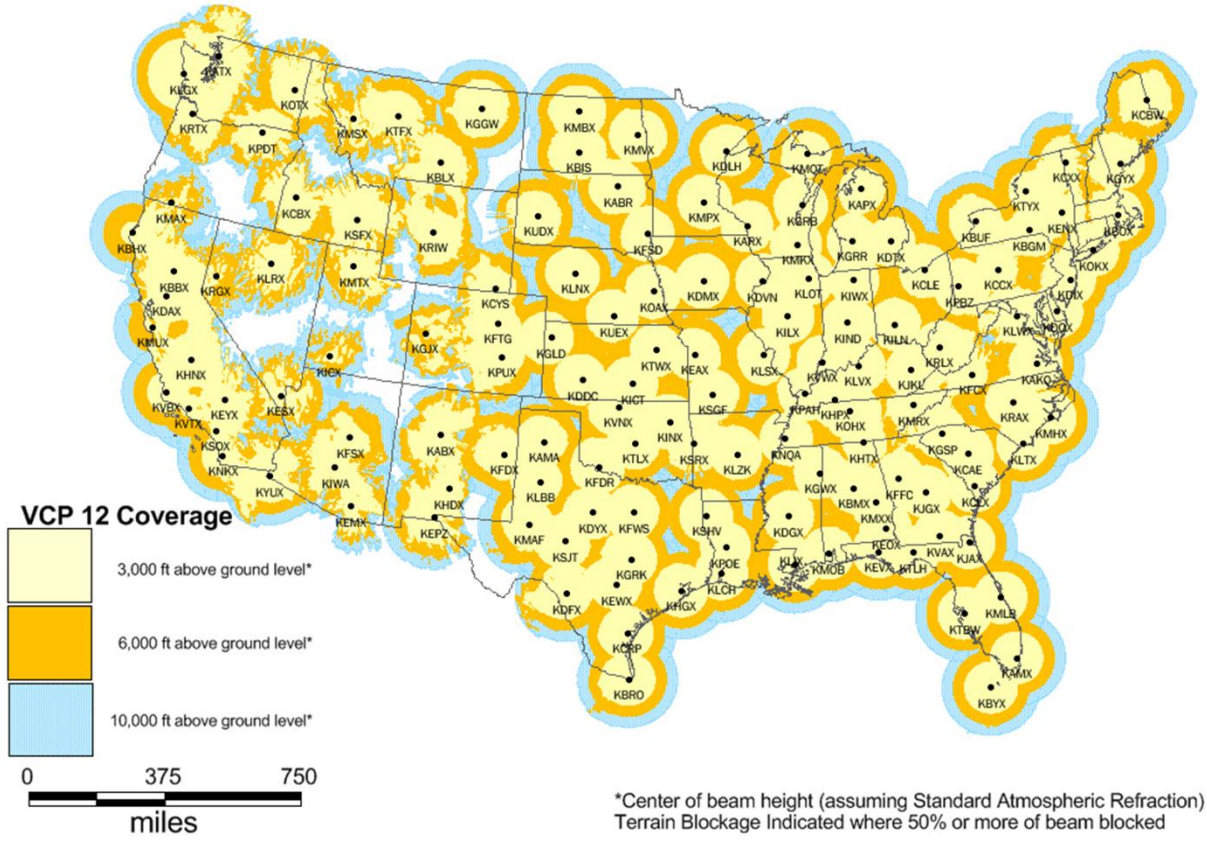

Figure 1.1: Map of operational radar coverage from the US NEXRAD network below 10000 ft (blue), 6000 ft (orange), and 3000 ft (yellow). Available online at https://www.roc.noaa.gov/WSR88D/Maps.aspx.

Recent coordinated research field experiments have revealed small-scale dynamical and microphysical mechanisms at play within orographic precipitation systems, but additional observations are needed. Houze and Medina (2005) identified a terrain-sloping layer of shear turbulence as a mechanism that enhances precipitation fallout upwind of the Oregon Cascades and European Alps in stable environments with blocked or partially retarded cross-barrier orographic flow (Figure 1.2). This turbulent shear layer facilitated rapid particle growth through

enhanced liquid water production and subsequent riming of large aggregate snowflakes just above the melting layer, which allowed faster fallout of precipitation upwind of the mountain, moisture that may have been advected farther downstream without the presence of this turbulent shear layer. Medina and Houze (2015) further investigated the importance of small-scale precipitation cells associated with shear-induced turbulence upwind of the Sierra Nevada Mountains. These studies have indicated the importance of turbulent overturning motions in allowing enhanced hydrometeor growth, but they have focused on more maritime coastal regions where increased moisture fluxes and mixed phase clouds are observed with warmer cloud bases.

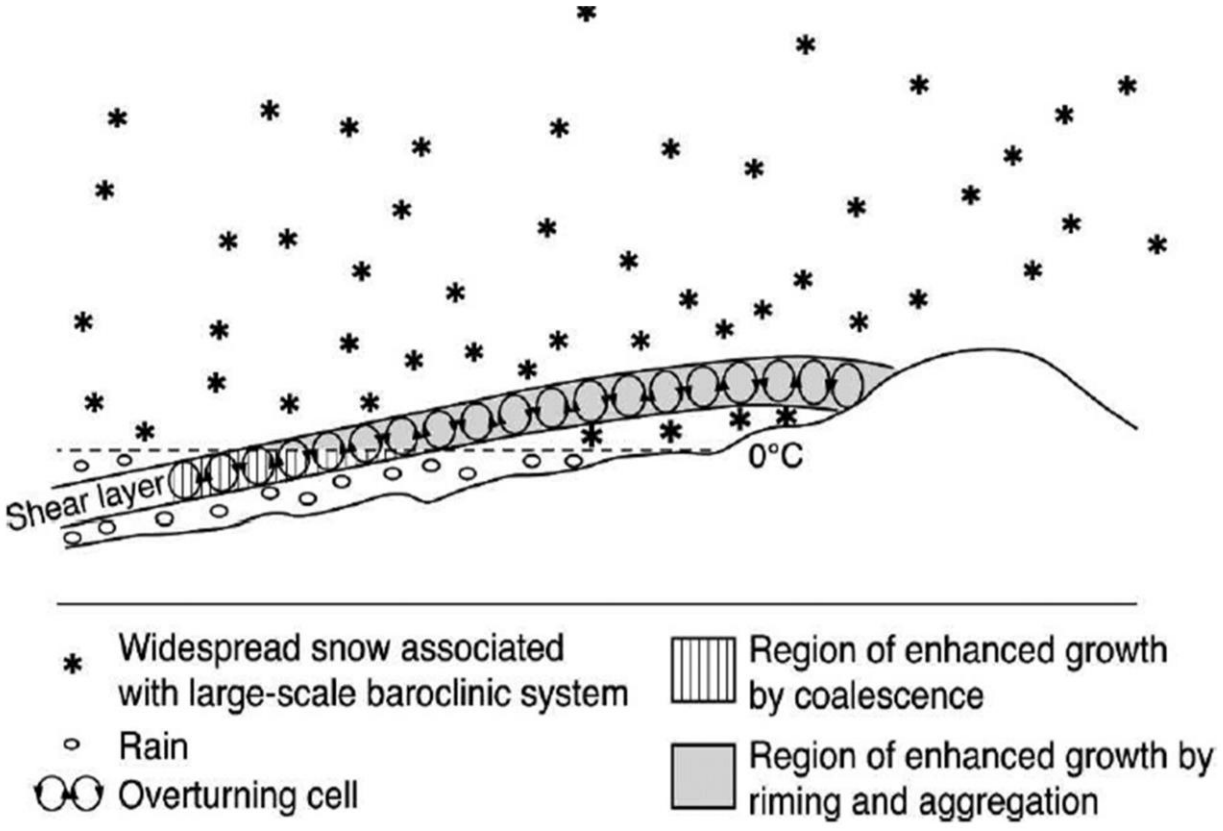

Figure 1.2: Conceptual model of the dynamical and microphysical mechanisms responsible for the orographic enhancement of precipitation during storms with a turbulent shear layer

atop a partially blocked low-level airflow. This figure is figure 22 of Houze and Medina (2005).

A motivation for the work presented in the first part of this dissertation is whether similar shear-induced turbulent cells modify snowfall within a colder continental mountain range of Wyoming, and if so through what microphysical mechanism does this occur. Additionally, these small-scale turbulent motions are too small to be observed within operational weather models, but their modification of microphysical growth mechanisms may be something that can be parameterized. Thus, identification of these turbulent cells is important for improving mesoscale weather model snowfall prediction over the mountains of the western US. Improved models could also reveal important changes in future precipitation over the western US in a warming climate, which would help in planning adaptation strategies.

The work presented in the second part of this dissertation focuses on understanding the small-scale impacts that mountains have on a warm-season mesoscale convective system (MCS). Specifically, I focused on the orographic modification of a convective squall line by the southern Appalachians during the spring of 2014.

There is an abundance of literature that has documented the kinematics of MCSs (Houze 2004 and Trapp 2013 are great resources), but most of this research has focused on MCS processes over regions devoid of mountainous terrain. Squall lines are a commonly observed MCS in the central and eastern US, which typically consist of a linear region of multicellular convection followed by a trailing stratiform region (Figure 1.3), although leading and parallel stratiform structures have been

observed in different wind environments (Parker and Johnson 2000). Squall lines form as initial convection creates mesoscale downdrafts that carry precipitation-cooled mid-tropospheric air to the surface, thus creating a surface cold pool that propagates outward from the storms as a gust front. As the gust front moves through unstable environments, new convection is generated along its leading edge as the denser air within the cold pool lifts warm moist low-level air ahead of it. Eventually old convective cells move rearward of the advancing gust front and weaken, creating the trailing stratiform precipitation region. The strong convective updrafts along the gust front set up a system-relative front-to-rear inflow of warm moist air due to the typically rearward-tilted updraft (Figure 1.3a). The initiation of new convection along the gust front and its subsequent convective downdraft continue to feed the surface cold pool and drive the gust front forward. Squall lines rely on a balance between the surface cold pool strength and ambient low-level (0-3 km) wind shear perpendicular to the squall line movement (Rotunno et al. 1988; Weisman and Rotunno 2004). Longer-lived squall lines are generally observed in conditions with increased shear due to the increased low-level inflow and more vigorous updraft along the leading edge of the cold pool. A meso-low pressure region typically forms at mid-levels within the squall line due to latent heat release by the convective updraft, which lies above the meso-high created by the cold pool at the surface (Figure 1.3a). Together, this pressure pattern creates a mid-level rear inflow jet that brings drier mid-level environmental air into the trailing stratiform rain region, thus favoring increased evaporation and a stronger cold pool (e.g., Smull and

Houze 1987). This rear-inflow jet frequently descends to the surface within the cold pool (Figure 1.3a), and it can create severe surface straight-line winds within bow echo segments (e.g., Przybylinski 1995). Because of severe winds, flooding rains, and lightning frequently associated with squall lines, understanding what drives them is important for the safety of human lives and property.

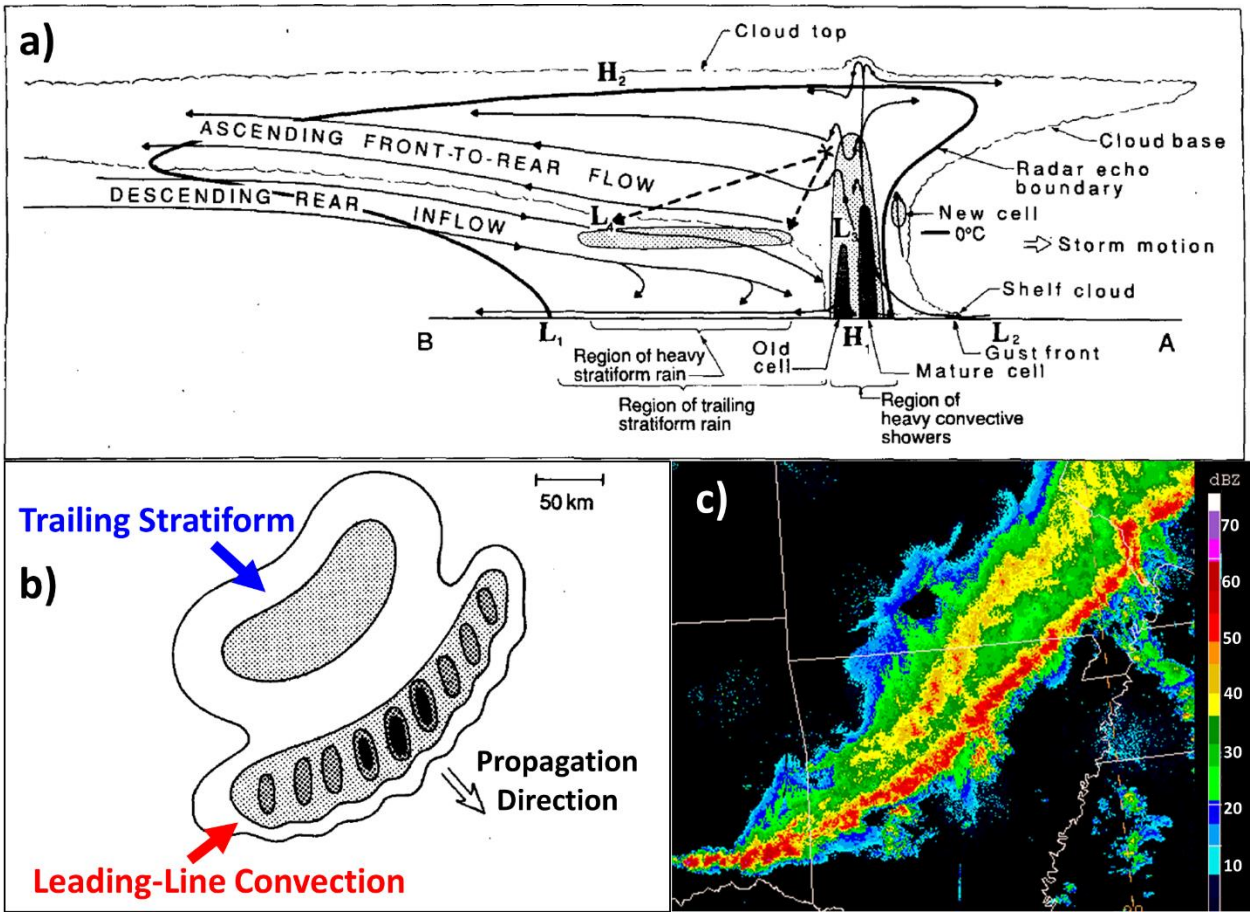

Figure 1.3: a) A vertical cross-section conceptual model of a squall line with a trailing stratiform region, oriented perpendicular to the convective line (parallel to its propagation direction). a) is from figure 1 of Houze et al. (1989). b) A horizontal schematic of a symmetric squall with the leading line convection and trailing stratiform regions identified, adapted from figure 7 of Houze et al. (1990). In both a) and b), darker shading indicates increased radar reflectivity. An example mosaic radar reflectivity image of a squall line over Arkansas is shown in c). The reflectivity colorbar is on the right in c). See text for further descriptions.

Recent studies have started to document MCS interactions with mountainous terrain, but limited observations exist. Frame and Markowski (2006) and Letkewicz and Parker (2010, 2011) were the first to model squall line interactions with idealized mountain barriers, finding that squall line strength is generally enhanced on windward slopes, suppressed on leeward slopes, and re-invigorated by hydraulic jumps at the base of leeward slopes as long as favorable convective available potential energy (CAPE) exists both upwind and downwind of the mountain barrier (Figure 1.4). However, a preliminary 6-year analysis of actual squall lines interacting with the Appalachian Mountains (Keighton et al. 2007) showed that a majority of MCSs do not continue downwind of the higher terrain. Additionally, the only known research paper that used radar observations to document the orographic modification of a sub-tropical squall line with the mountains of Taiwan (Teng et al. 2000) showed the squall line dissipated as it moved over the higher terrain. These observational studies suggest that the mountains themselves may set up contrasting atmospheric environments upwind and downwind and thus create a physical barrier detrimental to the continued propagation of organized convection. However, additional observations are needed to improve our understanding of the small-scale interactions between complex mountainous terrain and the kinematics of MCSs. This has motivated the work presented in section 3 of this dissertation.

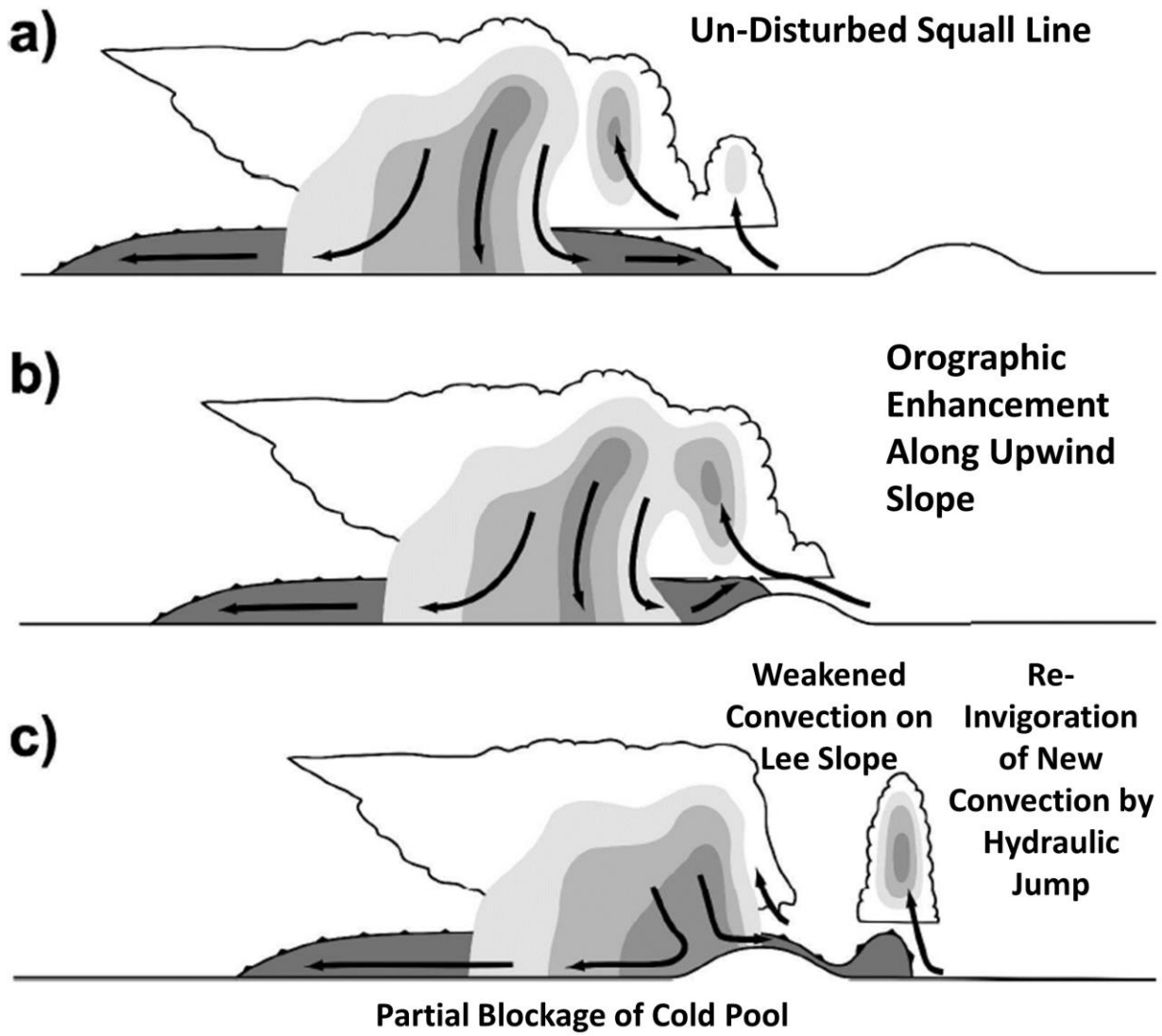

Figure 1.4: Schematic vertical cross-section diagram of a) a steady-state squall line before any terrain interaction, b) the squall line ascending an idealized mountain ridge, and c) a squall line descending the idealized mountain ridge with a hydraulic jump at the bottom of the slope resulting in enhanced lift and generation of a new convective line as the original convective line weakens. Shading indicates the rainwater field, roughly proportional to reflectivity, with darker shading indicating increased values. The cold pool is identified by the darkest grey shading, with the cold pool boundary identified by a bold black line with triangles. Black arrows indicate system-relative airflow. The main mechanisms affecting the squall line progression are identified by text in each panel. This figure is adapted from figure 28 of Frame and Markowski (2006).

2 Role of a Cross-Barrier Jet and Turbulence on Winter Orographic Snowfall

This chapter is adapted and reformatted from:

Aikins, J., K. Friedrich, B. Geerts, and B. Pokharel, 2016: Role of a Cross-Barrier Jet and Turbulence on Winter Orographic Snowfall. *Mon. Wea. Rev.*, **144**, 3277–3300, doi:10.1175/MWR-D-16-0025.1.

2.1 Abstract

Natural small-scale microphysical and dynamical mechanisms are identified in a winter orographic snowstorm over the Sierra Madre mountain range of Wyoming during an intensive observational period (IOP) from the AgI Seeding Clouds Impact Investigation (ASCII; January-March 2012). A suite of high-resolution radars, including a ground-based scanning X-band dual-polarization Doppler on Wheels radar, vertically pointing K_a-band Micro Rain Radar, and airborne W-band Wyoming Cloud Radar, and additional *in-situ* and remote sensing instruments are used in the analysis. The analysis focuses on a deep post-frontal period on 16 January 2012 (IOP2) when clouds extended throughout the troposphere and cloud liquid water was absent following the passage of a baroclinic front. A turbulent shear layer was observed in this post-frontal environment that was created by a mid-level cross-barrier jet riding over a decoupled Arctic air mass that extended above mountaintop. MRR and WCR observations indicate additional regions of turbulence aloft that favor rapid particle growth at upper-levels of the cloud. Plunging flow in the lee of the Sierra Madre was also observed during this

case, which caused sublimation of snow up to 20 km downwind. The multi-instrument analysis in this paper suggests 1) shear-induced turbulent overturning cells do exist over cold continental mountain ranges like the Sierra Madre, 2) the presence of cross-barrier jets favor these turbulent shear zones, 3) this turbulence is a key mechanism in enhancing snow growth, and 4) snow growth enhanced by turbulence primarily occurs through deposition and aggregation in these cold (< -15°C) post-frontal continental environments.

2.2 Introduction

In many mountainous regions on Earth, snowfall accounts for a substantial portion of the total annual precipitation and its local spatial distribution becomes increasingly important for hydro-meteorological applications such as evaluating flood risk, water availability, and hydropower production. Recent studies have shown that mesoscale and microscale dynamic and microphysical processes, which convert condensed water quickly and efficiently into precipitation, are becoming more important in understanding regional precipitation generation and distribution (e.g., Rotunno and Houze 2007; Garvert et al. 2007; Kirshbaum et al. 2007; Kumjian et al. 2014; Medina and Houze 2015).

Microscale shear dynamic instability found in frontal systems associated with baroclinic waves has been highlighted as one such dynamic process (Houze and Medina 2005, hereafter HM05; Medina and Houze 2015, hereafter MH15). These studies found that shear instability can produce so-called overturning cells, which are 1-5 km wide with updrafts of 1-3 m s^{-1}, when wind shear exceeds 10 m s^{-1} km^{-1}.

These updrafts can produce pockets of increased liquid water content (LWC), enhancing riming and coalescence and increasing aggregation through differences in fall velocity of forming and growing particles. These particles then grow rapidly and fall out quickly on windward slopes. HM05 identified overturning cells in terrain-sloping layers of shear turbulence in stable environments with blocked or partially retarded cross-barrier orographic flow below mountaintop in the Oregon Cascades and Alps. Medina et al. (2005) used model sensitivity studies to show that increased upwind stability, surface friction, mountain height, and pre-existing wind shear enhance this turbulent shear zone. MH15 further studied shear-induced turbulence in cyclones crossing the California Sierra Nevada. Shear-induced turbulence was found in storms with strong upstream winds and higher vertically-integrated cross- and along-barrier moisture fluxes. Similar cloud-top generating cells have also been identified (Rosenow et al. 2014; Kumjian et al. 2014; Plummer et al. 2014), but these overturning cells are more tied to convective instability rather than shear instability. Additionally, Geerts et al. (2011) observed snow growth within boundary layer turbulence on windward mountain slopes, but the aggregational growth mechanism suggested is only speculative. The lack of abundant observational and modeling research of the impacts of turbulence on microphysical processes is further motivation for this study.

Previous studies on shear instability have focused on large mountain ranges adjacent to large bodies of water with large moisture fluxes and mixed-phase precipitation. Cloud microphysical processes present in orographic environments

over inland mountain ranges were found to differ from coastal mountains, mainly due to the lower and warmer bases of coastal storm systems that favor riming and increased ice crystal concentrations through the rime splintering mechanism (Rauber 1992). Less riming is observed for inland mountain ranges, partly due the fact that water is removed from the atmosphere by upwind mountain ranges (Hindman 1986; Saleeby et al. 2011), but cloud liquid water has still been observed within regions where the condensate supply rate can exceed the diffusional growth rate of ice crystals (Rauber and Grant 1986). These regions were found to be near cloud-top, between cloud base and -10°C, and directly upwind and over the mountain crest where strong orographic lift is typically observed. Depositional and aggregational growth are the primary microphysical mechanisms within colder continental environments.

Do shear turbulence regions and overturning cells exist over continental mountain ranges with colder temperatures and reduced moisture fluxes? If so, do these overturning cells enhance precipitation? If enhancement occurs, through what microphysical mechanism(s) does it occur? This study aims to answer these questions by investigating the role of shear instability over the Sierra Madre mountain range in southern Wyoming, a small inner-mountain range with lower advected moisture fluxes.

The dataset used in this paper was collected during the AgI Seeding Clouds Impact Investigation (ASCII; Geerts et al. 2013). ASCII took place January-March 2012 and was designed to observe changes in cloud microphysical properties due to

ground-based seeding of orographic clouds over the Sierra Madre mountain range of Wyoming (Figure 2.1a). Although cloud seeding effects from ASCII continue to be analyzed (e.g., Geerts et al. 2013; Pokharel et al. 2014a; Pokharel et al. 2014b; Jing et al. 2015; Jing and Geerts 2015; Pokharel et al. 2015), the suite of surface and airborne instrumentation deployed during ASCII also provides observations of natural orographic precipitation over this Continental Divide mountain range. The analysis in this paper will largely focus on a 140 minute post-frontal time period when a deep layer of clouds and precipitation associated with a passing baroclinic storm was present.

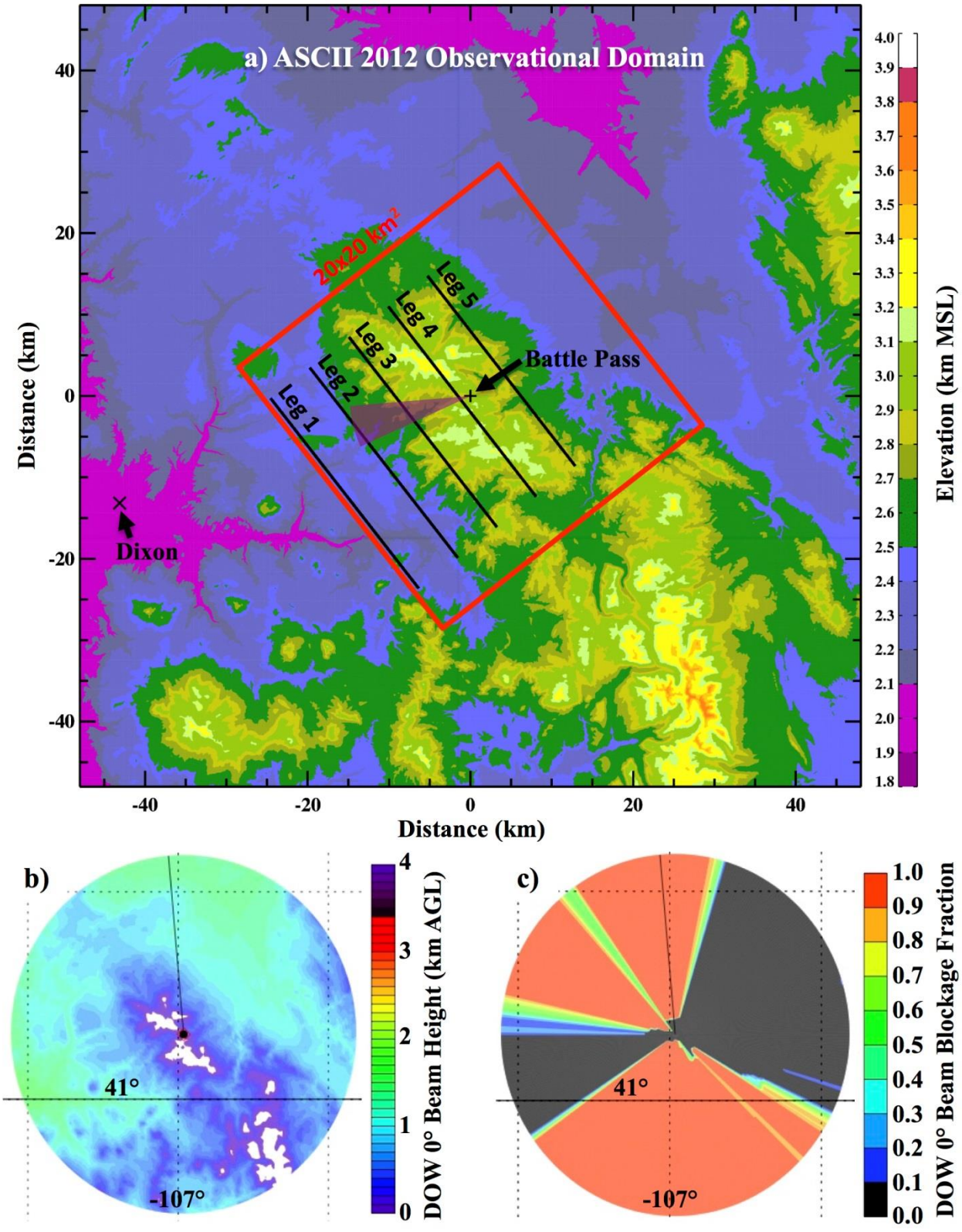

Figure 2.1: a) The observational domain (target area) for the ASCII 2012 field project plotted with 30 m resolution elevation data from the United States Geological Society

(USGS) National Elevation Dataset (NED). Dixon (×) and Battle Pass (+) locations are also labeled along with the UWKA ladder-pattern flight legs 1-5. The 20x20 km^2 region centered at Battle Pass and rotated with the mean axis of the Sierra Madre mountain range is also overlaid with a red box, which is the analysis region used in the Hovmöller diagram in Figure 2.2. The purple wedge starting from the DOW location at Battle Pass indicates the range of targeted DOW RHI azimuths used to calculate median profiles of reflectivity and Z_{DR} (Figure 2.7). The DOW radar beam height (km AGL) calculated for an elevation scan of 0° is plotted in b). The calculated fraction of the DOW radar beam that is blocked for a 0° elevation scan is plotted in c), where a fraction of 0.0 (1.0) indicates no (complete) beam blockage.

Section 2.3 describes the instrumentation used in the analysis as well as any data quality techniques used. Section 2.4 provides a brief overview for the case analyzed in this paper. Section 2.5 provides an overview of the precipitation observed by surface observations and the DOW radar. Section 2.6 identifies and analyzes the impacts of a cross-barrier jet and plunging flow. Section 2.7 identifies regions of turbulence and analyzes its impact on precipitation processes. Section 2.8 provides a discussion on our findings and how they relate to previous research, and section 2.9 summarizes the main findings of this paper.

2.3 Data and Methods

2.3.1 Doppler on Wheels Dual-Polarization X-band Radar

A ground-based scanning Doppler On Wheels (DOW) dual-polarization X-band radar was positioned on the Sierra Madre mountain pass (Battle Pass, 3029 m MSL; Figure 2.1a). The DOW operated at a frequency of 9.5 GHz with a beam width of 0.93° (Wurman 2001). The pulse duration was chosen to be 0.4 μs, relating to a resolution of 60 meters in range. With 800 range gates, the maximum range was 48 km. Data were sampled at 0.5° resolution in azimuth at a rate of 30° s^{-1}. The radar was run with a pulse repetition frequency (PRF) of 2500 Hz, resulting in a Nyquist

velocity of 19.7 m s^{-1}. Besides reflectivity (Z) and Doppler velocity fields, the DOW radar provided differential reflectivity (Z_{DR}), correlation coefficient (ρ_{HV}), spectral width, and total differential phase (Φ_{DP}). The radar scan strategy included full volume scans, or plane position indicator (PPI) scans, with elevation angles every 1° between -1° and 20° elevation, every 2° between 20° and 30°, and every 4° between 30° and 70°. In addition, Z_{DR} calibration scans were performed at 85° and 89°, followed by six range height indicator (RHI) scans. Three RHI scans faced downwind and three faced upwind with the center RHI scan aligned with the mean wind direction during that time. A full 3-dimensional radar volume was collected every 10 minutes. Significant beam blockage prevented reliable radar observations below 6° elevation scans to the north and south of Battle Pass (Figure 2.1b-c).

Ground clutter and multi-path scattering were removed from the PPI data using a fuzzy logic algorithm adapted from Gourley et al. (2007). The algorithm separates measurements contaminated by ground clutter and clear air from measurements of snow using dual-polarimetric variables Z_{DR} and ρ_{HV} and texture fields of Z_{DR}, Φ_{DP}, and ρ_{HV}. Bias corrections for Z_{DR} were first applied using the available calibration scans. The decluttered and quality-controlled polar-coordinate data were then interpolated onto a 3-dimensional Cartesian grid using the National Center for Atmospheric Research (NCAR) Radx2Grid software[1]. A horizontal grid spacing of 200 m was used (approximately three data points per horizontal grid cell). A vertical grid resolution of 250 m was determined by the tangent of the mean

[1] http://www.ral.ucar.edu/projects/titan/docs/radial_formats/radx.html

elevation angle between two consecutive beams at a half-distance of 30 km. The 30 km limit corresponds to the approximate distance between the foothills and Battle Pass. The maximum echo-top never exceeded 10 km MSL, which was used as the upper boundary of the Cartesian grid.

2.3.2 Micro Rain Radar

A vertically-pointing K_a-band (continuous wave mode at 24.23 GHz) METEK Micro Rain Radar (MRR) was deployed at Battle Pass. Vertical profiles of reflectivity (Z), Doppler velocity, and spectral width were averaged over 1-minute intervals with a vertical resolution of 200 m in 31 range gates (up to 9.4 km MSL). Raw Doppler velocities from 0.95-12.195 m s^{-1} are recorded by assuming only downward motion, which is the sum of the vertical air motion and particle fall speeds. A Doppler spectra post-processing technique created by Maahn and Kollias (2012) was implemented on the MRR data to improve sensitivity for snow and de-alias Doppler velocities so that upward (positive Doppler velocity) and downward (negative Doppler velocity) motions can be distinguished between ± 12 m s^{-1}. The first two range gates were considered unreliable and were removed in this post-processing. This makes the closest reliable range gate for the Battle Pass MRR at 3.6 km MSL. MRRs have been used previously in various locations to monitor vertical precipitation structures (e.g., Löffler-Mang et al. 1999; Peters et al. 2002; Peters et al. 2005; Rollenbeck et al. 2007; Tokay et al. 2009; Trivej and Stevens 2010).

2.3.3 W-band Wyoming Cloud Radar

The 94.92 GHz (W-band) Doppler Wyoming Cloud Radar (WCR) was flown aboard the University of Wyoming King Air (UWKA) aircraft along with *in-situ* cloud physics instruments. The WCR consisted of three antennas oriented up, down, and down-fore with respective beam widths of 0.7°, 0.5°, and 0.6°. A PRF of 20 kHz and a pulse width of 250 ns were used, resulting in a range resolution of 37.5 m. More details of the WCR system can be found in Wang et al. (2012) and references within. A schematic of the up, down, and down-fore radar beam configuration can be found in Figure 2 of Geerts et al. (2006). Due to oversampling, a sampling interval of 15 m was achieved. This allowed very high-resolution reflectivity (Z) and Doppler velocity observations above and below the aircraft flight level. Attenuation of the radar beam is assumed to be minimal due to the low Z observed in snowfall and the low amounts of liquid water observed during the case analyzed. A radar blind zone of 100 m above and below the aircraft flight level limited radar observations in the immediate vicinity of the aircraft. Post-processing of WCR data included removing aircraft motion and horizontal wind velocity contamination from the Doppler velocity fields and correcting Z for range from the aircraft.

I*n-situ* cloud physics measurements of LWC from the UWKA flight path were obtained by the Droplet Measurement Technologies, Inc. (DMT) Cloud Droplet Probe (CDP), and ice particle concentrations for diameters between 62.5μm - 2.5 mm were measured using the *fast* OAP-2DC instrument (Wang et al. 2012). Vertical air motion, air temperature, and mixing ratio were measured by additional

standard UWKA instrumentation[2]. A MacCready turbulence meter (MacCready 1964) aboard the UWKA allowed an *in-situ* calculation of Eddy Dissipation Rate (EDR), the cube root of the rate of dissipation of the turbulent kinetic energy and an indication of the strength of turbulence.

As indicated in Figure 2.1a, the UWKA flew ladder patterns at ~ 4 km MSL consisting of five ladder legs parallel to the Sierra Madre mountain range. Ladder legs 1-3 were upwind of the mountain crest, ladder leg 4 was along the mountain crest, and ladder leg 5 was immediately downwind of the mountain crest (Figure 2.1a). Cross-barrier flight legs oriented parallel to the mean wind direction were flown during the ASCII project, however no cross-barrier flight legs were flown during the analysis period presented in this paper.

2.3.4 Atmospheric Profilers

The Mobile GPS Advanced Upper-Air Sounding (MGAUS[3]) balloon rawinsonde system was set up 45 km upwind from Battle Pass at the Dixon Airport (hereafter referred to as Dixon; Figure 2.1a). The MGAUS soundings measured vertical profiles of humidity, temperature, and winds with high vertical resolution (1-5 m) in the upwind atmospheric environment every 1-2 hrs.

A Radiometrics Corporation passive microwave radiometer was deployed at Battle Pass and provided integrated liquid water (ILW) and integrated water vapor (IWV) measurements, and vertical profiles of temperature, humidity, LWC, and

[2] http://www.atmos.uwyo.edu/uwka/index.shtml
[3] http://www.eol.ucar.edu/rtf/facilities/gaus/gaus.html

water vapor density for the mountain crest environment. The radiometer measures microwave emission at 22-30 GHz (water vapor absorption band) and 51-59 GHz (oxygen absorption band) as well as infrared emission at 9.6-11.5 µm. The zenith-pointing antenna has beam widths of 6° (22-30 GHz) and 2.5° (51-59 GHz). Vertical profiles of temperature and relative humidity were derived using a neural network algorithm [Solheim et al. 1998a, 1998b]. The algorithm, based on a radiative transfer model [Rosenkranz 1998], was trained on a 5-year radiosonde climatology. Observations were integrated over 0.2 s, leading to a temperature resolution of 0.25 K. These measurements allow us to monitor atmospheric temperature and moisture changes above the terrain with higher temporal resolution than the MGAUS soundings.

2.3.5 PARSIVEL Disdrometer and Snow Crystal Photography

The laser-optical Particle Size and Velocity (PARSIVEL) disdrometer was installed in a forest opening at Battle Pass to measure *in-situ* snow particle characteristics. The location was chosen to shield the instrument from strong winds that occur at the mountain pass and significantly influence measurement quality (Battaglia et al. 2010; Friedrich et al. 2013). The PARSIVEL disdrometer uses a laser beam to detect individual particle diameters and fall speeds, which allows a particle size and fall velocity distribution to be created. Particle diameters are detectable between 0.25-25 mm and fall velocities between 0.2-20 m s^{-1} across 30x30 useable bins. Particle counts across these diameter and fall velocity bins are measured by the PARSIVEL every 10 seconds. Because of the complicated shapes of

snow particles, reliable snow particle size and velocity observations are a challenge (Battaglia et al. 2010). Due to issues with border effects and multiple particle counts for a single snowflake, observations in size bins < 1 mm were removed in the analysis. More reliable fall velocity measurements are retrieved for snow particles between 1-10 mm in diameter, which are the particles of focus for this paper. Raw particle counts were used to compute normalized particle concentrations per volume (m^{-3} mm^{-1}). These normalized concentrations were then used to compute time-series of total particle concentration and snowfall rate using the bulk snow density relation determined by Brandes et al. (2007).

Snow crystal photographs were taken on a black background every 10-15 minutes during IOPs using a hand-held camera. These photographs allow visual determination of ice crystal habits and the degree of riming or aggregation for individual snow particles, which will be used to infer microphysical processes occurring within the overlying clouds.

2.3.6 Surface Precipitation Gauges and Weather Stations

A Geonor all-weather precipitation gauge was installed at Battle Pass, which allowed *in-situ* liquid-equivalent precipitation accumulation measurements. Although many other precipitation gauges were present at Battle Pass, the Geonor gauge was heated and thus provided the most reliable precipitation accumulations in snowfall. Storm-total precipitation accumulations and rates were calculated from these observations.

Surface weather observations were recorded at Dixon and Battle Pass, including temperature, pressure, relative humidity, wind speed, and wind direction. Measurements at Battle Pass were taken through a mesonet ~ 10 m above the surface on the mast of the DOW truck. Observations at Dixon were taken through NCAR's MGAUS surface weather station at ~ 1-2 m above the surface.

2.4 Case Overview

On 16 January 2012 (ASCII IOP2), widespread snowfall was observed throughout the target area between 1700-2130 UTC during and following the passage of a baroclinic front (Figure 2.2). Many of the ASCII IOPs collected data during shallow storms with abundant LWC, largely because these conditions are prime for ground-based cloud seeding, which was the focus of the field project. Thus, IOP2 allows purely natural snow growth processes to be analyzed within a deep precipitation system associated with a baroclinic frontal passage. This period of IOP2 was chosen for analysis because the DOW observed a consistent deep precipitation layer (echo-tops between 7-8 km MSL) with a moderate 6.5 mm of liquid-equivalent precipitation accumulating at Battle Pass (Figure 2.2). Closer inspection of the precipitation accumulation at Battle Pass (Figure 2.2) indicates two distinct periods of accumulation. A surface cold front, reaching up to 3.5 km MSL above Dixon by 2015 UTC (Figure 2.3), moved over Dixon (Battle Pass) around 1720 UTC (1810 UTC) and exited the target region by 1910 UTC (Figure 2.2). The front is evident by a band of high reflectivity (Z > 35 dBZ) observed by the DOW radar (Figure 2.2), rapid snowfall accumulation at Battle Pass between 1800-1900

UTC (2.7 mm hr^{-1}; Figure 2.2), a sharp drop in surface temperatures at Battle Pass and Dixon (6-7°C by 2130 UTC; Figure 2.4a), a 15 m s^{-1} spike in wind speed at Dixon and a sharp drop (~10 m s^{-1}) in wind speeds at Battle Pass (Figure 2.4b), a sharp shift in wind direction at Dixon from SSW to NW (Figure 2.4c), a rapid increase in relative humidity from 60% to 85% at Dixon (Figure 2.4f), and spikes in ILW (0.54 mm; Figure 2.4e) and IWV (0.53 cm; Figure 2.4g). We designate the period 1700-1910 UTC as "Frontal" because the baroclinic front was responsible for generating precipitation over the ASCII target region during this time. The atmosphere was moist-neutral to moist-unstable up to 5.5 km MSL prior to the front (Figures 2.3, 2.4d) with strong cross-barrier low-level winds (10-25 m s^{-1}; Figures 2.3, 2.4b). The passage of the cold front stabilized the atmosphere (Figure 2.4d) and decoupled the boundary layer from the upper air with an inversion that developed near 3.5 km MSL by 2015 UTC (Figure 2.3). This inversion separated post-frontal northwesterly (along-barrier) slightly moist unstable flow from strong (10-30 m s^{-1}) southwesterly (cross-barrier) stable flow above. Note that the northwesterly flow is part of the low-level post-frontal airmass and not a result of deflected airflow. The surface-based calculation of moist Froude number (Fr_m) following the frontal passage stayed relatively steady near 1, indicating wave motions over the mountain were likely. The period from 1910-2130 UTC is designated as "Post-Frontal" and is the main focus of the following analysis due to the shear instability that set up during this time.

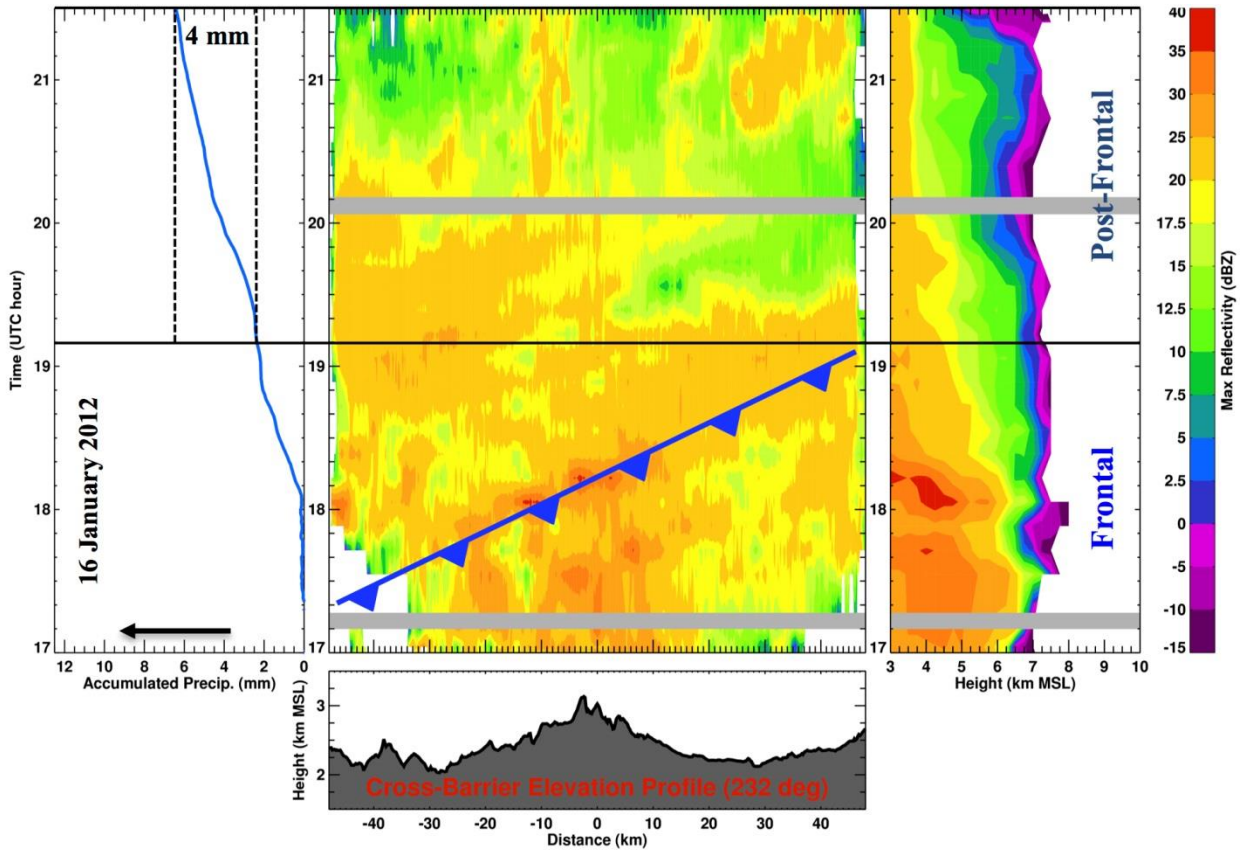

Figure 2.2: A Hovmöller diagram of maximum reflectivity observed by the DOW radar above 3 km MSL is plotted in the center panel, accumulated surface precipitation from the Geonor precipitation gauge at Battle Pass is plotted in the left panel, and maximum reflectivity observed by the DOW radar with height and time is plotted in the right panel for the time period 1700-2130 UTC 16 January 2012 (IOP2). This period encompasses the baroclinic frontal passage and post-frontal stratiform precipitation that occurred during IOP2. The maximum reflectivity for each x grid point in the center Hovmöller panel is computed within y = +/- 20 km, and the maximum reflectivity with height in the right panel is computed within the 20x20 km^2 region shown in Figure 2.1a for each Cartesian-gridded DOW radar volume. The Cartesian-gridded DOW radar volumes used in this figure were rotated with the mean Sierra Madre mountain range axis so that the positive (negative) x-axis is oriented at 52° (232°) from North, which is roughly perpendicular to the Sierra Madre mountain barrier. The elevation profile along this azimuth is shown in the bottom panel, with the DOW location at Battle Pass at x = 0 km. The grey blocks in the center and right panels are time periods when no DOW radar data was available.

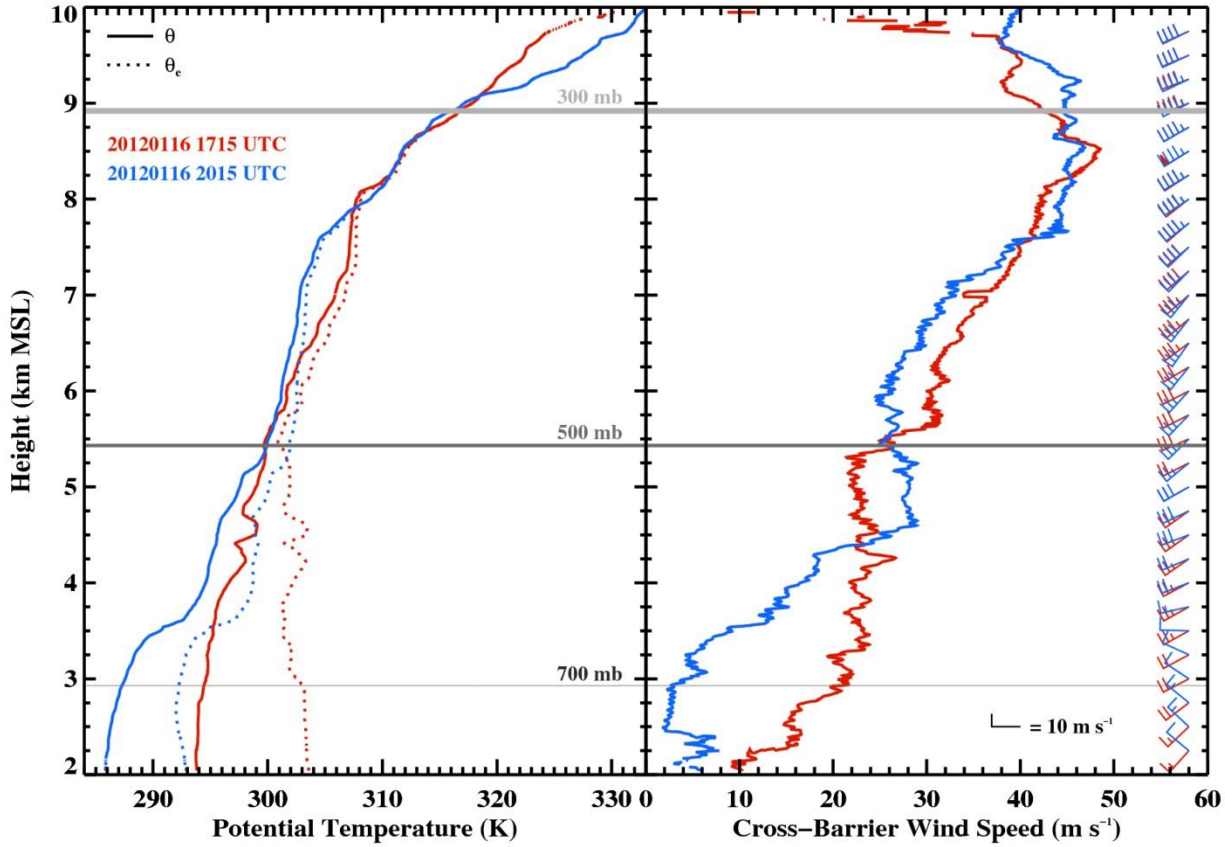

Figure 2.3: MGAUS atmospheric soundings launched from Dixon are plotted for 1715 UTC (red) and 2015 UTC (blue) on 16 January 2012. These times show the pre-frontal and post-frontal environment during IOP2, respectively. Potential temperature (θ, solid line) and equivalent potential temperature (θ_e, dotted line) are plotted in the left panel and computed cross-barrier wind speed is plotted in the right panel. Median wind speed and direction is also plotted as a wind barb every 0.25 km MSL in the right panel (flag = 50 m s^{-1}; full barb = 10 m s^{-1}; half barb = 5 m s^{-1}). The cross-barrier wind speed was computed as the component of the observed wind in a 232° wind direction. Grey bars across both panels denote the range of heights at which the 300 mb (light grey), 500 mb (medium grey), and 700 mb (dark grey) pressure levels were located in the soundings shown.

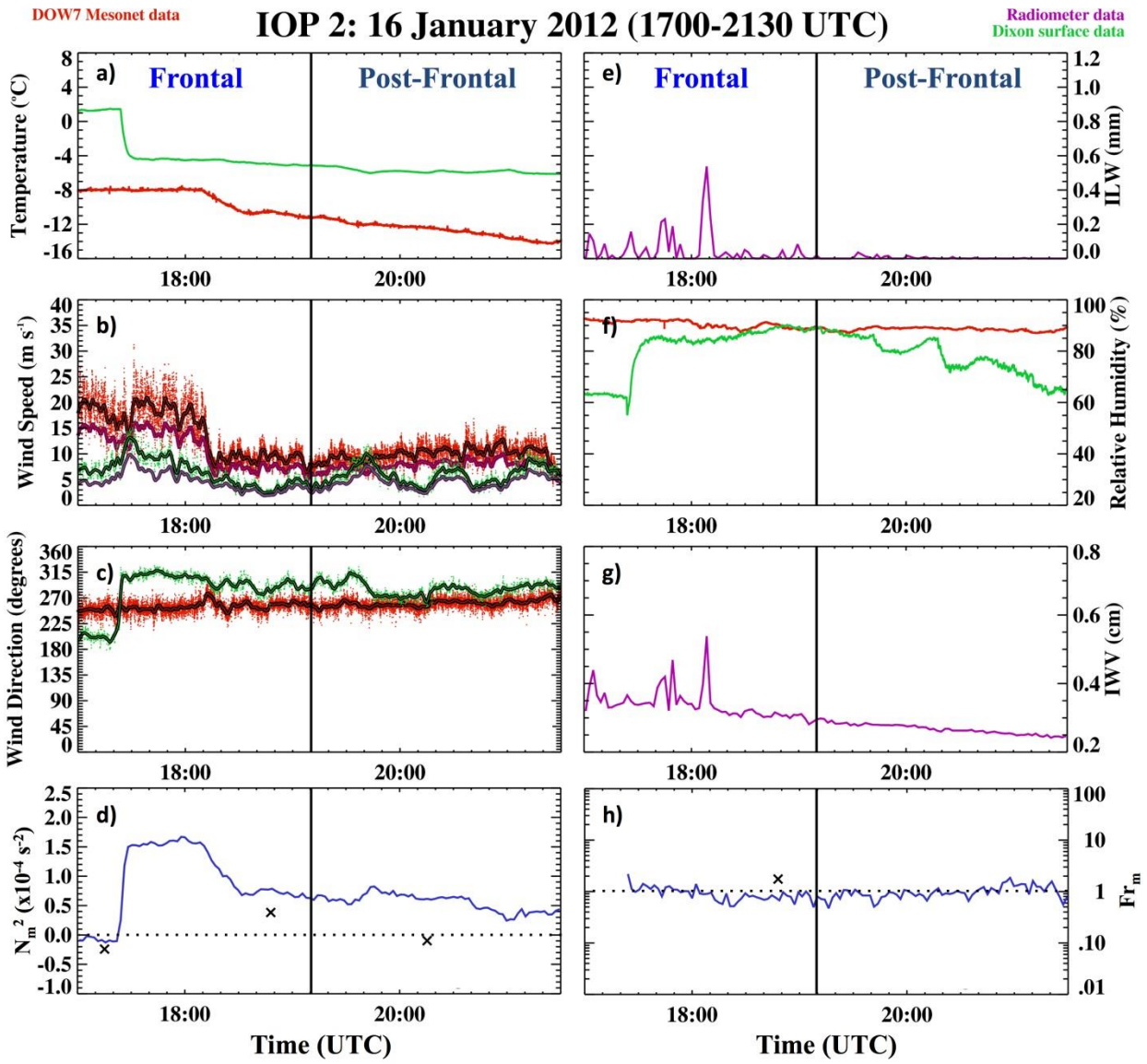

Figure 2.4: Surface weather observations, vertically-integrated liquid water (ILW) and water vapor (IWV), and surface-based and sounding-based stability parameters are plotted between 1700-2130 UTC on 16 January 2012 during IOP2. a) Air temperature, b) wind speed, c) wind direction, and f) relative humidity observations are plotted for Dixon (green) and Battle Pass (red) locations. Raw (dots) and 60 s averaged (solid line) surface wind speed observations (black line border) at Dixon (green) and Battle Pass (red) as well as computed cross-barrier wind components (purple line border) are plotted in b). ILW and IWV observations from the microwave radiometer at Battle Pass are plotted in e) and g), respectively. Calculated moist squared Brunt-Väisälä Frequency (N_m^2) is plotted in d), and calculated moist Froude # (Fr_m) is plot in h). The blue lines in d) and h) are calculated using surface observations from Dixon and Battle Pass, and the black X symbols are calculated using MGAUS soundings from Dixon. N_m^2 and Fr_m values were computed using observations at the two elevations corresponding to Dixon (1980 m MSL) and Battle Pass (3030 m MSL) locations. The separation between moist stable ($N_m^2 > 0$) and moist unstable conditions ($N_m^2 < 0$) is separated by a dotted black line at $N_m^2 = 0$ in d). The transition

between blocked flow ($Fr_m < 1$) and un-blocked flow ($Fr_m > 1$) is separated by a dotted black line at $Fr_m = 1$ in h). A vertical black line separates the frontal and post-frontal periods mentioned in the paper, similar to Figure 2.2.

2.5 Precipitation Processes Indicated by Surface Observations and Radar

During the post-frontal period between 1910-2130 UTC on 16 January 2012, deep, widespread stratiform clouds and precipitation dominated the ASCII target region with maximum Z of 5-25 dBZ observed by the DOW radar (Figures 2.2, 2.5). A total of 4 mm of precipitation accumulated at Battle Pass during this time with decreasing intensity (1.3-2.9 mm hr^{-1}; Figure 2.2). At the beginning of this period (1910-2000 UTC), higher reflectivity (maximum Z > 20 dBZ) was observed from ~50 km upwind to Battle Pass. This enhanced precipitation was advected from the southwest by an approaching mid-level cross-barrier jet (see section 5). Later (2000-2130 UTC), higher Z only occurred 5-15 km upwind of Battle Pass. These isolated areas of higher Z (18-25 dBZ) after 2000 UTC were generated mainly below 4 km, as shown in Figure 2.2 and the individual DOW radar volume at 2023 UTC (Figure 2.6).

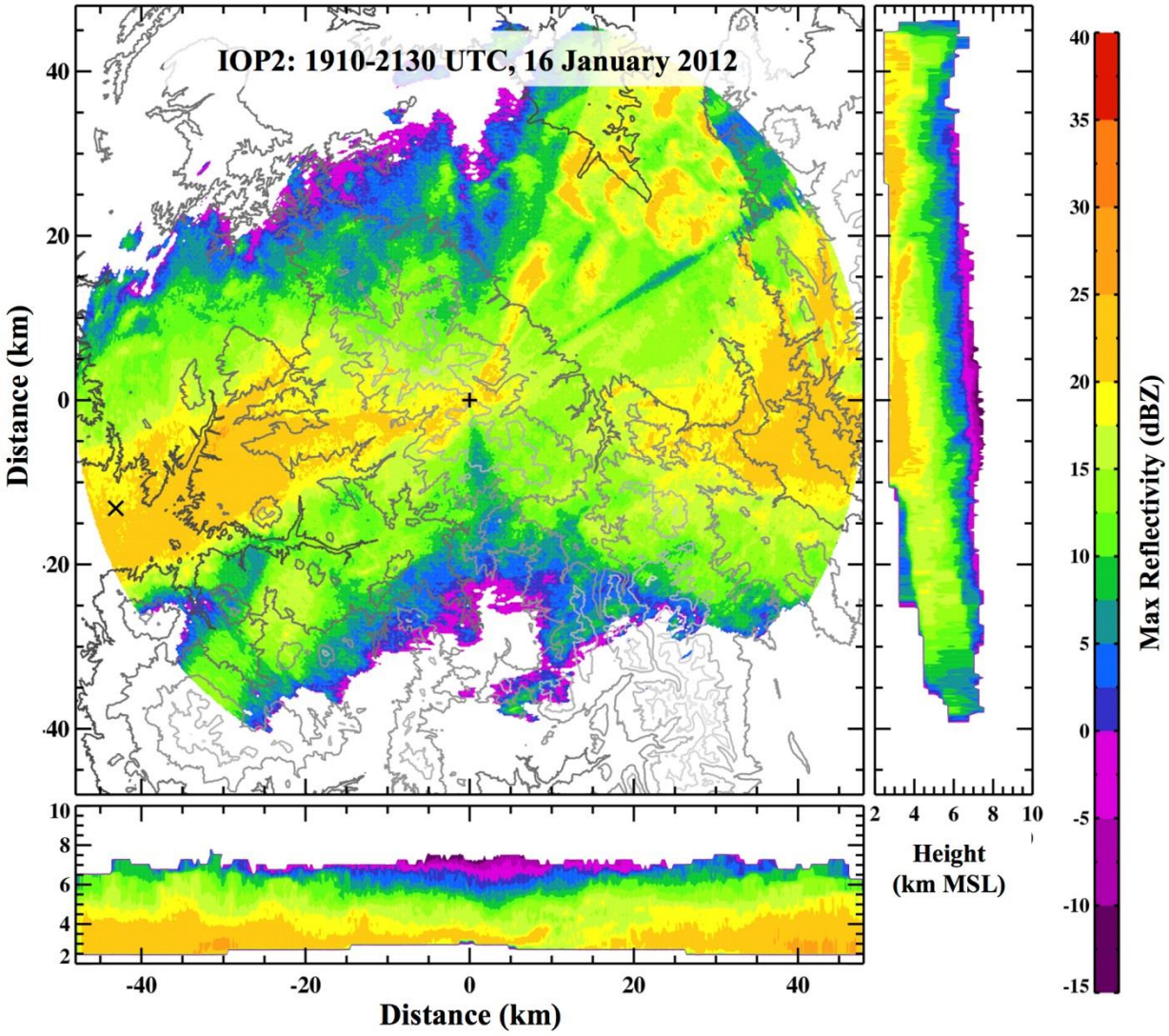

Figure 2.5: Maximum reflectivity observed by the DOW radar above 2 km MSL is plotted for the post-frontal period between 1910-2130 UTC on 16 January 2012 (IOP2). USGS NED terrain elevation is overlaid in the center panels. Maximum reflectivity at each (x,z) grid point within y = +/- 20 km is plotted in the bottom panel, and maximum reflectivity at each (y,z) grid point within x = +/- 20 km is plotted in the right panel. The DOW location at Battle Pass is labeled as a black +, and the Dixon airport location is marked with a black X. Elevation contours are at 2.1, 2.4, 2.7, 3.0, 3.3, and 3.6 km MSL and are colored dark grey at low elevations (2.1 km MSL) to light grey at high elevations (3.6 km MSL). See text for further details.

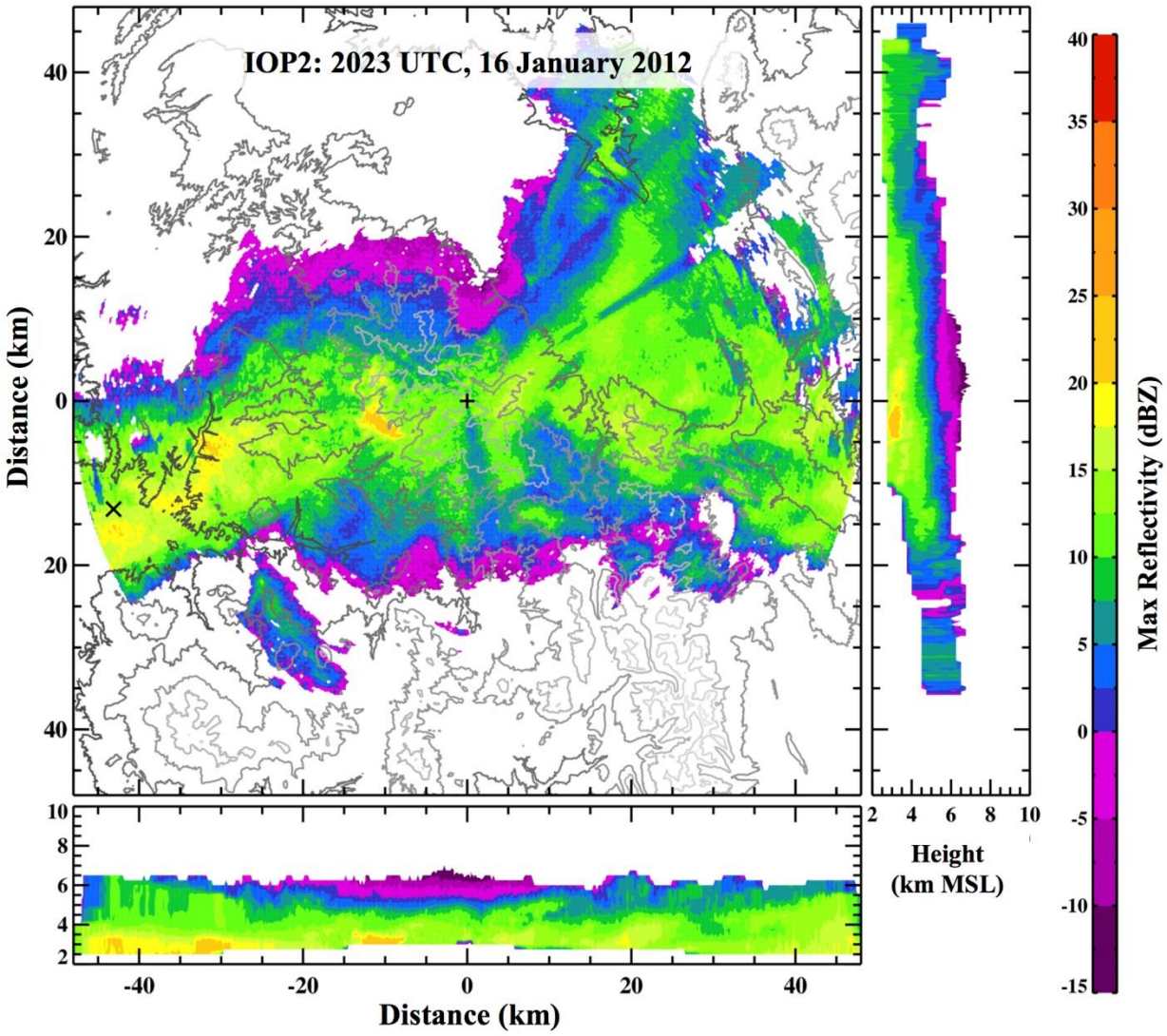

Figure 2.6: As in Figure 2.5, except for a single Cartesian-gridded DOW radar volume at 2023 UTC on 16 January 2012 (IOP2).

To further investigate precipitation processes during this post-frontal period, we analyze vertical profiles of median Z and Z_{DR} from DOW RHI scans (best available RHI scan every 10 minutes; Figure 2.7). Median profiles were derived from data collected over a 15 km region immediately upwind from Battle Pass (245°-265° azimuths; Figure 2.1a). At upper-levels between 5.5-7 km MSL, median profiles of Z and Z_{DR} rapidly increased with decreasing height by 10-15 dBZ km^{-1}

(Figure 2.7a) and 0.5-1.5 dB km^{-1} (Figure 2.7b), respectively. Higher median Z was observed in this layer around 1930 UTC (up to 4 dBZ), suggesting upper-level snow growth was enhanced during this time. Temperatures in this layer ranged between -28°C and -40°C (Figure 2.7). Studies have shown that pristine plate-like snow crystals (Bailey and Hallett 2009) grow through water vapor deposition in this temperature region near cloud-tops of stratiform precipitation with low reflectivity ($-10 < Z < 10$ dBZ) and positive Z_{DR} between 0-2 dB (Ryzhkov and Zrnić 1998; Moisseev et al. 2009; Kennedy and Rutledge 2011; Bechini et al. 2013; Schneebeli et al. 2013).

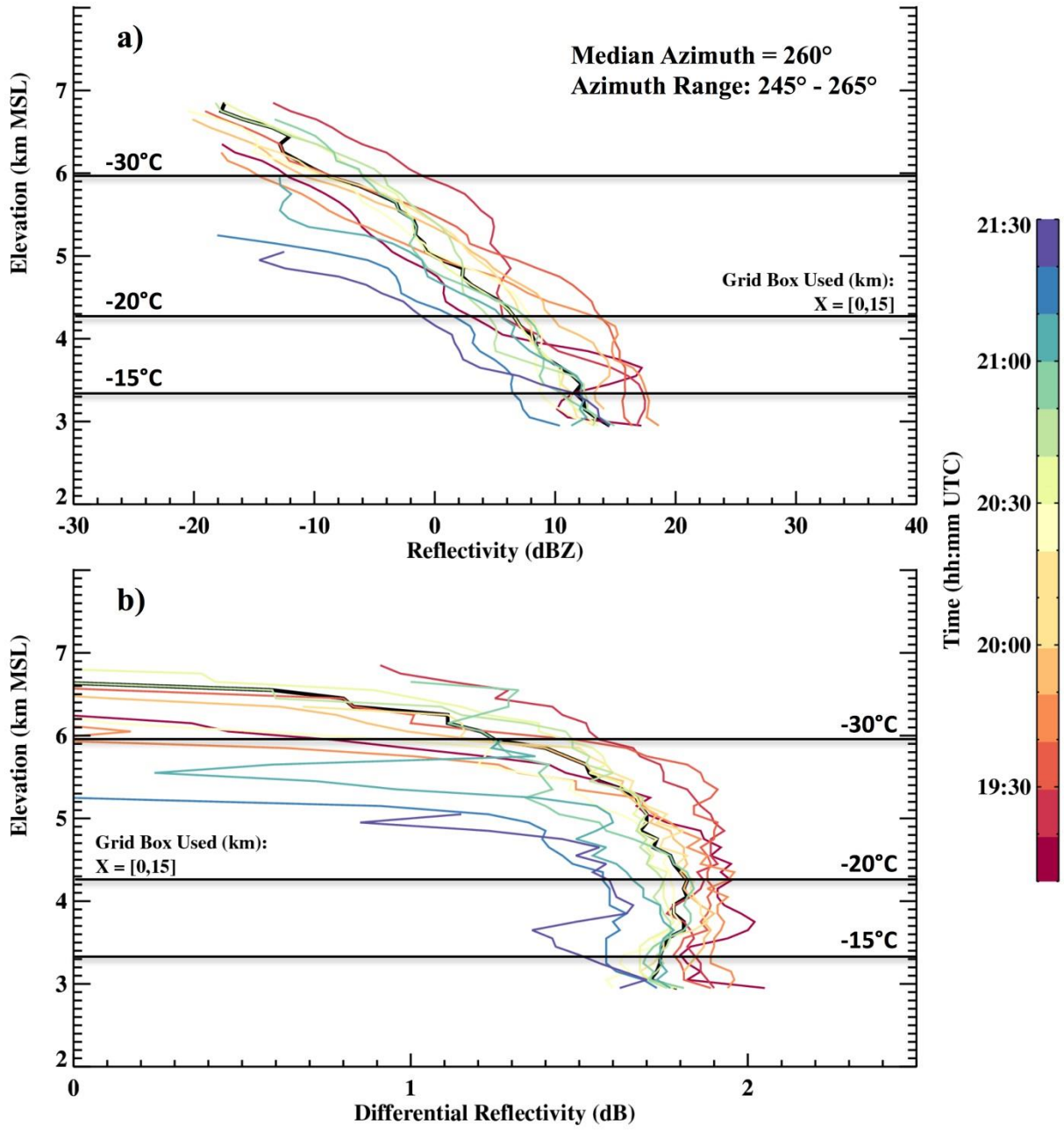

Figure 2.7: Median profiles of a) reflectivity and b) differential reflectivity calculated from upwind DOW radar RHI scans every ~10 minutes between 1910-2130 UTC on 16 January 2012 (IOP2). Each median profile is calculated within a horizontal distance of 0-15 km from the DOW radar. The color-coded times of each median profile can be identified by the color bar on the right side of the figure. The overall median profile over this time period is plotted as the thick black line. The median targeted RHI azimuth and azimuth range between 1910-2130 UTC is displayed in a) and Figure 2.1a for reference. The mean height of the -15°C, -20°C, and -30°C temperature levels observed by the radiometer at Battle Pass are overlaid and labeled. Note that no RHI scans were available between 2000-2010 UTC.

At mid-levels between 4-5.5 km MSL, Z_{DR} increased less rapidly (< 0.5 dB km^{-1}) and became fairly constant with height between 1.5-2 dB (Figure 2.7b). The Z_{DR} CFAD (not shown) shows 30-50% of the observed Z_{DR} was between 1.5-2 dB in this layer. Median Z generally continued to increase (up to 15 dBZ) with decreasing height at varying rates with time in this mid-level layer (1-20 dBZ km^{-1}; Figure 2.7a). Temperatures in this layer ranged between -18°C and -28°C (Figure 2.7). These observations indicate pristine horizontally-oriented snow crystals likely grew in size without changing their shape in this layer. Also note that the overall Z and Z_{DR} in this layer decreases over time after 1930 UTC (Figure 2.7), indicating snow particles likely became smaller with less oblate shapes between 1930-2130 UTC.

At low-levels between 3-4 km MSL, reflectivity generally increased slightly with decreasing height (0-10 dBZ km^{-1}), but rapid increases in Z (> 20 dBZ km^{-1}) were observed at the beginning (before 1930 UTC) and end (around 2130 UTC) of this analysis period (Figure 2.7a). Z_{DR} generally remained constant or decreased with decreasing height in this layer (-0.1 dB km^{-1}; Figure 2.7b), but Z_{DR} increased where rapid reflectivity increases occurred before 1930 UTC and around 2130 UTC. Temperatures in this layer ranged from -14°C to -18°C (Figure 2.7). Localized positive Z_{DR} and specific differential phase (K_{DP}) enhancements in areas with temperatures near -15°C are often associated with rapid dendritic growth (Hogan et al. 2002; Andrić et al. 2010; Kennedy and Rutledge 2011; Andrić et al. 2013; Bechini et al. 2013). The positive K_{DP} signature usually associated with rapid dendritic

growth cannot be verified in this case because Φ_{DP} measurements became unreliable during this period.

In-situ snow particle observations at the Battle Pass surface (~ 3 km MSL) can be used to verify microphysical growth mechanisms indicated by the DOW radar. Dendritic growth before 1930 UTC is supported by surface snow crystal photographs taken at 1920 UTC at Battle Pass, which show the presence of dendrites, stellar crystals, and large dendritic aggregates (panel I; Figure 2.8a). PARSIVEL observations at Battle Pass before 1930 UTC show an increase in total particle concentration (300 to 2000 m^{-3}; Figure 2.8b), increased snowfall rate (0.3 to 2 mm h^{-1}; Figure 2.8d), and the presence of large particles ($d > 5$ mm; Figure 2.8c), indicative of the observed large dendritic aggregates. After 2000 UTC, smaller un-rimed plates, sectored plates, capped columns, and irregular polycrystalline plate-like crystals were observed during the remainder of the analysis period (panels II and III; Figure 2.8a). PARSIVEL observations support snow crystal photographs indicating smaller particle diameters ($d < 5$ mm) were observed after 1930 UTC (Figure 2.8c). However, total particle concentrations and snowfall rates remained elevated at ~1000 m^{-3} and ~1 mm h^{-1} until 2107 UTC (Figure 2.8b,d). No clear photographs of fern-like dendritic crystals were observed at the surface around 2130 UTC, but stellar dendrites were captured (panel III; Figure 2.8a). PARSIVEL observations show the return of larger aggregates ($d > 5$ mm; Figure 2.8c) and increased total particle concentrations (2500 m^{-3}; Figure 2.8b) and snowfall rates (2 mm h^{-1}; Figure 2.8d) around 2130 UTC. Note that the presence of larger aggregates

at the Battle Pass surface after 2130 UTC seem to be collocated with the dendritic growth signatures indicated by the DOW radar within 1 km above the Battle Pass surface. This is expected because dendrites are more susceptible to aggregation due to mechanical interlocking (e.g., Rauber 1987). Dendritic aggregates have been observed and modeled to have low Z_{DR} (~ 0 dB) due to their quasi-spherical shapes and tendency to tumble (Ryzhkov and Zrnić 1998; Andrić et al. 2010; Kennedy and Rutledge 2011; Andrić et al. 2013). The presence of aggregates may explain the relative minima in Z_{DR} below 4 km MSL before 1930 UTC and around 2130 UTC (Figure 2.7b). However, the still relatively high median Z_{DR} within these minima (1.35-1.8 dB; Figure 2.7b), as well as the small concentration of particles having $d >$ 5 mm (up to 200 m^{-3} mm^{-1}; Figure 2.8c), indicates large aggregates did not dominate the DOW radar signal. Rather, the horizontally-oriented pristine dendrites and stellar crystals present during these times dominated. The relatively low height of the dendritic growth layer near -15°C (within 1 km above the Battle Pass surface) likely prevented substantial aggregation before reaching the Battle Pass surface.

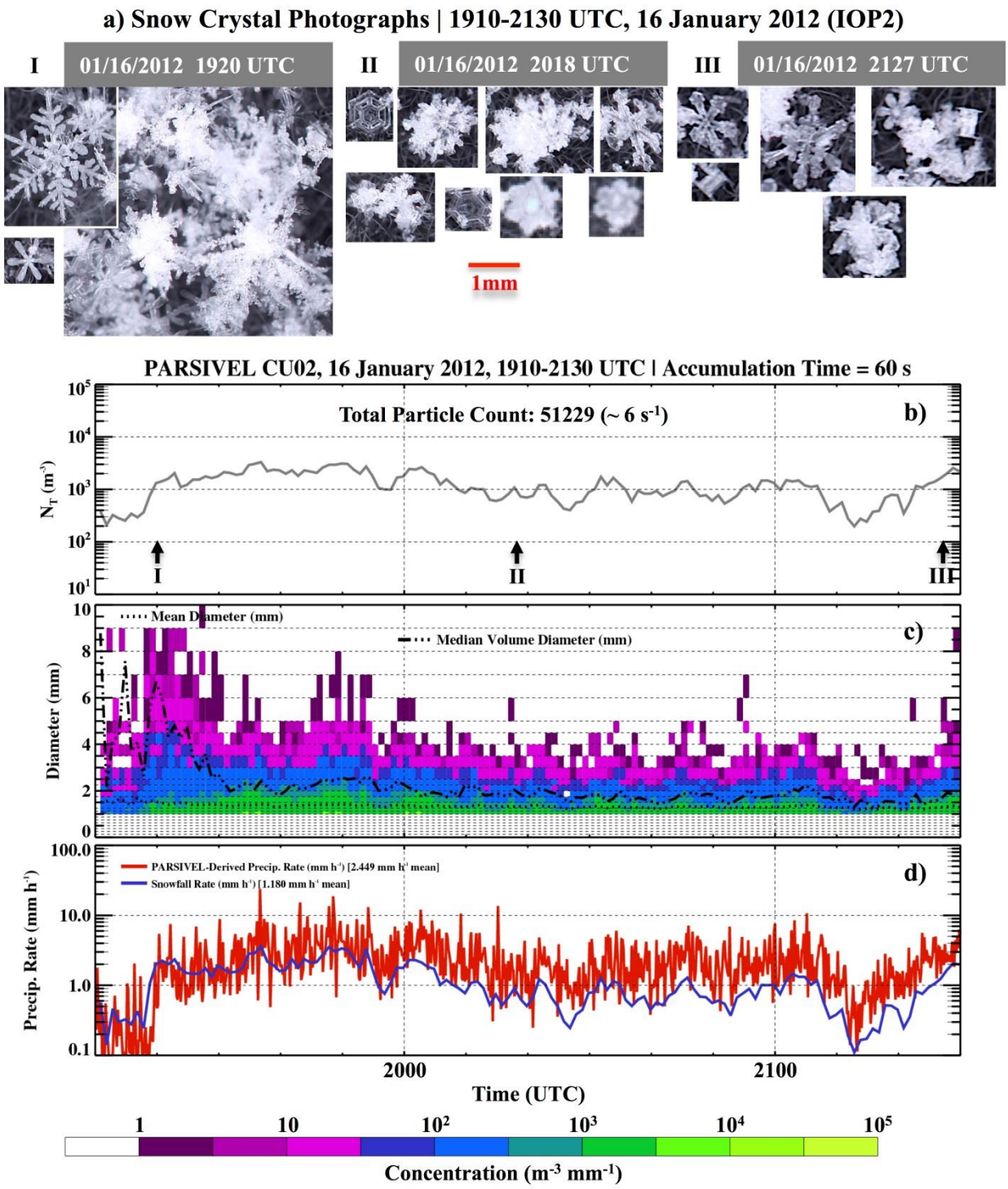

Figure 2.8: a) Snow crystal photographs taken at the surface of Battle Pass at 1920 UTC (panel I), 2018 UTC (panel II), and 2127 UTC (panel III) on 16 January 2012 during IOP2. PARSIVEL disdrometer observations from Battle Pass between 1910-2130 UTC on 16 January 2012 during IOP2 are plotted in b) - d), including b) total particle concentration, c) normalized particle concentrations per diameter bin (see concentration color bar at bottom), and d) raw PARSIVEL-derived precipitation rates and calculated snowfall rates. The mean

(median volume) particle diameter over time is plotted as a dotted (dash dot dot dot) line in c) as well. The total particle count observed by the PARSIVEL disdrometer during this time is labeled along with the mean number of observed particles per second in b). The times when the snow crystal photographs were taken are indicated in b). Note that all PARSIVEL observations with particle diameters less than 1 mm were removed from the dataset before calculating PSD-derived parameters, but the raw PARSIVEL-derived precipitation rate takes into account all measured particles.

The MRR at Battle Pass observed echo-tops (Z ~ -5 dBZ) up to 6 km MSL over the mountain crest with an overall steady increase in median Z with decreasing height at a rate of 7 dBZ km^{-1} between 3.6-6 km MSL (Figure 2.9a). This stratiform reflectivity profile is similar to the overall median Z observed by the DOW radar immediately upwind of Battle Pass (~ 8 dBZ km^{-1}) between 3-6.8 km MSL (Figure 2.7a). The MRR-observed reflectivity profile over time (Figure 2.10a) shows changes in precipitation with increased temporal resolution (1 minute) compared to the DOW observations (10 minutes). MRR-observed echo-top increased significantly between 1910-1930 UTC from 4.2 to 6 km MSL (Figure 2.10a), indicating upper-level precipitation growth was enhanced and advected over Battle Pass (Figure 2.2), during this time. This agrees with the DOW-observed reflectivity profiles as median Z increased by 3-11 dBZ between 1915 and 1925 UTC above 4 km MSL (Figure 2.7a). At low-levels between 3.6-4 km MSL, MRR-observed reflectivity consistently increased rapidly with decreasing height (12-25 dBZ km^{-1}) during this time (Figure 2.10a). The DOW radar observed similar reflectivity increases in this layer before 1930 UTC (Figure 2.7a). The highest reflectivities observed by the MRR (20-25 dBZ) occurred in pockets below 4.5 km MSL between 1930-2015 UTC (Figure 2.10a). This agrees with the DOW observations as median Z is highest and consistently above the overall median between 3.6-4.5 km MSL from 1930-2000 UTC (Figure 2.7a).

PARSIVEL observations at the Battle Pass surface also indicate the heaviest snowfall rates occurred during this time (1-4 mm h^{-1}; Figure 2.8d). After 2015 UTC, MRR-observed Z generally decreased at all heights, but individual towering reflectivity enhancements were observed up to 6 km MSL between 2030-2100 UTC (Figure 2.10a). After 2100 UTC, MRR echo-top decreased steadily down to 4.6 km MSL.

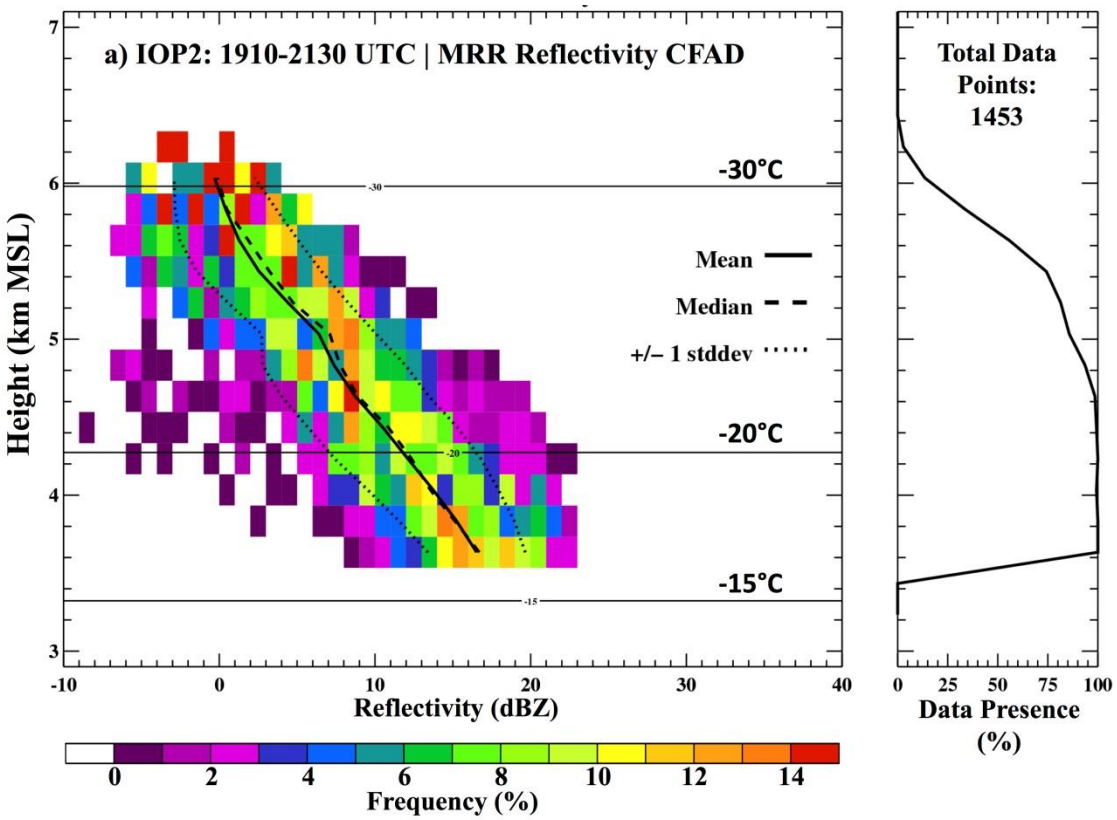
a) IOP2: 1910-2130 UTC | MRR Reflectivity CFAD
Height (km MSL)
-30°C
-20°C
-15°C
Mean
Median
+/– 1 stddev
Reflectivity (dBZ)
Frequency (%)
Total Data Points: 1453
Data Presence (%)

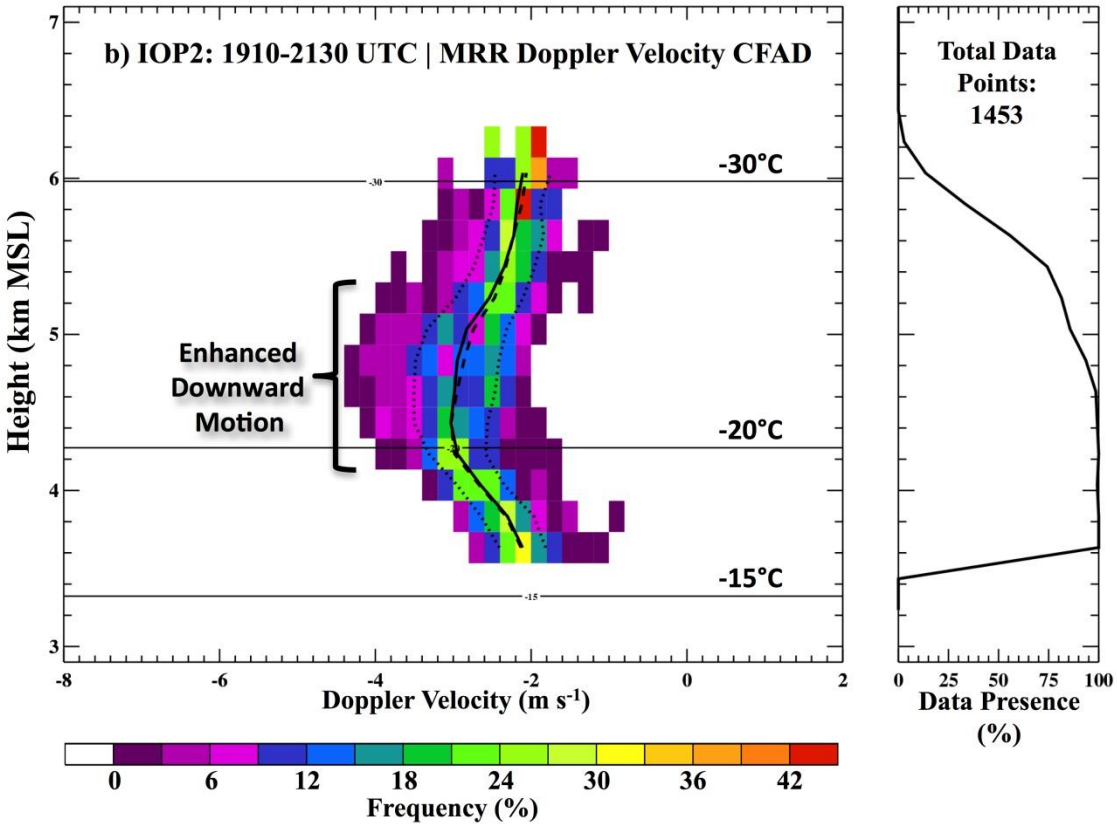
b) IOP2: 1910-2130 UTC | MRR Doppler Velocity CFAD
Height (km MSL)
-30°C
-20°C
-15°C
Enhanced Downward Motion
Doppler Velocity (m s-1)
Frequency (%)
Total Data Points: 1453
Data Presence (%)

Figure 2.9: Contoured Frequency by Altitude Diagrams (CFADs) are plotted for a) reflectivity and b) Doppler velocity observed by the vertically-pointing MRR at Battle Pass between 1910-2130 UTC on 16 January 2012 (IOP2). Frequency is a function of height, so summing the frequencies along a specific height level will result in 100%. Note that the frequency scale changes between the reflectivity and Doppler velocity CFADs. The mean temperature heights between 1910-2130 UTC on 16 January 2012 (IOP2) are labeled in each panel based on temperature profiles observed by the radiometer at Battle Pass. The far right panels show the total number of MRR-observed reflectivity and Doppler velocity observations and the data presence, the percentage of measurement times with data present in each height level during this time period. The mean, median, and ±1 standard deviation of reflectivity and Doppler velocity for each height are plotted in the respective CFADs. See text for further details.

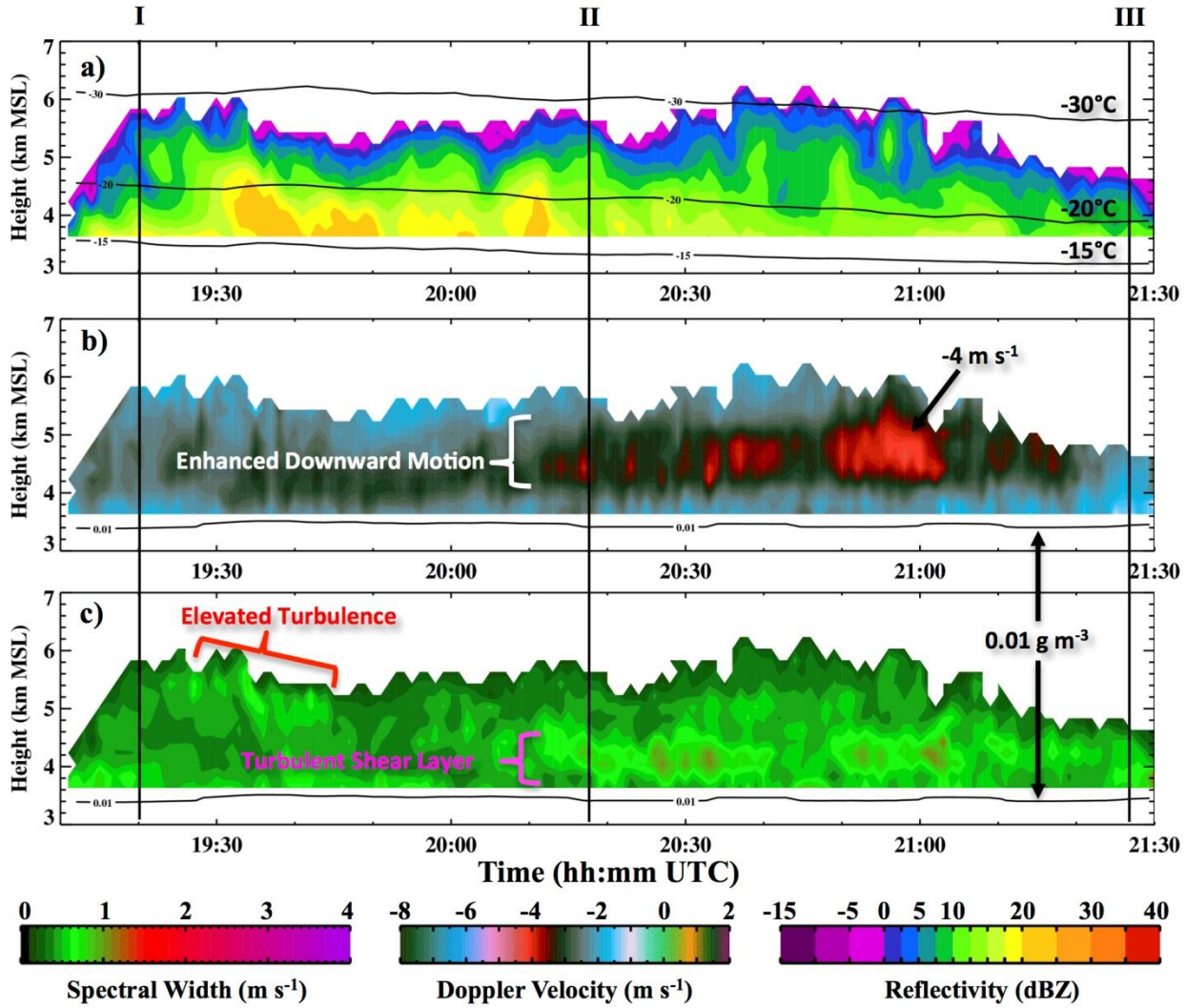

Figure 2.10: Time-height profiles of a) reflectivity, b) Doppler velocity, and c) spectrum width observed by the MRR at Battle Pass between 1910-2130 UTC on 16 January 2012

(IOP2). Radiometer-observed temperature levels (-30°C, -20°C, and -15°C) are overlaid in a) and radiometer-observed LWC levels are overlaid in b) and c) as solid black lines. The times the snow crystal photographs (Figure 2.8a) were taken are labeled as I, II, and III in the time-height plots of MRR data. Note that the MRR is vertically-pointing, so Doppler velocities are positive for upward motion and negative for downward motion. See text for further details.

2.6 Cross-Barrier Jet and Plunging Flow: Implications for Microphysical Processes

Vertical profiles of MRR-observed Doppler velocity show a distinct layer of enhanced downward motion (Doppler velocities < -3 m s^{-1}) between 4.1-5.3 km MSL, with the strongest downward motion occurring between 2010-2120 UTC (Figures 2.9b, 2.10b). This area of enhanced downward motion is collocated with a distinct cross-barrier jet that was observed by the DOW radar between 1920-2115 UTC (coinciding with the arrival of the advected upper-level reflectivity enhancement) and by the 2015 UTC upwind sounding (Figure 2.3). Doppler radial velocity fields observed by the upwind (260° azimuth) and downwind (79° azimuth) DOW RHI scans at 2055 UTC (Figure 2.11a) indicate this cross-barrier jet between 4-6 km MSL with maximum Doppler velocities between 25-30 m s^{-1}. The calculated cross-barrier wind speed from the 2015 UTC sounding (Figure 2.3) shows a relative enhancement indicative of a cross-barrier jet between 4.3-5.5 km MSL with maximum cross-barrier winds approaching 30 m s^{-1} near 4.6 km MSL.

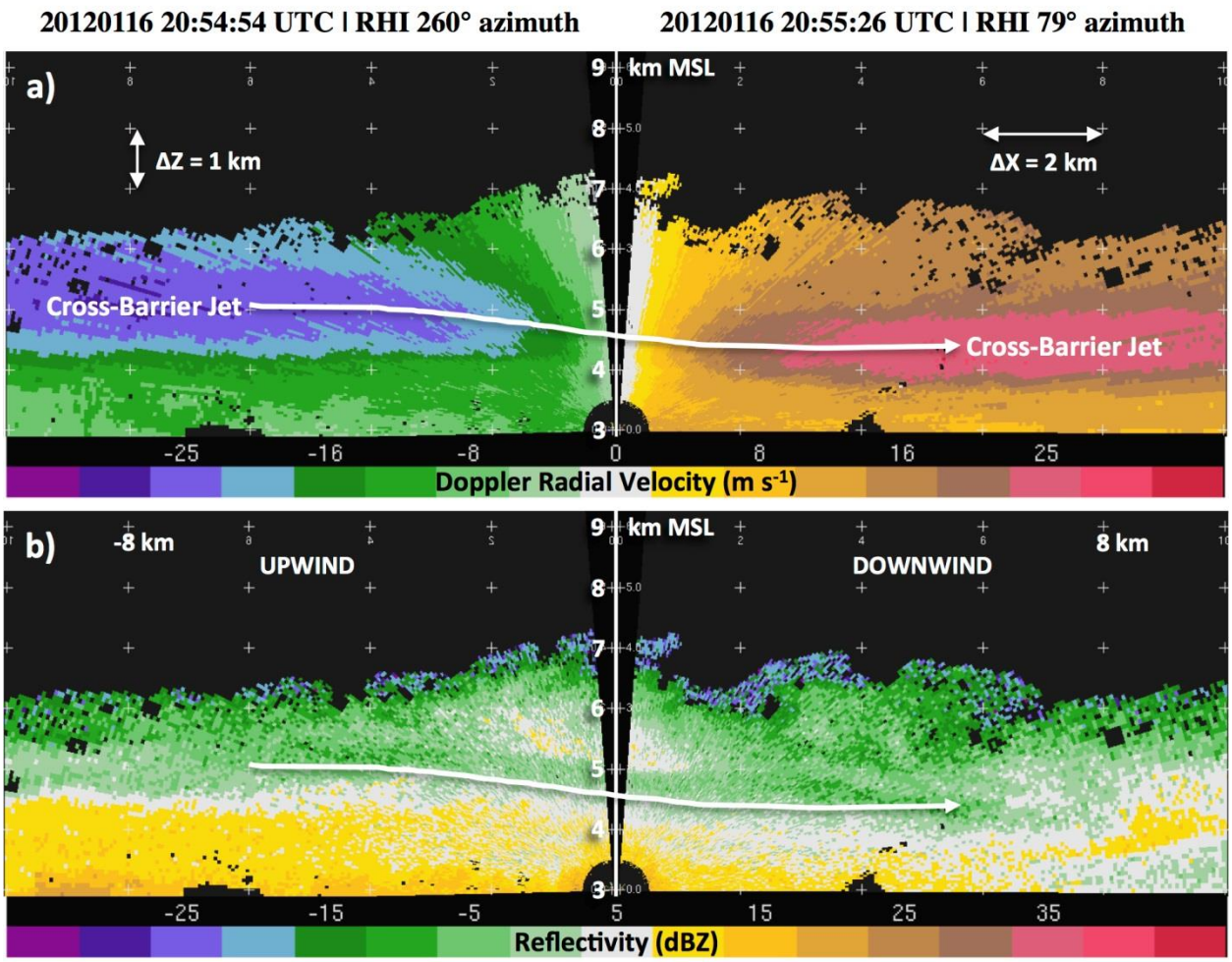

Figure 2.11: a) Doppler radial velocity and b) reflectivity observed by the DOW radar RHI scans at 2055 UTC 16 January 2012. Tick marks (+) in a) and b) denote Cartesian heights and distances from the DOW radar, which are spaced every 1 km in height (ΔZ) and every 2 km in horizontal distance (ΔX). The ±8 km horizontal distance tick marks are labeled in b). The center of the cross-barrier jet is denoted with a white arrow in a) and b). Doppler de-aliasing was performed on the Doppler velocity field using the Soloii radar software.

Decreasing MRR-observed Doppler velocities can be related to an increase in downward air motion, an increase in particle fall velocity, or both. Negative Doppler velocities exceeding 3 m s^{-1} in magnitude are much higher than typical observed fall velocities of snow crystals (< 1.5 m s^{-1}; Lamb and Verlinde 2011, their Figures 9.7, 9.10) and aggregates (< 2 m s^{-1}; Brandes et al. 2008). Since the precipitation analysis (section 4) indicates pristine snow crystals dominated the reflectivity

signal during this period, the enhanced downward motion observed by the MRR (Figures 2.9b, 2.10b) can be related to an increase in downward air motion rather than an increase in particle fall speed. Strong downward motion within orographic flow, also referred to as plunging flow, has been observed and modeled in various orographic settings on the lee side of mountain barriers (e.g., Garvert et al. 2007; Smith et al. 2012; Saleeby et al. 2013; Geerts et al. 2015). Geerts et al. (2015) observed plunging flow in winter snowstorms over an adjacent mountain range in Wyoming, the Medicine Bow Range, using the WCR flown aboard the UWKA. They show that this plunging flow is characterized by strong downward air motion immediately downwind of the mountain crest, which causes snow to fallout rapidly and sublimate in the lee (typically within ~ 20 km from the crest for stratiform precipitation). They also observed low-level cross-barrier jets riding up and over the mountain, with the jet decreasing in height in the lee and sometimes accelerating. Lee-side plunging flow is typically associated with a vertically propagating mountain wave centered at the mountain crest (Garvert et al. 2007; Geerts et al. 2015). Unfortunately no along-wind UWKA flights were flown during this period, so cross-barrier WCR-observed Z and Doppler vertical velocity transects similar to analysis in Geerts et al. (2015) are not available. However, plunging flow is indicated by the decrease in height of the maximum Doppler radial velocities as well as the decreasing height of the 5 dBZ reflectivity contour observed by the DOW radar from upwind to downwind at 2055 UTC (denoted by the white line/arrow in Figure 2.11a,b). At Battle Pass, the downward motion observed by the MRR did not

reach the surface. It is not clear whether the decoupled boundary layer prevented the flow from reaching the surface or if plunging flow reached the surface farther downstream.

Plunging flow is important because it impacts the distribution and intensity of snowfall over the lee-side mountain slope. Downward air motion is detrimental to precipitation growth because adiabatic motion favors warming and drying, thus evaporation and sublimation (e.g., Saleeby et al. 2013). That means snow particles that grow upwind of the mountain and are advected into the lee encounter either no further particle growth or sublimation, thus favoring decreased surface precipitation in the lee. This was observed by the DOW radar as a decrease in median Z during this period from 20-30 km upwind to 10-20 km downwind of Battle Pass (Figure 2.12). Below 4 km MSL, median Z remained above 10 dBZ for all upwind profiles and then decreased below 10 dBZ for all downwind profiles. A slight increase in median Z occured at all levels between the 10-20 km and 20-30 km downwind profiles (Figure 2.12). This downwind increase in reflectivity can also be seen in the Hovmöller diagram beyond 20 km downwind after 2030 UTC (Figure 2.2) and indicates a return to orographic ascent and particle growth over the downwind Medicine Bow range (Figures 2.1, 2.2).

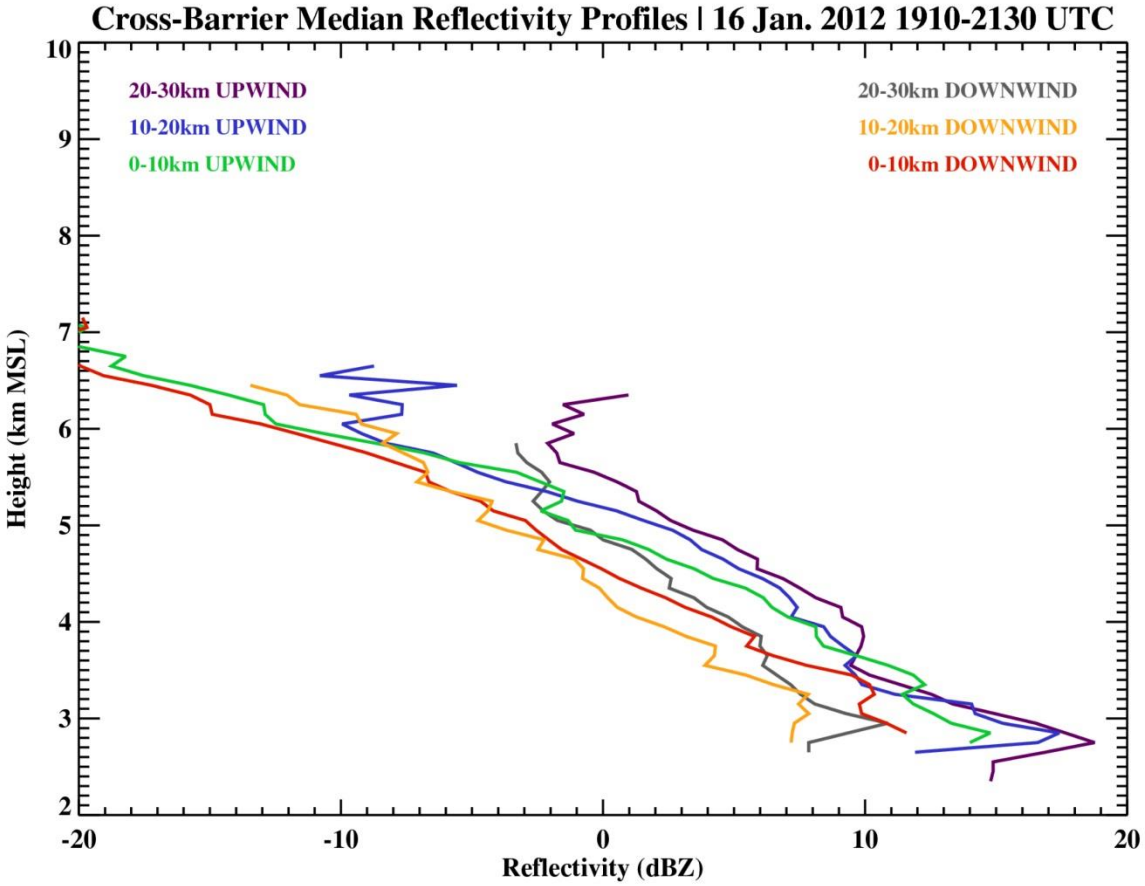

Figure 2.12: Median profiles of reflectivity are shown for cross-barrier transects from upwind-facing (245°-265°) and downwind-facing (70°-85°) DOW RHI scans between 1910-2130 UTC on 16 January 2012. These transects are broken into six 10 km horizontal distances: -30 to -20 km (upwind), +20 to +30 km (downwind), -20 to -10 km (upwind), +10 to +20 km (downwind), -10 to 0 km (upwind), and 0 to +10 km (downwind) from the DOW radar location at Battle Pass.

2.7 Turbulent Motion and Implications for Microphysical Processes

An increase in spectrum width was observed by the MRR between 3.6-4.6 km MSL during the strongest plunging flow from 2010-2120 UTC (Figure 2.10c). Increased spectrum width can be an indication of increased turbulence or fall speed diversity of falling precipitation particles. Because fall speeds of pristine ice crystals vary little with size (Locatelli and Hobbs 1974), turbulence dominated the spectrum

width signal during this time period. The sharp decrease in cross-barrier wind speed below the jet maximum indicated by the 2015 UTC sounding between 3.25-4.6 km MSL (15-30 m s^{-1} km^{-1}; Figure 2.3), which is well above the 10 m s^{-1} km^{-1} threshold identified by HM05, as well as the Doppler radial velocity field in the DOW RHI scans at 2055 UTC (Figure 2.11a) indicate this turbulence was likely shear-generated. Backing of winds in this shear layer, from northwesterly within the decoupled boundary layer to southwesterly above the inversion at 3.5 km MSL, partially contributed to this cross-barrier wind shear, but wind speeds also increased from 10 m s^{-1} to 30 m s^{-1} between 3.25 and 4.5 km MSL (Figure 2.3). Because the MRR is pointing vertically, this turbulent motion indicates rapidly fluctuating air motion, or updrafts and downdrafts. The MRR-observed Doppler velocity CFAD (Figure 2.9b) and 1-minute profiles (Figure 2.10b) show mean downward motion in this turbulent shear layer (-2 to -3 m s^{-1}), associated with the plunging flow above Battle Pass, but small-scale alternating fluctuations between -0.8 and -4.4 m s^{-1} were present. These fluctuations can be related to pockets of overturning cells with 1-2 m s^{-1} updrafts and downdrafts.

Along-barrier UWKA flight legs flown between 1925-1951 UTC indicate turbulence with updrafts up to 2 m s^{-1} within the shear layer between 3.6-4.7 km MSL that appears separate from a turbulent terrain-following boundary layer below 3.6 km MSL (Figure 2.13). Note that the time of the UWKA along-barrier flights lies outside the time when the strongest plunging flow and shear-layer turbulence was identified over Battle Pass (2010-2120 UTC). However, because the synoptic

system is progressing to the southeast during this time and the cross-barrier jet was identified as entering the target region with the advected upper-level reflectivity enhancement by 1920 UTC, the turbulent shear layer should appear to the northwest in the flight legs. This seems to be the case as turbulence within the shear layer is best observed by the WCR to the northwest in flight legs 3 and 4 (pink boxes in Figure 2.13b-c). *In-situ* vertical wind measurements from the UWKA also observed turbulent vertical air motions between ±2 m s^{-1} at flight level (4 km MSL) throughout each flight leg (Figure 2.13). To further quantify the turbulence observed by the UWKA, Figure 2.14 plots the *in-situ* Eddy Dissipation Rate (EDR), the cube root of the rate of dissipation of the turbulent kinetic energy, measured by the MacCready turbulence meter (MacCready 1964) for the same flight legs shown in Figure 2.13. Based on previous classifications (Strauss et al. 2015), EDR thresholds of 0.014, 0.050, 0.125, 0.220, 0.350, and 0.500 $m^{2/3}$ s^{-1} designate turbulence categories 'smooth to light', 'light', 'light to moderate', 'moderate', 'moderate to severe', and 'severe,' respectively. It can be seen that the UWKA generally experienced greater than 'light' turbulence for the majority of the along-barrier flight legs, with the strongest turbulence (moderate to severe) being observed within the turbulent shear layer identified by the pink box in leg 4 (Figure 2.14). However, the turbulence observed within the shear layer by the WCR and UWKA *in-situ* sensors seems to be sub-kilometer scale. Additionally, MRR-observed spectrum width within the shear layer during the UWKA flight times indicates little to weak turbulence was present, at least over Battle Pass (Figure 2.10c).

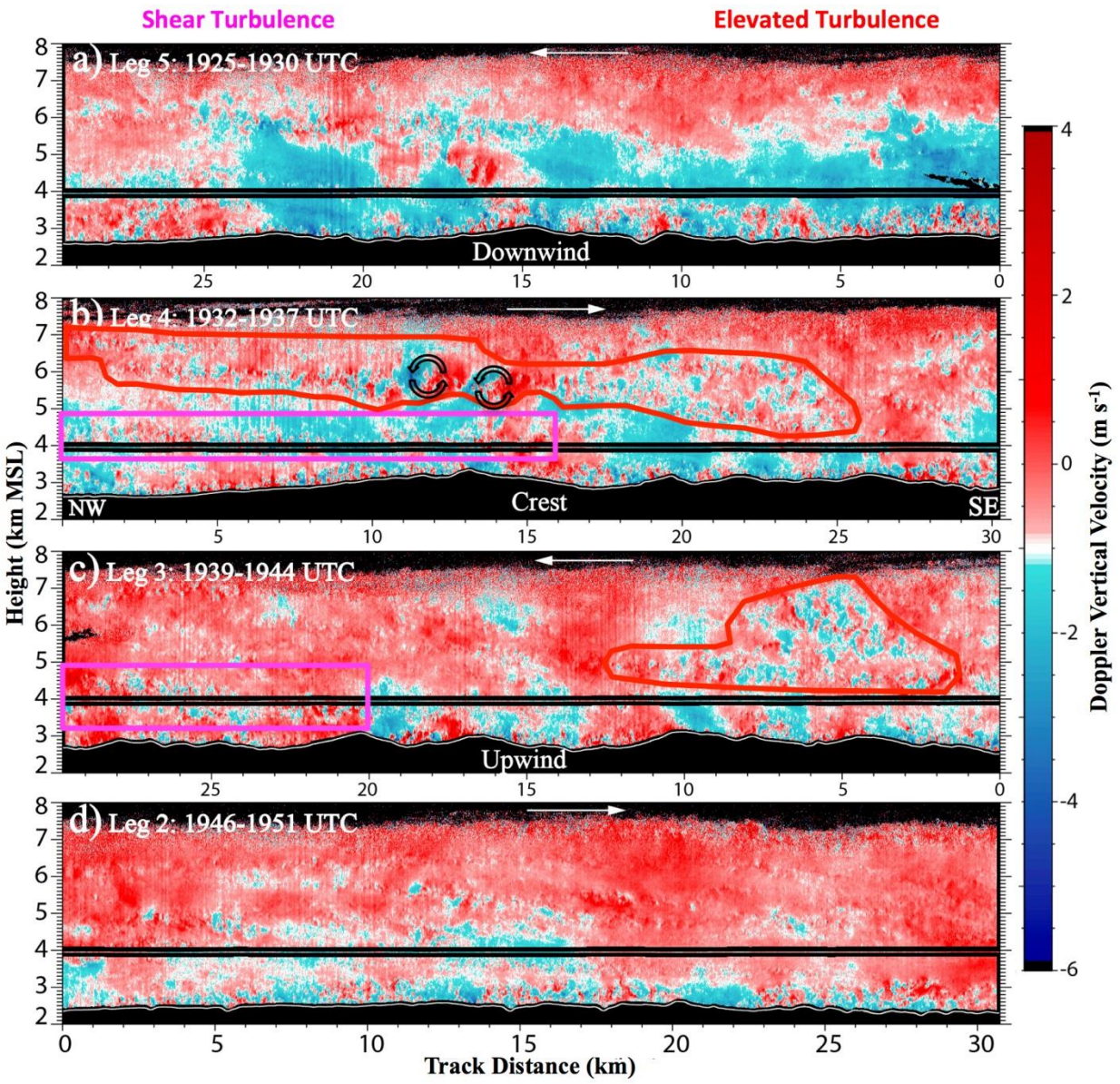

Figure 2.13: Doppler vertical velocity measured by the WCR are plotted for UWKA research flight #4 (RF04) a) leg 5, b) leg 4, c) leg 3, and d) leg 2 of ladder #4 flown between 1925-1951 UTC on 16 January 2012 during ASCII IOP2. The UWKA flight track is located within the radar blind zone (black) near 4 km MSL, and the underlying terrain is visible as the white line below the flight track. 25 Hz vertical velocity measurements from *in-situ* instruments aboard the UWKA are plotted within the WCR blind zone (near 4 km MSL). The flight tracks are all oriented northwest (NW) on the left and southeast (SE) on the right. The direction that the UWKA traveled across each leg is indicated by the white arrow in each panel. Note that track distances are slightly different for each flight leg. See Figure 2.1a for flight leg locations. Notice the Doppler vertical velocity color scale is centered at -1 m s^{-1}, which better depicts air motion as snow generally falls at ~ 1 m s^{-1}. *In-situ* vertical velocity (25 Hz data) plotted within the radar blind zone uses the same color scale but is centered at

0 m s^{-1}. The regions of shear turbulence (pink boxes) and elevated turbulence (red boundaries) are identified and discussed in the text. See text for further details.

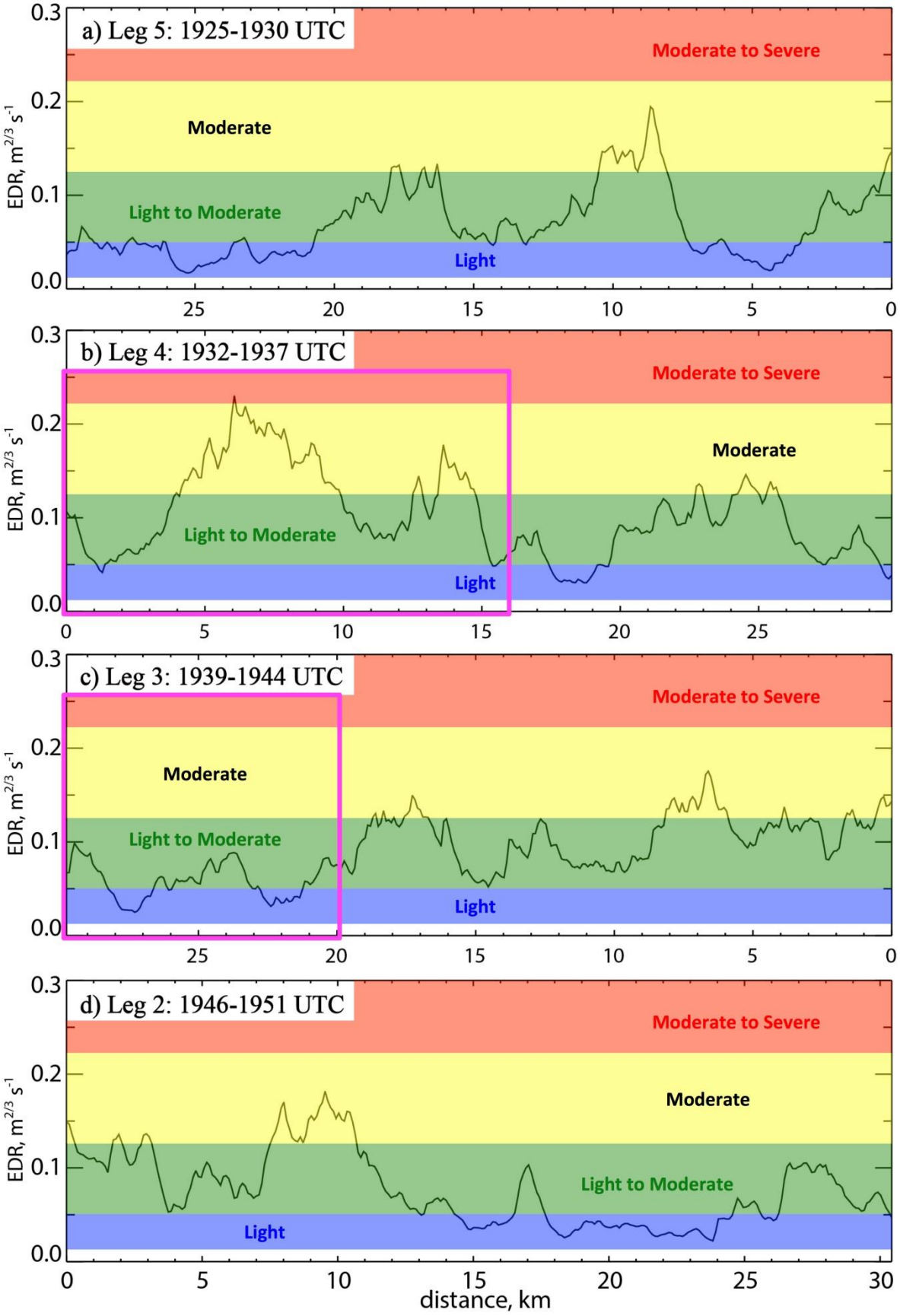
a) Leg 5: 1925-1930 UTC
b) Leg 4: 1932-1937 UTC
c) Leg 3: 1939-1944 UTC
d) Leg 2: 1946-1951 UTC
Moderate to Severe
Moderate
Light to Moderate
Light
EDR, m^2/3 s^-1
0.0
0.1
0.2
0.3
0
5
10
15
20
25
30
distance, km

Figure 2.14: Eddy dissipation rate (EDR) measured by the MacCready turbulence meter (MacCready 1964) aboard the UWKA is plotted for UWKA research flight #4 (RF04) a) leg 5, b) leg 4, c) leg 3, and d) leg 2 of ladder #4 flown between 1925-1951 UTC on 16 January 2012 during ASCII IOP2. Based on previous classifications (Strauss et al. 2015), EDR thresholds of 0.014, 0.050, 0.125, 0.220, 0.350, and 0.500 $m^{2/3}$ s^{-1} designate turbulence categories 'smooth to light', 'light', 'light to moderate', 'moderate', 'moderate to severe', and 'severe,' respectively. Regions where the UWKA flew through the layer of shear turbulence, indicated by the WCR Doppler velocity observations (Figure 2.13), are outlined with a pink box, similar to Figures 2.13 and 2.16. See text for more details.

UWKA flight legs 3 and 4 (1932-1944 UTC) also observed an elevated turbulent layer (red boundaries in Figure 2.13b,c), which was also observed by the Battle Pass MRR as an increase in spectrum width near echo-top (labeled in Figure 2.10c). This elevated turbulence mainly contains sub-kilometer updrafts and downdrafts, but two larger (~ 1 km wide) coherent overturning cells are observed in flight leg 4 between 5-6.5 km MSL with updrafts/downdrafts reaching ± 3 m s^{-1} (see black arrows in Figure 2.13b). It is unclear what induced these overturning cells, but the arrival of the cross-barrier jet during this time likely played a role, either through releasing moist instability or creating shear instability above the jet.

The question is, do these turbulent layers affect the microphysical growth of snow particles? HM05 and MH15 suggest localized enhancements of LWC are generated within the updrafts of observed turbulent overturning cells, which allow more rapid particle growth and fallout through aggregation and subsequent riming. During all flight legs shown in Figure 2.13 (legs 2-5), *in-situ* instruments aboard the UWKA observed no liquid water (not shown). Similarly, the microwave radiometer at Battle Pass observed ILW values < 0.05 mm (Figure 2.4e) with LWC values < 0.01 g m^{-3} above 3.5 km MSL (Figure 2.10b,c). However, during flight leg 1 between 1916-1921 UTC (Figure 2.15), the CDP aboard the UWKA observed peaks in LWC

up to 0.25 g m^{-3} at 4, 7, and 8.6 km flight distances (Figure 2.15e). These LWC spikes are collocated with increased turbulence (EDR > 0.15 $m^{2/3}$ s^{-1}; Figure 2.15c), increased water vapor mixing ratios (max ~ 1.57 g kg^{-1}; Figure 15c), strong updrafts (0.8-2.7 m s^{-1}; Figure 2.15b,d), regions of lower reflectivity (Z < 10 dBZ; Figure 2.15a), and lower ice concentrations (~10 L^{-1}; Figure 2.15e). These strong updrafts create increased cooling and condensation, thus favoring the generation of supercooled liquid water. However, notice that no LWC was observed in an area of higher reflectivity (Z > 10 dBZ) and ice concentration (40-50 L^{-1}) where a similar strong updraft (1.6 m s^{-1}), increased turbulence (max EDR ~ 0.17 $m^{2/3}$ s^{-1}), and increased mixing ratio (1.5 g kg^{-1}) was observed near 23.5 km flight distance (red box; Figure 2.15). One possible mechanism to explain this could be that larger and more numerous snow particles, generated at higher levels in the deep cloud and indicated by the higher Z and *in-situ* ice concentration, fall through this layer of turbulent updrafts and grow through deposition. The cumulative consumption of water vapor from these larger and more numerous ice particles seems to prevent supercooled liquid water generation. The dominance of depositional growth agrees with the snow particles observed at the surface and the reflectivity profiles analyzed in section 4. Figure 2.16 reveals that reflectivity was high (Z > 10 dBZ) near the UWKA flight path during all flight legs shown in Figure 2.13, especially within the turbulent shear layer between 3.6-4.7 km MSL (pink boxes in Figures 2.13b-c, 2.16b-c), which explains why no *in-situ* LWC was observed.

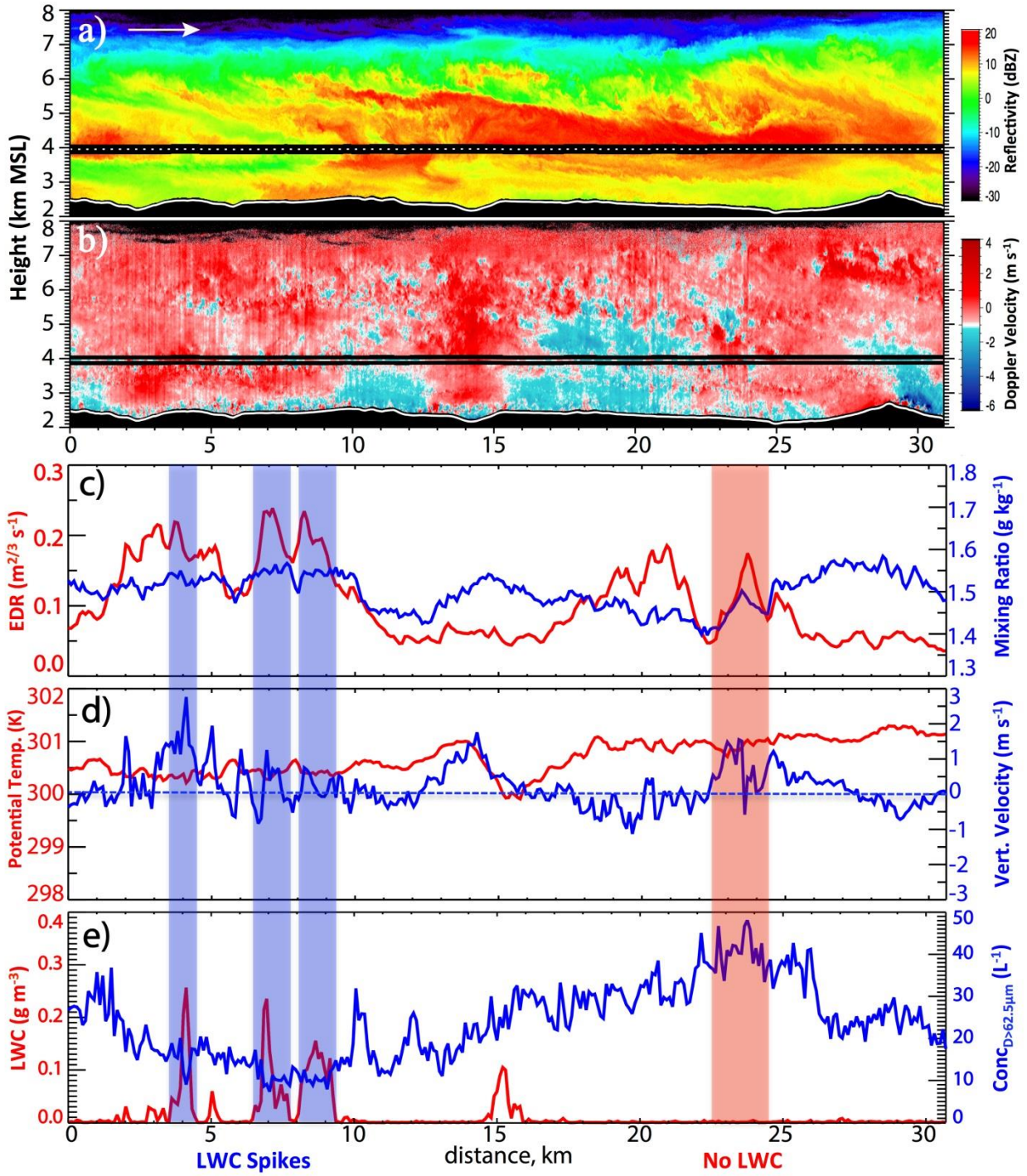

Figure 2.15: a) Reflectivity and b) Doppler vertical velocity observed by the WCR between 1916-1921 UTC 16 January 2012 during flight leg 1 of UWKA research flight #4, ladder #3. *In-situ* measurements of water vapor mixing ratio (g kg^{-1}) and Eddy Dissipation Rate (EDR) are plotted in c). *In-situ* measurements of potential temperature (K) and vertical wind velocity (m s^{-1}) are plotted in d). *In-situ* measurements of LWC (g m^{-3}) and ice concentration per Liter (particle diameters 62.5 µm - 2.5 mm) are plotted in e). See Figure 2.1a for ladder

leg location. A blue dashed line in d) marks the 0 m s^{-1} vertical wind velocity. Regions where vertical wind velocity is above this line identify updrafts, whereas downdrafts are located where vertical wind velocity lies below this line. See text for details.

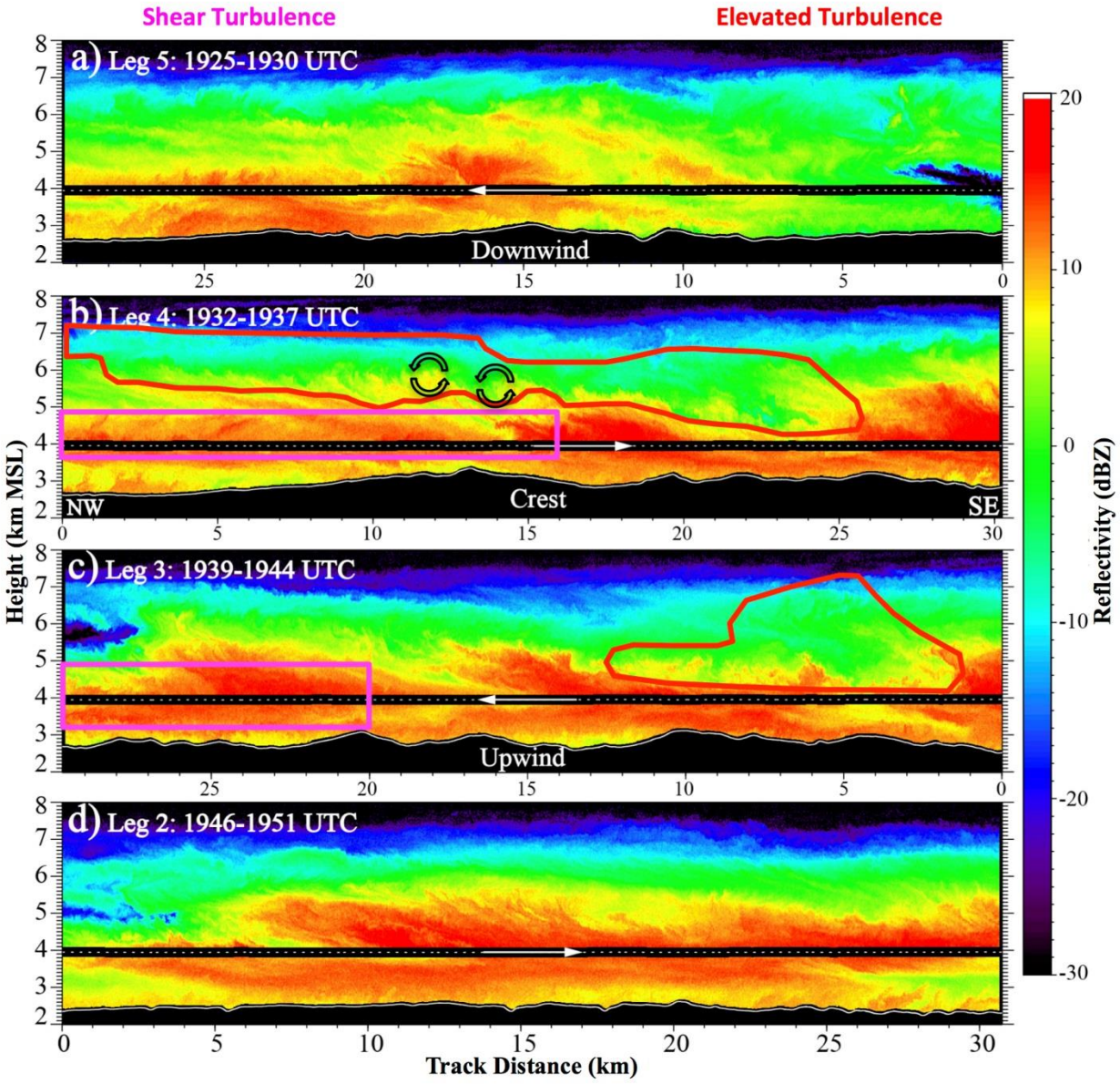

Figure 2.16: As in Figure 2.13, except for reflectivity observed by the WCR. The UWKA flight track is plotted as a dotted white line within the radar blind zone. See Figure 2.13 and text for further details.

Although no in-situ LWC observations are available within the elevated turbulence region, the elevated turbulence seems to occur in lower reflectivity

regions (Z < 10 dBZ) with rapid reflectivity increases (fall streaks) extending below (Figures 2.10a, 2.16b,c). Increased reflectivities were also observed by the WCR to extend from the center of the two overturning cells (Figure 2.16b), indicating a net particle growth rather than offsetting growth and sublimation within the updraft and downdraft, respectively. These observations indicate the elevated turbulence drove the majority of snow growth within this deep cloud system at the time of the UWKA flights. However, the observed large dendritic aggregates at Battle Pass during this time (section 4) indicates the turbulent shear layer between 3.6-4.7 km MSL may have enhanced the aggregation of the snow particles falling from the elevated turbulence region. This agrees with the nearly uniform region of high reflectivity (Z > 10 dBZ) observed within the shear turbulence region (Figure 2.16b-c) as aggregation would increase particle sizes and thus backscattered power.

Consistent increases in Z were observed by the MRR within and below the jet-induced turbulent shear layer during its peak strength between 2010-2120 UTC (Figure 2.10). Vertical turrets of increased reflectivity above the main turbulent shear layer (3.6-4.5 km MSL) observed by the MRR at 2033, 2040, 2050, and 2056 UTC also seem to be collocated with weaker yet enhanced turbulence up to 6 km MSL (Figure 2.10a,c). Also note the decrease in Z observed by the MRR between 2040-2050 UTC (Figure 2.10a). This temporary feature is collocated with a weakening of the plunging flow (Figure 2.10b) and reduced shear turbulence (Figure 2.10c), indicative of a weaker cross-barrier jet. Increased turbulence was also observed by the MRR below 4 km MSL, near the -15°C dendritic growth zone,

before 1930 UTC and after 2125 UTC (Figure 2.10c). This coincides with rapid reflectivity increases observed by the MRR (Figure 2.10a) and DOW radar (Figure 2.7a) below 4 km MSL and the presence of aggregates at the Battle Pass surface (Figure 2.8).

Collectively, these observations suggest that the mid-level cross-barrier jet and its respective turbulent shear zone below the jet maximum are closely tied to turbulent overturning motion and rapid snow growth. These rapid snow growth regions frequently occur in pockets with distinct fall streaks extending below regions of increased turbulence. Snow growth due to the shear-induced turbulence occurred through deposition and aggregation due to the abundance of ice crystals from the deep, cold cloud system.

2.8 Discussion

The orographic precipitation system analyzed in this paper is similar to previously studied systems over the Park Range of Colorado. The post-frontal period analyzed in this analysis resembles the deep stratiform precipitation system depicted by the conceptual model shown in Figure 13b of Rauber and Grant (1986). Similar to Rauber and Grant (1986), the deep clouds observed in this analysis contained very little liquid water. They suggest the reduction in liquid water is due to the increased ice crystal flux (concentration) from deeper and colder cloud tops, which increases the bulk diffusional growth rate and limits supercooled liquid water production. Observations from our analysis agree with this theory. Surface snow particles observed at Battle Pass are similar to snowfall observed by Rauber (1987),

which mainly consisted of irregular and plate-like crystals, dendrites, and aggregates, thus emphasizing the dominance of deposition and aggregation within these cold continental environments.

Previous observations have also indicated the importance of decoupled flow, namely low-level barrier jets and mid-level cross-barrier jets, for precipitation enhancement (e.g., Marwitz 1983; Overland and Bond 1995; Yu and Smull 2000; Yu and Bond 2002; Neiman et al. 2002, 2004; Loescher et al. 2006; Olson et al. 2007; Olson and Colle 2009). In the case analyzed here, the flow was decoupled but the northwesterly surface flow in this case was part of the post-frontal airmass and not a result of deflected airflow. Medina and Houze (2003), HM05, and Rotunno and Houze (2007) discovered small-scale precipitation enhancements in overturning cells as a result of shear dynamic instability. Our observations agree with HM05 and MH15 in that increased turbulence favors increased snow growth, and that the presence of a cross-barrier jet favors increased turbulence through vertical wind shear. However, in the colder continental environment of Wyoming, enhanced depositional growth rather than riming was found to result from this shear-induced turbulence. Aggregation was observed at the surface when 1) enhanced growth aloft allowed larger snow particles to fall through the turbulent shear layer and 2) turbulence was located near the -15°C dendritic growth zone. The location of the mid-level cross-barrier jet and turbulent shear layer are similar to HM05 in that they formed at the top of a cold, decoupled surface layer. However, the decoupled surface layer in this analysis was associated with an Arctic air mass that extended

above mountaintop rather than the blocked flows observed below mountaintop by HM05. In fact, the 2015 UTC sounding indicates some moist instability within the upwind decoupled surface layer (Figure 2.3) and WCR along-barrier transects (Figures 2.13, 2.15b) show air flowing up and over individual peaks within this decoupled surface layer (updrafts on northwest-facing slopes, downdrafts on southeast-facing slopes). HM05 also suggest turbulent motions within the shear layer may cause small localized pockets of supercooled liquid water. Small pockets of supercooled liquid water were observed by the WCR in our case, but they were only observed outside regions of increased reflectivity and ice crystal concentration.

2.9 Conclusions

The role of turbulent shear instability associated with a post-frontal cross-barrier jet on precipitation formation and fallout has been investigated using a suite of high-resolution ground-based and airborne radars and *in-situ* instruments. Observations were taken during IOP2 (16 January 2012) of the 2012 ASCII field project in a deep, post-frontal winter orographic precipitation system over the Sierra Madre mountain range of Wyoming. Surface snow gauge observations at mountaintop (Battle Pass) indicated that 4 mm of liquid-equivalent precipitation fell during this post-frontal period between 1910-2130 UTC with decreasing intensity (1.3-2.9 mm hr^{-1}).

Dual-polarization radar-based analysis indicated that snow crystals primarily grew through water vapor deposition near cloud top and grew in size as particles fell to the ground, a primarily stratiform precipitation signal. Microwave

radiometer and airborne *in-situ* cloud physics probes measured little to no supercooled liquid water within the deep precipitating clouds. Enhanced reflectivity (Z > 20 dBZ) was advected from upwind of the target area between 1910-2015 UTC, which was associated with the arrival of a mid-level cross-barrier jet (~ 30 m s^{-1}). Low-level (< 4 km MSL) reflectivity enhancements were observed within 15 km of the upwind side of the mountain between 2015-2130 UTC, likely due to rapid dendritic growth and aggregation. A post-frontal airmass inversion at 3.5 km MSL separated post-frontal northwesterly, along-barrier, slightly moist unstable flow from a southwesterly cross-barrier jet in stable air above. While wind shear characteristics were similar to previously observed blocked low-level flow, the northwesterly flow observed in the boundary layer in our analyzed case is part of the low-level post-frontal Arctic airmass and not a result of deflected airflow. In fact, the Arctic airmass extended above mountaintop, yet orographic ascent upwind and plunging flow downwind was observed in the cross-barrier flow above.

Shear-induced turbulence and overturning cells were observed between the top of this Arctic airmass and the cross-barrier jet maximum wind speed (~ 30 m s^{-1}). An elevated layer of turbulent overturning cells was also observed by the WCR earlier in the analysis period and collocated with the arrival of the mid-level cross-barrier jet. These turbulent regions created pockets of rapid snow growth through enhanced depositional and aggregational processes. No liquid water was observed in the vicinity of the overturning cells, as suggested by HM05 and MH15. The lack of liquid water is likely due to the increased concentration of ice particles falling from

the deeper cloud above, which consumes water vapor too fast to allow liquid drops to grow. This hypothesis is supported by previous research (Rauber and Grant 1986) and WCR and *in-situ* UWKA data, which shows that turbulent updrafts favor cooling and liquid water generation, but only outside regions of increased reflectivity and ice crystal concentration.

Previous studies investigating the role of shear dynamic instability on precipitation formation have focused on events with large moisture fluxes and the presence of supercooled liquid water along more coastal mountain ranges (HM05; MH15). This study highlighted the effects of shear dynamic instability on snow growth for an inner-mountain range with lower moisture flux and the absence of supercooled liquid water. The analysis presented in this paper also focuses on a smaller mountain range, whereas previous research has focused on larger mountain barriers.

The results of this paper suggest that 1) shear-induced turbulent overturning cells do exist over cold continental mountain ranges like the Sierra Madre range, 2) the presence of cross-barrier jets favor these turbulent shear zones, 3) this turbulence is a key mechanism in enhancing snow growth, and 4) snow growth enhanced by turbulence primarily occurs through deposition and aggregation in these cold (< -15°C) post-frontal continental environments.

2.10 Acknowledgements

We would like to thank the Center for Severe Weather Research staff for recording and processing the DOW radar data, Mike Dixon at NCAR for assisting

with the Radx radar software, Evan Kalina and Yang Yang for taking snow crystal photographs at Battle Pass, Samuel Haimov, Yang Yang, and Xiaoqin Jing for providing the IDL analysis code for the WCR data and WCR radar specifications used in ASCII, and the anonymous reviewers for their helpful suggestions to improve this paper. This work was partially supported by the AMS Graduate Fellowship Program and the Cooperative Institute for Research in Environmental Sciences (CIRES). The ASCII experiment was a collaborative field study between the University of Wyoming, University of Colorado at Boulder, NCAR, and the University of Illinois at Champaign-Urbana and funded through NSF grant AGS-1058426. Any opinions, findings, or recommendations expressed in this publication are those of the authors and do not necessarily reflect the views of the National Science Foundation.

3 Investigating A Squall Line Interaction with the Southern Appalachians Using High-Resolution Radar and Surface In-Situ Observations During IPHEx

This chapter is adapted and reformatted from:

Aikins, J., K. Friedrich, M. Hughes, and R. Cifelli, 2018: Investigating A Squall Line Interaction with the Southern Appalachians Using High-Resolution Radar and Surface In-Situ Observations During IPHEx. To be submitted to *Monthly Weather Review* May 2018.

3.1 Abstract

This study utilizes a high-resolution observational network from the Integrated Precipitation and Hydrology Experiment (IPHEx) to document the orographic modification of a prefrontal squall line that passed over the southern Appalachian Mountains of southwestern North Carolina on 15 May 2014. This squall line was embedded within an Atmospheric River (AR), where southerly low-level moisture transport was impeded by the southern Appalachian Mountains, favoring rapid fallout of precipitation on its southeastern slopes. High-resolution NOXP and NPOL radar observations show that a prominent mountain ridge along the southwestern boundary of the Pigeon River Basin weakened the squall line leading-line convection as it passed into the lee, with a maximum in intensity near the highest terrain of this ridge. Surface rain gauge and disdrometer observations show a maximum in rain accumulation along this southeast/northwest oriented ridge with decreasing rainfall farther northeast along the lee slope and into the

central valley within the Pigeon River Basin. Comparison of the mountainous domain over and southwest of the Pigeon River Basin with the flatter plains domain to the southeast of the Pigeon River Basin reveals that the Appalachian Mountains were more efficient at releasing convective instability and maintaining hydrometeor growth through orographic lift, but more intense convection was able to persist over the flatter terrain. Comparison with previous literature of the squall line interacting with terrain is discussed. This case analysis is also placed into context with previous literature that looked at ARs and extreme precipitation events within the southeastern US.

3.2 Introduction

Organized convective systems have fascinated scientists and the general public due to their extreme impact on people and the environment. This led to decades of observational and modeling research that identified what drives these mesoscale convective systems (MCSs; e.g. Houze 2004, Trapp 2013). However, most previous research has largely focused its attention on MCSs within regions devoid of mountainous terrain in tropical locations (e.g., Houze 1977; Chong et al. 1987) and on the Great Plains of the United States (e.g., Ogura and Liou 1980; Bluestein and Jain 1985; Bluestein et al. 1987; Houze et al. 1989; Houze et al. 1990; Blanchard 1990; Parker and Johnson 2000). This focus was helpful in generating a conceptual model depicting the kinematics of MCSs (e.g. Houze et al. 1989), but it leaves an interesting question un-answered. What happens when these convective systems interact with mountainous terrain? This study aims to start answering

that question by revealing the structural and microphysical changes that an MCS underwent on 15 May 2014 while impinging on the southern Appalachian Mountains using high-resolution research radar and surface in-situ observations collected during the Integrated Precipitation and Hydrology Experiment.

Specifics on how mountains modify passing MCSs have been hypothesized through modeling (Frame and Markowski 2006), but observations are limited and have focused on forecasting perspectives (Teng et al. 2000; Keighton et al. 2007). Squall lines are a commonly observed type of MCS in the US, which typically consist of a linear region of multicellular convection followed by a trailing stratiform region, although leading and parallel stratiform structures have been observed in different wind environments (Parker and Johnson 2000). Previous studies have largely specifically focused on squall line interactions with terrain. Frame and Markowski (2006) modeled the interaction of a squall line with an idealized sinusoidal mountain ridge and found 1) orographic enhancement of rainfall and convective updrafts occurred on the upwind slope of the ridge, 2) convection and rainfall were suppressed on the lee slope due to the partial blocking and more shallow cold pool that descended, and 3) re-invigoration of convection occurred downwind of the lee slope due to a hydraulic jump created by the cold pool that made it over the ridge. They also noted that the mountain height has to be at least 600 m above the surrounding terrain for this discrete propagation of the squall line to occur, and that higher mountain heights lead to decreased squall line intensity in the downwind environment due to the increased cold pool blockage. However, this

numerical modeling study only scratched the surface of MCS interaction with terrain as only one horizontally-homogeneous atmospheric setup was investigated with convective available potential energy (CAPE) set to 2200 J kg^{-1}. Letkewicz and Parker (2010, 2011) expanded on this modeling work by adjusting environmental instability and wind parameters to study linear MCSs that did and did not cross the Appalachians. They found that instability (specifically most unstable CAPE, MUCAPE) was the primary factor determining whether MCSs can re-invigorate in the lee of the Appalachians, and that increased mean winds favors stronger upwind enhancement and lee suppression of the MCS due to orographic flows. Observationally, only approximately 10% of MCSs that move into the southern Appalachians actually maintain their organization over the mountains (Parker and Ahijevych 2007), indicating there are more complex processes involved. Teng et al. (2000) used Doppler radar observations to document some complex processes within a subtropical squall line interacting with the mountains of Taiwan (up to 4000 m peaks) during the evening of 16 May 1987. They found that the mountains slowed the progression of the squall line and ultimately lead to its dissipation due to the reduction of the front-to-rear inflow (Houze et al. 1989) of warm moist air. In fact, they observed the drier rear inflow jet (Smull and Houze 1987) get lifted into the convective updraft through orographic lifting, which reduced instability and updraft strength leading to reduced echo-tops. To the authors' knowledge, there have been no other observational studies documenting squall line interactions with mountainous terrain. The limited studies described above all suggest that mountain

barriers can be detrimental to squall lines due to the modification of low-level convergence by the surface cold pool, a key element in maintaining their strength. However, more observations of MCS interactions with mountainous terrain are needed, especially with today's advanced instrumentation.

The Integrated Precipitation and Hydrology Experiment (IPHEx) dataset provides a great opportunity to explore MCS interactions with mountainous terrain. IPHEx is a ground validation field campaign for the new Global Precipitation Measurement Core satellite, sponsored by NASA's Precipitation Measurement Missions Program. The IPHEx field campaign took place between October 2013 and October 2014 in the southern Appalachian Mountains, with a specific focus on the Pigeon River Basin in western North Carolina and eastern Tennessee (Figure 3.1). This region now has ample long-term precipitation and hydrological monitoring networks (Barros et al. 2014), and additional instruments were deployed during an Intensive Observational Period (IOP) between 1 May and 15 June 2014 (see section 2 and Figure 3.1). IPHEx coincided with the NOAA Hydrometeorological Testbed Southeast Pilot Study (HMT-SEPS), which focused on improving quantitative precipitation estimation (QPE) and forecasting (QPF) in the Upper Catawba watershed where additional meteorological instrumentation was deployed (e.g., Tao et al. 2016). A goal of IPHEx and HMT-SEPS is to better characterize the small-scale orographic precipitation mechanisms in the southern Appalachians utilizing the dense network of in-situ and remote sensing platforms. The analysis in this study will contribute to this goal through an in-depth case study of the orographic

modification of a squall line by the southern Appalachian Mountains on 15 May 2014.

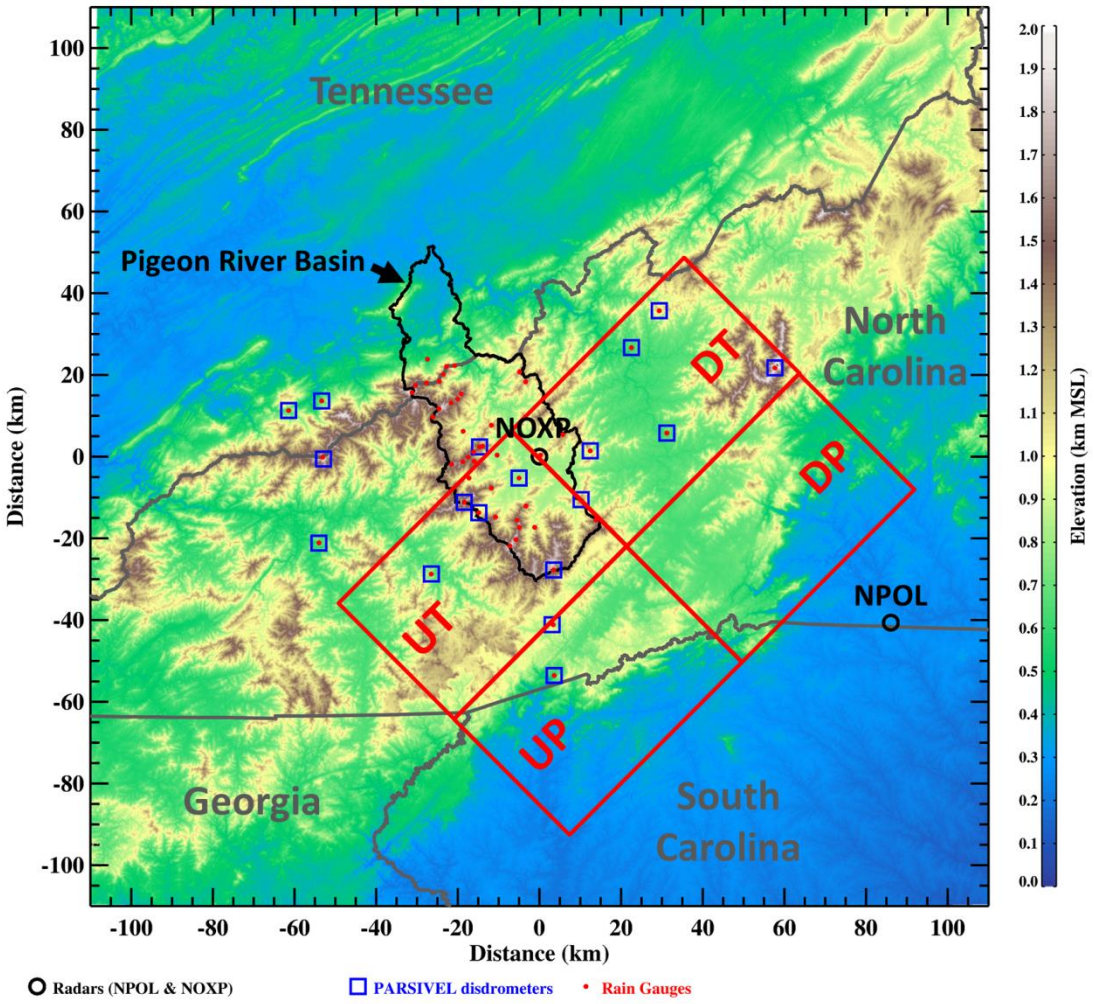

Figure 3.1: IPHEx terrain elevation map centered on the NOXP radar location. The location of scanning radars (NOXP and NPOL), PARSIVEL disdrometers, and rain gauges are overlaid and labeled on the terrain map. The Pigeon River Basin watershed is outlined in black and state borders are outlined in grey for reference. The terrain elevation colorbar is displayed on the right and ranges between 0 and 2.0 km above mean sea level (MSL). The terrain elevation data is from the United States Geological Survey (USGS) National Elevation Dataset (NED) with a 1-arc-second resolution (~ 30 meters). The Upwind Terrain (UT), Upwind Plains (UP), Downwind Terrain (DT), and Downwind Plains (DP) analysis domains are outlined in red. See text for further details.

The objectives of this paper are to (i) identify changes in squall line structure and intensity as it passes over the southern Appalachian Mountains utilizing high-resolution dual-polarization radar observations and (ii) relate these changes to

surface precipitation characteristics using in-situ rain gauge and disdrometer observations. Documenting the time evolution of the squall line passage over terrain will provide insight into the basic question: what happens when a squall line interacts with terrain?

This paper is outlined as follows. A description of the main instrumentation and data processing used in this analysis is presented in section 3.3. An overview of the synoptic setup on 15 May 2014 is described in section 3.4. A detailed radar analysis of a squall line propagating from southwest to northeast over the IPHEx region is presented in section 3.5. Surface rain gauge and disdrometer observations during this squall line passage are discussed in section 3.6. Finally, a discussion of the major results from this study is presented in context with previous research in section 3.7.

3.3 Instrumentation, Data, and Methods

3.3.1 NOXP Dual-Polarization X-band Radar

The National Oceanic and Atmospheric Administration (NOAA) X-POL (NOXP) radar is a mobile scanning dual-polarization X-band Doppler radar owned by the National Severe Storms Laboratory (NSSL). During IPHEx it operated at a frequency of 9.41 GHz (3.22 cm) with a pulse repetition frequency (PRF) of 1350 Hz, resulting in a maximum range of 111 km with range gate spacing of 150 m. The NOXP radar has a parabolic dish with a half-power beam width of 0.9 degrees. The NOXP radar was positioned on a mountain ridge at 1200 m elevation on the northeast side of the Pigeon River Basin (Figure 3.1), which allowed the best view of

precipitation along a 180° sector from azimuths 135° to 315° due to beam blockage by terrain and near-radar obstacles (Figure 3.2). The NOXP radar scanned in both plan position indicator (PPI) and range height indicator (RHI) modes during IPHEx, but only PPI scans were available for the case studied in this analysis. The PPI scan strategy included scanning a full 360° in azimuth at 15 elevations between 0.1° and 19.5° over ~5 minutes.

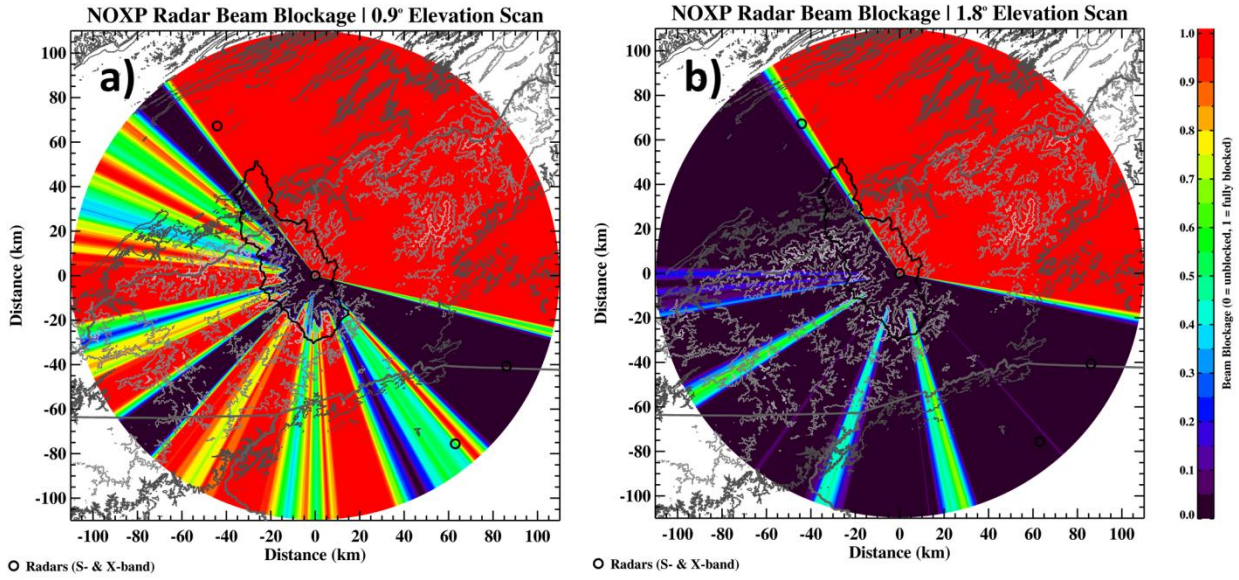

Figure 3.2: NOXP radar beam blockage at a) 0.9° and b) 1.8° elevation. USGS terrain elevation is contoured in grey every 500 meters, with darker grey indicating lower elevation and lighter grey indicating higher elevation. The Pigeon River Basin is outlined in black for reference, similar to Figure 3.1.

NOXP radar data was processed by the new self-consistent with optimal parameterization attenuation correction and rain microphysics estimation algorithm (SCOP-ME; Anagnostou et al. 2013; Kalogiros et al. 2013; Kalogiros et al. 2014). This algorithm calculated attenuation correction for reflectivity and differential reflectivity (ZDR) fields, estimated melting layer levels, and calculated rain microphysical parameters, including rain rate, median volume diameter, and

intercept and shape parameters of normalized Gamma drop size distributions (DSDs). The attenuation and melting layer fields output by the SCOP-ME algorithm were further corrected for high-elevation PPI scans where no melting layer was detected by interpolating melting layer heights over time and using estimated melting layer heights from atmospheric soundings. Attenuation correction values within and above the interpolated melting layer were set to the maximum attenuation correction value found along each ray and below the melting layer. Note that reflectivity and ZDR fields are only corrected for rain attenuation. Attenuation by mixed precipitation within the melting layer and hail are not corrected. NOXP radar data are removed where calculated beam blockage exceeds 50%. Additionally, non-meteorological echoes are removed below the melting layer (rain only) for i) low correlation coefficient (< 0.8), ii) a combination of low reflectivity (< 10 dBZ) and large ZDR (≥ 3 dB), iii) low reflectivity (< 0 dBZ) and highly negative ZDR (< -1.5 dB), and iv) low reflectivity (< 0 dBZ) and ZDR > 1 dB. This de-cluttering also removed any ground clutter that may still be present, although ground clutter was removed in real-time by the NOXP translation software.

Corrected NOXP radar fields were then interpolated onto 3-dimensional Cartesian grid volumes using the Radx software (www.eol.ucar.edu/software/radx). Grid spacing of 500 meters in the horizontal and 250 meters in the vertical were used, with the grid covering the 220 x 220 km^2 area centered on the NOXP radar location. This region, shown in Figure 3.1, will be considered the IPHEx region for

the purposes of this study. A second set of gridded volumes were also created with the grid rotated -45° from North to orient the x- and y-axis perpendicular and parallel to the squall line propagation direction, respectively (see section 4).

3.3.2 NPOL Dual-polarization S-band Radar

The National Aeronautics and Space Administration (NASA) S-band dual-polarimetric radar (NPOL) is a fully transportable and self-contained scanning S-band (10.65 cm) dual-polarimetric, Doppler research radar owned and operated by NASA's Wallops Flight Facility. The NPOL radar was positioned 95 km southeast (115°) from the NOXP radar near the North/South Carolina border at an elevation of 306 m (Figure 3.1). It operated with a PRF of 1100 Hz, range gate spacing of 125 m, and maximum range up to 150 km. The NPOL antenna is 8.5 m in diameter with a 0.95° horizontal and vertical beam width. During IPHEx, the NPOL radar scanned in high-resolution PPI, RHI, and PPI sector (PPS) modes with nearly continuous operations throughout the IPHEx IOP period. PPI rain-mapping scans were run for a full 360° azimuth sweep over three elevation angles at 1.0°, 1.5°, and 2.0°. PPS scans were occasionally run over user-selected 90° azimuth sectors when precipitation was impacting the IPHEx region, which consisted of 13 scan elevations between 1.5° and 8.5°. RHI scans were not used in this analysis. The NPOL dataset used in the analysis for this paper is considered "version 1" (Wolff and Marks 2015) and was quality-controlled following Pippett et al. (2013).

PPI and PPS scans were grouped together into full radar volumes and interpolated to a 3-dimensional Cartesian grid using the Radx software

(www.eol.ucar.edu/software/radx) with the same horizontal (500 m) and vertical (250 m) grid resolution used for the NOXP radar gridding. These gridded NPOL volumes were available every 3 minutes during the 15 May 2014 case and were matched to the same Cartesian grid used for the NOXP radar data. Note that not every gridded volume includes PPI and PPS scans (15 scans total) due to changing scan patterns, so low-level observations (from the 3 PPI scans) are sampled more frequently than upper-levels (from the 13 PPS scans).

A mosaicked radar reflectivity field was created for each NOXP 3-dimensional Cartesian radar volume by matching the closest NPOL volume start time (within 5 minutes). The maximum reflectivity value was chosen in the mosaicking for each co-located NOXP/NPOL grid cell. Analysis of all co-located NOXP and NPOL grid cells for each time-matched volume during the analysis period (0000-0430 UTC 15 May 2014; see section 4) shows a small mean negative NOXP reflectivity bias (-2.4 dB), likely due to incomplete attenuation correction, which is more significant at the NOXP X-band wavelength.

3.3.3 Rain Gauges

A total of 64 tipping bucket rain gauges were deployed within the IPHEx region between 1 May and 15 June 2014, with 37 reliable gauges available from the Duke University network and 20 reliable gauge pairs available from the NASA dual tipping bucket rain gauge network during the analysis period on 15 May 2014 (Figure 3.1). The Duke rain gauge network consisted of 6 reliable gauges with a tip resolution of 0.2 mm (RG0** gauges), 22 reliable gauges with a tip resolution of 0.1

mm (RG1**, RG303S, and RG4** gauges), and 9 reliable gauges with a tip resolution of 1.0 mm (RG3** gauges). All Duke gauges have a temporal resolution of 1 second. Duke gauge accumulation data were calibrated for each instrument and included a quality flag based on observations during regular maintenance, which identified times when the gauge was clogged or knocked over, a time shift was detected and corrected, and data was missing. The NASA dual gauge network consisted of two co-located Met One model 380 tipping bucket gauges with tip resolutions of 0.254 mm and temporal resolution of 1 second. Version 2 of the NASA dual gauge data was used in this analysis (Petersen et al. 2016). Gauges were considered reliable if their rain accumulation periods lined up with precipitation features identified by the NOXP/NPOL reflectivity mosaic and if the gauge was not clogged, knocked over, or contained missing data within the analysis period on 15 May 2014. Two gauges were omitted from analysis due to being clogged by debris, two gauges were omitted due to missing data, and three low-resolution gauges (1 mm tip resolution) were omitted due to a higher resolution gauge (0.1 mm tip resolution) being co-located.

Rain gauge accumulations from individual tips were accumulated and re-sampled to a continuous1-minute time series over the IPHEx IOP (1 May - 16 June 2014). The gauge with the largest accumulation from the NASA dual gauge pairs was used in this analysis because of known under-catch issues with rain gauges due to mechanics, wind, clogging, and evaporation (e.g., Duchon and Essenberg 2001, Duchon and Biddle 2010, Duchon et al. 2014). In general, rain gauge under-catch

errors increase with wind speed and rain rates. NASA Met One rain gauges have a reported mechanical accuracy of ±0.5% at rain rates of 13 mm h^{-1} and ±1% at 25-75 mm h^{-1} (Petersen et al. 2016). Although a complete intercomparison analysis is beyond the scope of this paper, three co-located Duke (0.1 mm resolution) and NASA dual rain gauges showed agreement within +/- 7% for a 12-hour period on 15 May 2014. Additional information on rain gauge accuracy can be found in Ciach (2003) and Tokay et al. (2010).

3.3.4 PARSIVEL Disdrometers

A total of 24 particle size and velocity (PARSIVEL) optical disdrometers (Löffler-Mang and Joss 2000) were deployed within the IPHEx region, with 11 PARSIVEL 1st generation (P1) and 11 PARSIVEL 2nd generation (P2) instruments available with reliable measurements during the 15 May 2014 case analyzed in this paper (Figure 3.1). PARSIVEL disdrometers use a laser beam (180 mm long x 30 mm wide x 1 mm thick) to measure the number of drops across 32 diameter and 32 fall velocity bins between 0-26 mm and 0-20 m s^{-1}, respectively. However, the first two diameter bins are considered unreliable due to low signal to noise, so only drops between 0.25-26 mm can be detected. This drop size distribution (DSD) matrix is collected every 10 seconds.

PARSIVEL measurements were processed separately by Duke University (11 P1, 3 P2) and NASA (8 P2), leading to slightly different datasets. NASA P2 drop matrices were quality controlled to remove suspicious measurements by removing individual drop counts with observed fall velocities exceeding +/- 50% from the

expected terminal fall velocity for rain drops (Beard 1976), similar to previous studies (e.g., Jaffrain and Berne 2011; Tokay et al. 2013; Tokay et al. 2014). Duke P1 and P2 data do not include this drop removal quality control technique and raw matrix observations were not available. Normalized drop concentrations (m^{-3} mm^{-1}) using observed drop fall velocities and mean PARSIVEL diameter bins corrected for oblateness (Beard 1976) were calculated every one minute for NASA P2 corrected diameter bins (equation 6 of Tokay et al. 2014). Duke P1 and P2 normalized drop concentrations were also calculated every one minute, but terminal fall velocities and mean raw PARSIVEL diameter bins were used because observed fall velocities were not available. A terminal fall velocity function was adapted for Duke PARSIVEL DSD calculations using equation 5b from Gossard et al. (1992) for drop diameters 0.11-0.6 mm, equation 24 from Atlas (1973) for drop diameters 0.6-5.0 mm, and a constant maximum terminal velocity value for drop diameters greater than 5 mm equal to the Atlas (1973) solution at a drop diameter of 5 mm. These fall velocities were adjusted to an air pressure of 950 mb and temperature of 10°C using a density estimates from Beard (1977), which is more representative of the atmosphere at higher elevation disdrometer locations within the southern Appalachians. This fall velocity function is within 0.2 m s^{-1} of the NASA terminal fall velocity function used for drop rejection at all PARSIVEL diameter bins up to 8 mm. Integral DSD parameters, including total drop concentration (m^{-3}), liquid water content (g m^{-3}), rain rate (mm h^{-1}), reflectivity in the Rayleigh regime (dBZ), and mean mass-weighted diameter (mm), were then calculated for all 1-minute

normalized DSDs (Testud et al. 2001). Finally, cumulative rain accumulation was calculated from 1-minute DSD-calculated rain rates for all PARSIVELs.

Comparison of PARSIVEL rain accumulations with collocated rain gauges during the analysis period between 0000-0430 UTC 15 May 2014 revealed a 31% (31%) bias (absolute bias) for all Duke P1 and a -24% (24%) bias (absolute bias) for all NASA P2, indicating Duke P1 overestimate and NASA P2 underestimate DSD-derived rain accumulations. This is in agreement with previous findings where it was found that P1 instruments overestimate large drop concentrations (diameters > 2.44 mm) leading to larger integral rain parameters (Tokay et al. 2013), whereas P2 instruments measured slower fall velocities compared to terminal fall velocities for drop diameters 1 mm and larger due to a software bug, which resulted in underestimation of rain rates (Tokay et al. 2014). Similar to these previous findings, the P2 instruments are better than P1 at estimating rain accumulation and DSDs, therefor the analysis in this paper will largely focus on P2 measurements.

3.4 Atmospheric Setup - 15 May 2014

The IPHEx region was located in the warm sector of a strengthening extratropical low pressure system between 0000 UTC and 0600 UTC 15 May 2014 (Figure 3.3). Upper-level 250 mb North American Regional Reanalysis (NARR) maps show a digging high-amplitude trough centered over the central US with strong south-southwesterly flow (50-80 m s^{-1}) to the east of the trough axis, extending from northern Louisiana through Lake Superior and well into Canada (Figure 3.3a,d). Similarly, NARR 500 mb geopotential height maps show this trough

with strong south-southwesterly flow (30-45 m s^{-1}) over the Mississippi River valley between Louisiana and southern Illinois, coinciding with the strongest geopotential height and temperature gradients (baroclinic zone) along the eastern edge of the trough (Figure 3.3b,e). An interesting tongue of enhanced southerly flow (20-25 m s^{-1}) appears at 500 mb centered over the Alabama-Georgia border at 0000 UTC 15 May (Figure 3.3b), well ahead of the main baroclinic zone associated with the trough. This region of increased winds further enhanced up to 32 m s^{-1} and shifted eastward over the IPHEx region by 0600 UTC 15 May (Figure 3.3e). A similar region of enhanced southerly flow (20-25 m s^{-1}) was observed at 700 mb (not shown). NOAA Weather Prediction Center (WPC) surface analyses indicate this region of enhanced southerly flow was co-located with a surface low-pressure trough ahead of the surface cold front at 0000 UTC 15 May (Figure 3.3c). This pre-frontal trough eventually evolved into a north-south oriented squall line extending over much of eastern Georgia by 0600 UTC 15 May (Figure 3.3f). NOAA WPC surface analyses also show a deepening low pressure system as it tracked from southern Indiana at 0000 UTC 15 May (Figure 3.3c) north-northeasterly to east-central Indiana by 0600 UTC 15 May (Figure 3.3f). A surface cold front extended from this low pressure system center southward into the Gulf of Mexico (Figure 3.3c,f), but the IPHEx region remained in the warm sector of the storm, ahead of the cold front, until after 1200 UTC 15 May (not shown).

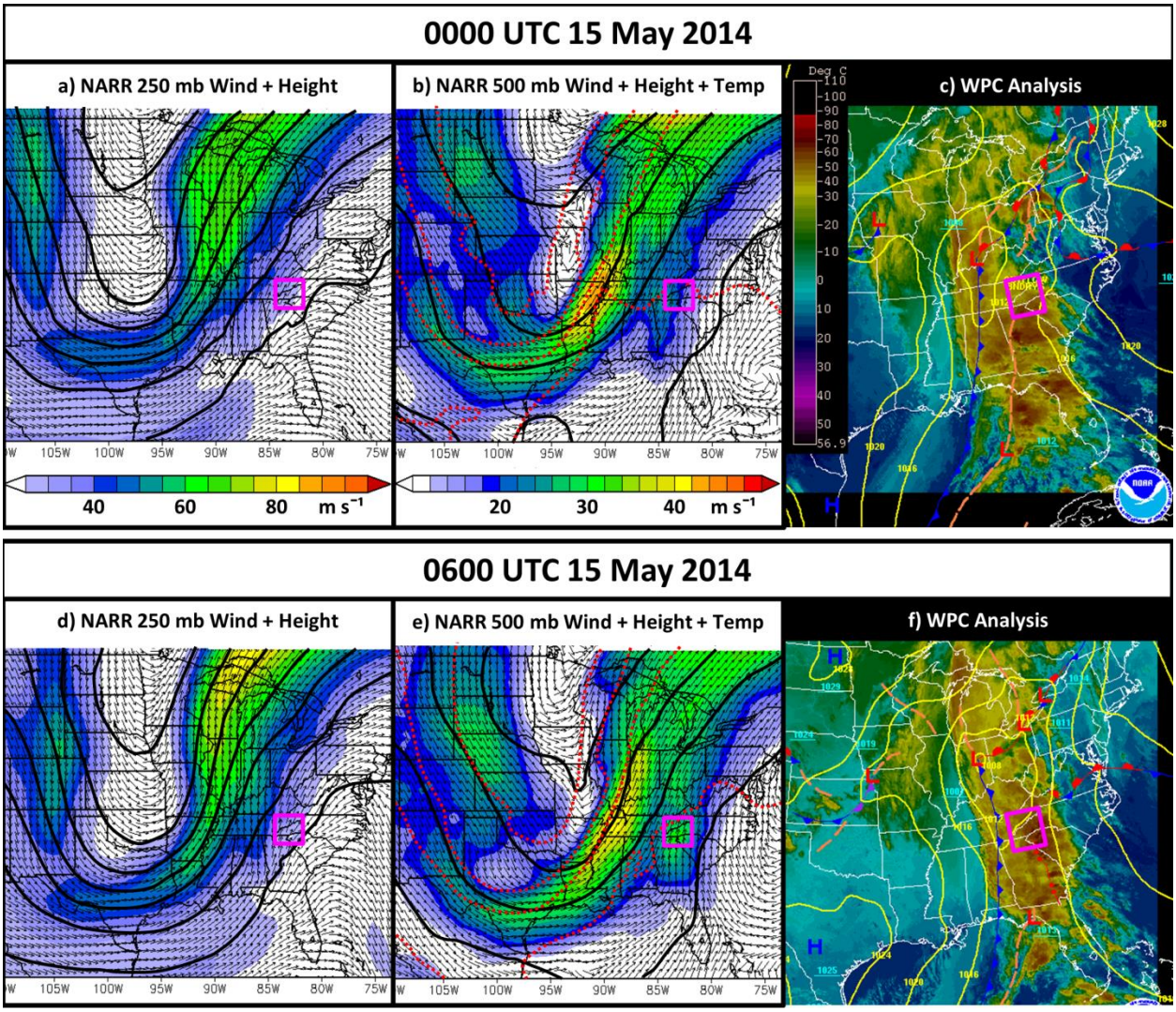

Figure 3.3: National Centers for Environmental Prediction (NCEP) North American Regional Reanalysis (NARR) 250 mb vector wind speeds (color-filled + vectors) and 250 mb geopotential height (black contour lines, 100 m spacing) are shown in a) and d). NARR 500 mb vector wind speeds (color-filled + vectors), 500 mb geopotential height (black contour lines, 100 m spacing), and 500 mb temperatures (red dotted contour lines; 5°C spacing) are shown in b) and e). NOAA Weather Prediction Center (WPC) infrared satellite (color-filled), surface pressure (yellow contour lines), and surface frontal analysis maps are shown in c) and f). Panels a) - c) represent analysis at 0000 UTC 15 May 2014, and panels d) - f) represent analysis at 0600 UTC 15 May 2014. The 250 mb wind speed colorbar is shown in a), the 500 mb wind speed colorbar is shown in b), and the infrared satellite temperature scale is shown in c). The area bounded by the pink boxes roughly outlines the IPHEx region shown in Figure 3.1.

Enhanced southerly and southeasterly flow at low levels favored strong moisture transport, convergence, and convection into the southern part of the

IPHEx region between 0000-0600 UTC 15 May 2014 (Figure 3.4), comparable to atmospheric river (AR; Zhu and Newell 1998) conditions previously observed in the southeastern US (e.g., Moore et al. 2012). Global Forecast System (GFS) analysis of Integrated Water Vapor (IWV) shows a plume of enhanced moisture (IWV > 40 mm) extending into the southeastern US from the tropical Atlantic Ocean during this analysis period (Figure 3.4a,d). Similarly, GFS analysis of Integrated Vapor Transport (IVT) shows a corridor of enhanced moisture transport (IVT > 300 kg m^{-1} s^{-1}) from The Bahamas into the southeastern US (Figure 3.4b,e). The IPHEx region observed an increase in IWV and IVT between 0000 UTC and 0600 UTC 15 May, with IWV (IVT) values 20-40 mm (250-700 km m^{-1} s^{-1}) at 0000 UTC (Figure 3.4a,b) and 35-45 mm (700-1200 kg m^{-1} s^{-1}) at 0600 UTC (Figure 3.4d,e). Additionally, 850 mb wind vectors show converging winds over the region of highest IWV between the eastern Gulf of Mexico and the southern boundary of the IPHEx region (Figure 3.4a,d), which helped increase the low-level moisture. This convergence of warm, moist air allowed instability to build over much of the southeast US as NARR surface-based Convective Available Potential Energy (CAPE) maximized at over 3700 J kg^{-1} along the southwestern boundary of the IPHEx region by 0000 UTC 15 May (Figure 3.4c). NARR surface-based CAPE decreased over the entire southeast US land area by 0600 UTC 15 May (Figure 3.4f), likely due to the lack of shortwave surface heating at this time (0200 AM local time), but values remained as high as 1500 J kg^{-1} in southwestern Georgia where a maxima in IWV existed (IWV > 50 mm; Figure 3.4d). The abundant moisture and instability within the southeast US

allowed organized convection to form within the warm sector of the extratropical system, as evidenced by a large region of cold cloud tops (< -30°C) extending out of the Gulf of Mexico (Figure 3.3c,f), the outflow boundaries (Figure 3.3c) and large north-south squall line (Figure 3.3f) identified by NOAA WPC analyses, and the National Weather Service (NWS) NEXRAD national reflectivity mosaic (supplemental Figure 1). However, convection seems constrained to the region south of the Appalachians.

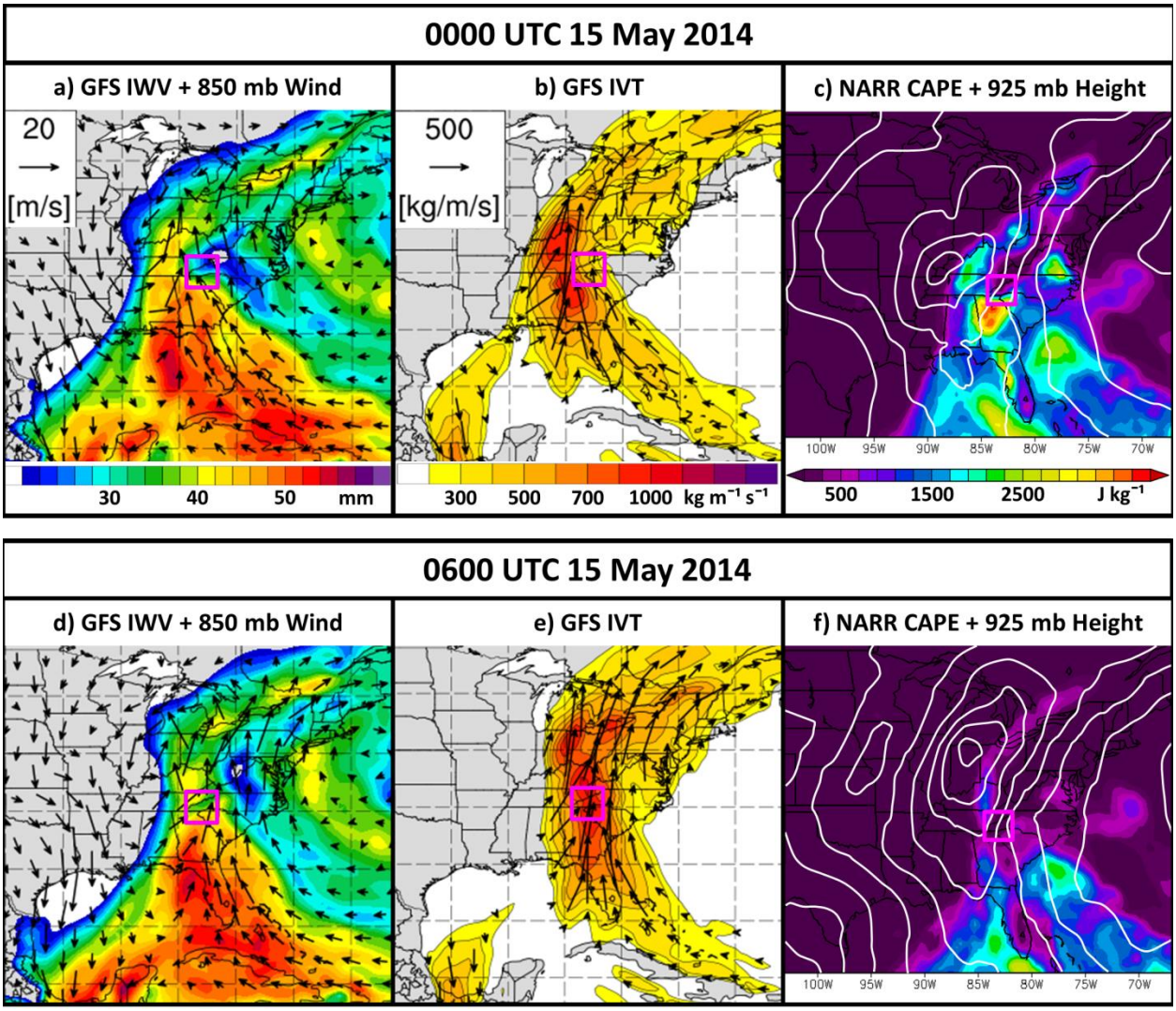

Figure 3.4: Global Forecast System (GFS) model analysis of Integrated Water Vapor (IWV; color-filled) and 850 mb wind speed (black vectors) is shown in a) and d). GFS analysis of

Integrated Vapor Transport (IVT; color filled + vectors) is shown in b) and e). NARR surface-based Convective Available Potential Energy (CAPE; color-filled) and 925 mb geopotential height (white contour lines) are shown in c) and f). Panels a) - c) represent GFS analysis at 0000 UTC 15 May 2014, and panels d) - f) represent analysis at 0600 UTC 15 May 2014. The GFS IWV colorbar and 850 mb reference wind vector are shown in a), the GFS IVT colorbar is shown in b), and the NARR surface-based CAPE colorbar is shown in c). The area bounded by the pink boxes roughly outlines the IPHEx region shown in Figure 3.1.

While the synoptic environment suggests large transport and convergence of moist unstable air into the IPHEx region, regional topography caused contrasting atmospheric environments south and north of the southern Appalachian Mountains, indicating the mountains may have impeded the transport of low-level moisture farther north and thus impacted the precipitation distribution from this AR event. The north-south oriented prefrontal squall line that developed between the Georgia-Florida border and the southern boundary of the IPHEx region by 0600 UTC 15 May impinges on the southern Appalachians of southwest North Carolina, but does not extend north of the mountains (Figure 3.3c). This prefrontal squall line propagated eastward over central South and North Carolina by 1200 UTC 15 May, similarly terminating over the Appalachian mountains of central West Virginia (supplemental Figure 3.1). This indicates the region immediately north of the southern Appalachians was not as conducive to maintaining convection, which agrees with NARR surface-based CAPE as values generally remained below 500 J kg^{-1} within the northern end of the IPHEx region throughout the analysis period (Figure 3.4c,f). Additionally, the plume of strongest IWV (> 45 mm) remained south of the southern Appalachians (Figure 3.4a,d) even though the strongest region of IVT (> 800 kg m^{-1} s^{-1}) extended both south and north of the mountains (Figure

3.4b,e). A pocket of drier air (IWV < 25 mm) was centered over the northeast tip of Tennessee and extended southeast into central and eastern North Carolina at 0000 UTC 15 May (Figure 3.4a), which advected northeastward by 0600 UTC 15 May (Figure 3.4d). Note that the lower IWV values centered over western North Carolina are largely due to the higher terrain of the Appalachians and thus reduced atmospheric depth over which to accumulate moisture, but the terrain is at similar elevations (< 500 m MSL) northwest and southeast of the Appalachians within the IPHEx region (Figure 3.1). Therefore, we would expect to observe similar IWV values north of the Appalachians as we observe south as the AR moisture plume moves eastward. However, this is not what is observed. The pocket of drier air created a strong moisture gradient over the IPHEx region at 0000 UTC (Figure 3.4a), with higher moisture south (IWV up to 46 mm) and less moisture north (IWV up to 34 mm). This moisture gradient decreased but still existed by 0600 UTC 15 May (Figure 3.4d), with IWV up to 46 mm south and up to 42 mm north. NOAA Storm Prediction Center (SPC) mesoscale analysis maps of surface dewpoint temperature also show this moisture gradient between 0000-0600 UTC 15 May (not shown). This all indicates that low-level moisture was physically blocked by the Appalachian Mountains, squeezed out by heavy precipitation associated with the squall line and orographic lift, or a combination of the two.

To further analyze the impact that the southern Appalachian Mountains had on the precipitation during this AR event, in the following section we will analyze a small squall line that propagated through the IPHEx region from southwest to

northeast between 0000 UTC and 0430 UTC 15 May (Figure 3.5), along the eastern edge of the IWV plume (Figure 3.4a) and ahead of the large WPC-analyzed north-south squall line that impacted the IPHEx region later (Figure 3.3f).

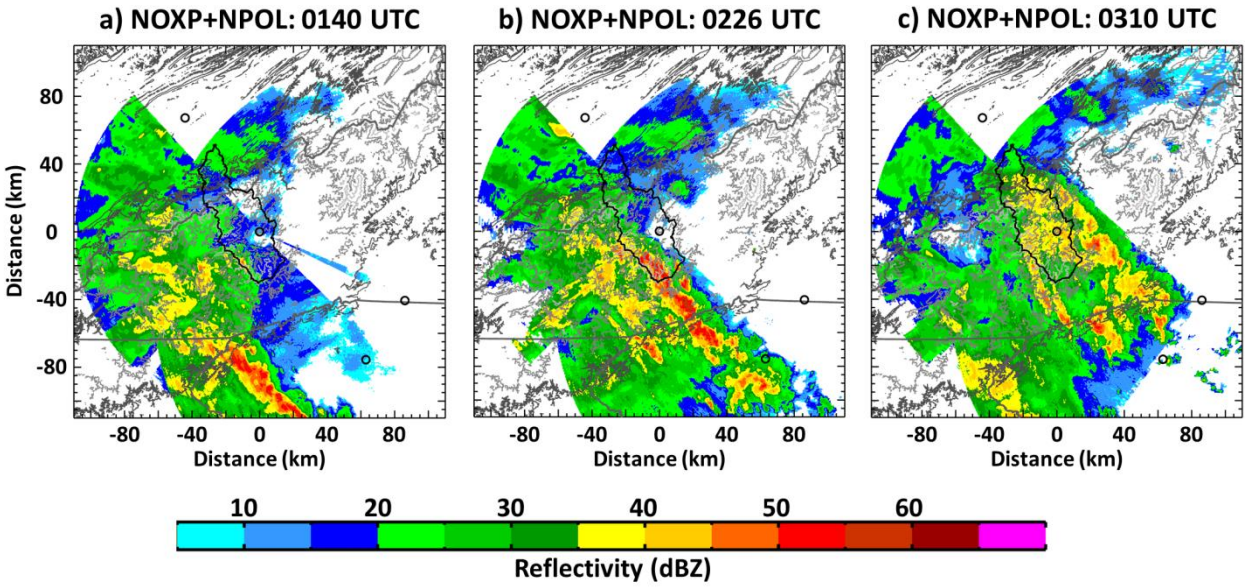

Figure 3.5: Merged NOXP and NPOL radar volume column max reflectivity is shown for volumes ending at a) 0140 UTC, b) 0226 UTC, and c) 0310 UTC on 15 May 2014 as a squall line moved up and over the southern Appalachians of southwestern North Carolina. The reflectivity colorbar is shown at bottom. The Pigeon River Basin watershed is outlined in black for reference, see Figure 3.1.

3.5 Squall Line Evolution: Radar Observations

In this section we investigate through the view of the NOXP and NPOL research radars how a prefrontal squall line evolved as it encountered the mountainous terrain of the southern Appalachians within the IPHEx region. The squall line propagated from southwest to northeast over the IPHEx region (Figure 3.5), so the radar analysis will focus on the squall line evolution from southwest to northeast. To identify the orographic impacts of the mountainous terrain on squall

line evolution, we will compare the squall line organization over the mountainous region to that over the flatter region to the southeast of the Pigeon River Basin (Figure 3.1). Additionally, we are interested in the differences in squall line organization and intensity upwind and downwind of the higher mountain ridges along the southwestern and southern boundary of the Pigeon River Basin, so we designated upwind to be southwest of the NOXP radar location and downwind to be northeast of the NOXP radar location. This creates four 40x60 km^2 analysis domains that we will denote as upwind terrain (UT), downwind terrain (DT), upwind plains (UP), and downwind plains (DP; Figure 3.1).

3.5.1 Upwind vs. Downwind Terrain

The squall line leading-line convection propagated over the mountain and valley terrain of the UT and DT domains between 0140-0400 UTC where it maximized in intensity over the higher terrain of the UT domain and weakened over the lower terrain of the DT domain (Figure 3.6). The leading-line convection also slowed down within the valley of the DT domain, propagating from southwest to northeast at a speed of 16.3 m s^{-1} through the UT domain and 14.1 m s^{-1} through the DT domain. The leading-line convection reached a maximum in intensity (reflectivity 55-60 dBZ) over and immediately downwind of the highest mean terrain between -30 km and -3 km (Figure 3.6). The leading-line convection then maintained a lower intensity (reflectivity 50-55 dBZ) as it entered the DT domain before weakening significantly beyond 30 km from the NOXP location. The expected trailing stratiform region immediately following the leading-line convection actually

contained embedded convection (identified by numbers 6, 7, and 8 in Figure 3.6a), but this trailing convection did not make it beyond 15 km into the DT domain. More information on convective cells 1-5 will be discussed in section 4c.

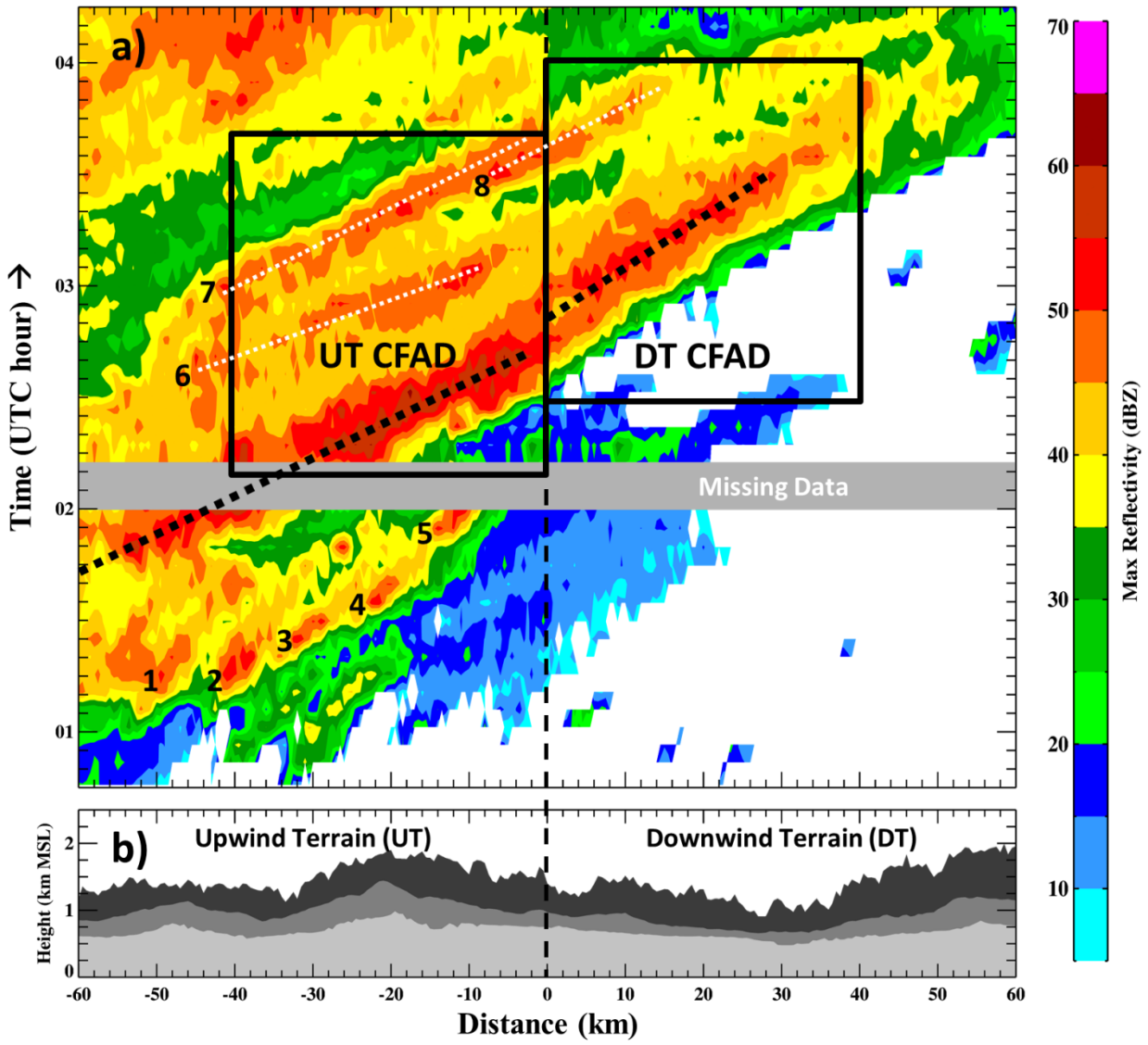

Figure 3.6: a) Hovmöller diagram of maximum reflectivity between 0045 - 0415 UTC 15 May 2014 showing the progression of a squall line over the UT and DT domains. Distances along the x-axis denote distance southwest (negative) and northeast (positive) of the NOXP radar location. Time increases upward on the y-axis. Maximum reflectivity is computed between heights of 1 km to 3 km above mean sea level (MSL) and between -10 km and 30 km from the NOXP radar along the southeast (negative) to northwest (positive) y-dimension of the Cartesian grid rotated -45° from true north. The reflectivity mosaic data used consists of merged rotated grids with both NOXP and NPOL radar data (see section 3.3). The position of the squall line leading-line convection is denoted with the thick dotted

black line. The UT and DT contoured frequency by altitude diagram (CFAD) domain boundaries used to compute data for Figure 3.7 are shown with black boxes. b) Minimum (light gray), mean (medium gray), and maximum (dark gray) terrain elevation profiles are shown for the UT and DT domains. See text for more details.

To document the overall change in vertical structure of the squall line, we constructed UT and DT contoured frequency by altitude diagrams (CFADs) of reflectivity over smaller upwind/downwind distances and shorter times that encompassed only the squall line leading-line convection and trailing stratiform region (Figure 3.6a) and subtracted the DT CFAD from the UT CFAD to get a difference CFAD (Figure 3.7). This difference CFAD shows that higher mean and median reflectivity (0-4 dB) was observed at low levels (below 4 km MSL) within the melting and rain layers of the UT CFAD domain (Figure 3.7), indicating larger hydrometeors and heavier rain fell out over the UT CFAD domain. However, mean and median reflectivity profiles were similar at upper levels (4-7 km MSL; Figure 3.7), indicating precipitation growth from upper-level clouds was similar over the UT and DT CFAD domains. Limited radar observations are available above 7 km MSL due to the NOXP and NPOL radar scan strategies, so CFAD differences are less reliable above this level.

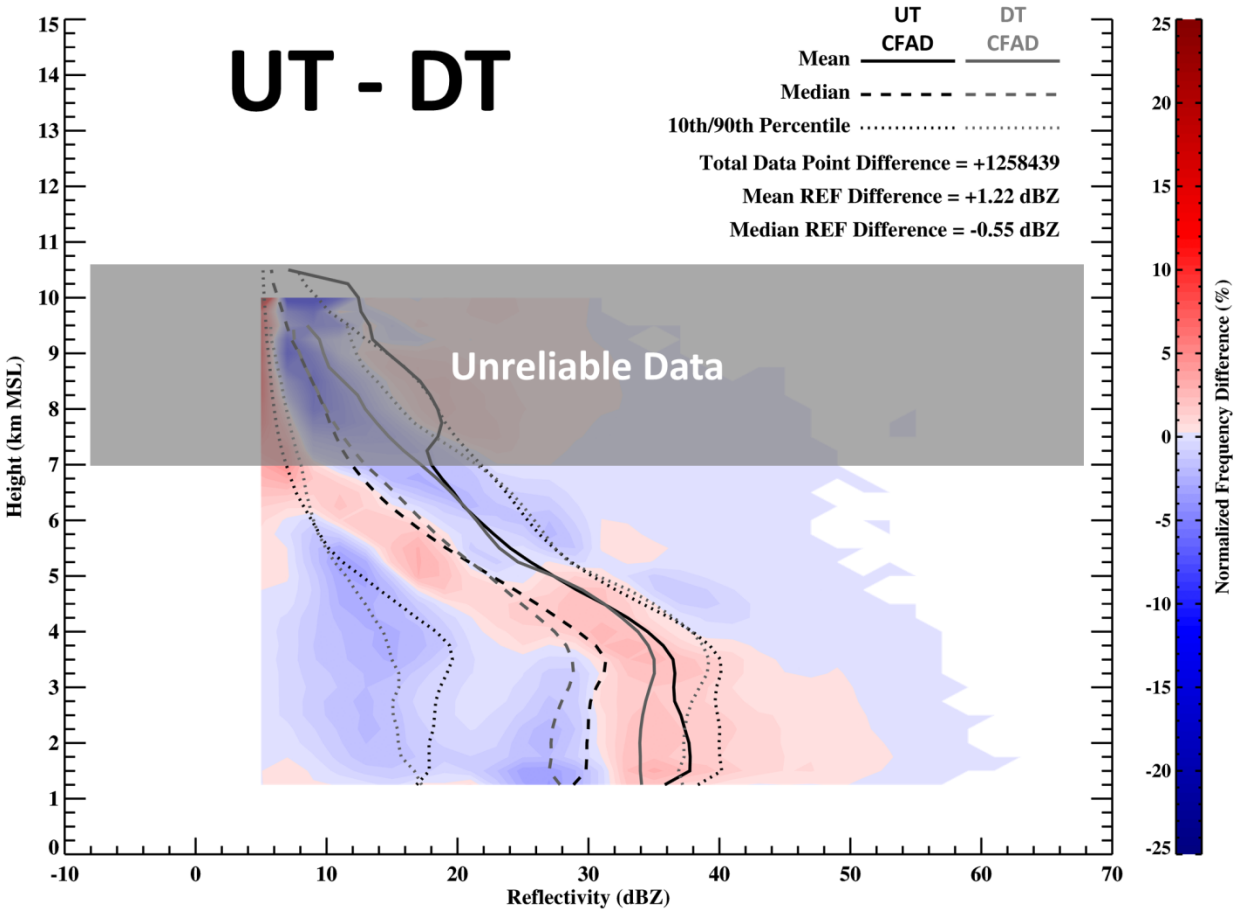

Figure 3.7: Difference CFAD showing the difference in normalized frequency of reflectivity observations between the UT CFAD domain and the DT CFAD domain. Frequency is normalized by the total number of observations in each height bin (every 250 m). Red colors indicate more reflectivity values were observed in the UT CFAD domain compared to the DT CFAD domain, whereas blue colors indicate the opposite. The mean (solid lines), median (dashed lines), and 10th and 90th percentile (dotted lines) reflectivity profiles for the UT CFAD (black) and DT CFAD (gray) are overlaid for comparison. The UT CFAD domain is shown in Figure 3.6 and includes gridded NOXP and NPOL reflectivity data between 0210 - 0340 UTC within a rotated grid domain of -40 km to 0 km in the x-dimension and -30 km to 10 km in the y-dimension. The DT CFAD is shown in Figure 3.6 and includes gridded NOXP and NPOL reflectivity data between 0230-0400 UTC within a rotated grid domain of 0 km to 40 km in the x-dimension and -30 km to 10 km in the y-dimension. The grid is rotated -45 degrees from north so that the x-axis is aligned in the southwest/northeast direction and y-axis is aligned in the northwest/southeast direction.

To better understand the temporal evolution of the vertical structure of the squall line as it passed over the highest terrain, we calculated maximum reflectivity cross-sections over a 10 km wide region at the center of the UT and DT domains

between 0217-0250 UTC (Figure 3.8a-h). At 0217 UTC the leading-line convection had reached its maximum intensity (reflectivity 55-60 dbZ) along the southwestern (windward) slope of the main mountain ridge between -30 km and -20 km southwest of the NOXP radar, with the trailing stratiform region (reflectivity up to 45 dBZ) extending beyond -30 km (Figure 3.8a,e). At 0226 UTC, the leading-line convection had crested the main ridge with little loss in intensity (reflectivity up to 55 dBZ) and was positioned on the northeastern (lee) slope between -22 km and -12 km, with the trailing stratiform region extending beyond -22 km (Figure 3.8b,f). Note that a region of stratiform precipitation with a visible melting layer at 3.5 km MSL extended ~ 5 km ahead of the leading-line convection at 0226 UTC (Figure 3.8b,f), indicating potential advection of mid- and upper-level hydrometeors by strong southerly winds aloft (section 3). At 0236 UTC the leading-line convection had weakened slightly (reflectivity 50-55 dBZ) and narrowed as it moved over the central valley within the Pigeon River Basin between -3 km and -12 km (Figure 3.8c,g). A well-developed, broad trailing stratiform region extended from -45 km to -12 km behind the leading-line convection at 0236 UTC, with reflectivity reaching 45-50 dBZ in the melting layer around 3.5 km MSL (Figure 3.8g). By 0250 UTC the leading-line convection had moved into the DT domain (0 km to 8 km) and weakened (reflectivity 45-50 dBZ; Figure 3.8d,h). Additionally, the trailing stratiform region weakened overall by 0250 UTC, but a convective cell appeared embedded within the trailing stratiform region on the southwestern slope of the main ridge between -28 km and -32 km (Figure 3.8d,h). This cross-section time

series shows that the squall line leading-line convection weakened and became more narrow as it moved from upwind to downwind of the high mountain ridge line ~ 20 km southwest of the NOXP radar location along the southwestern boundary of the Pigeon River Basin. Additionally, the trailing stratiform region became embedded with convective cells by 0250 UTC.

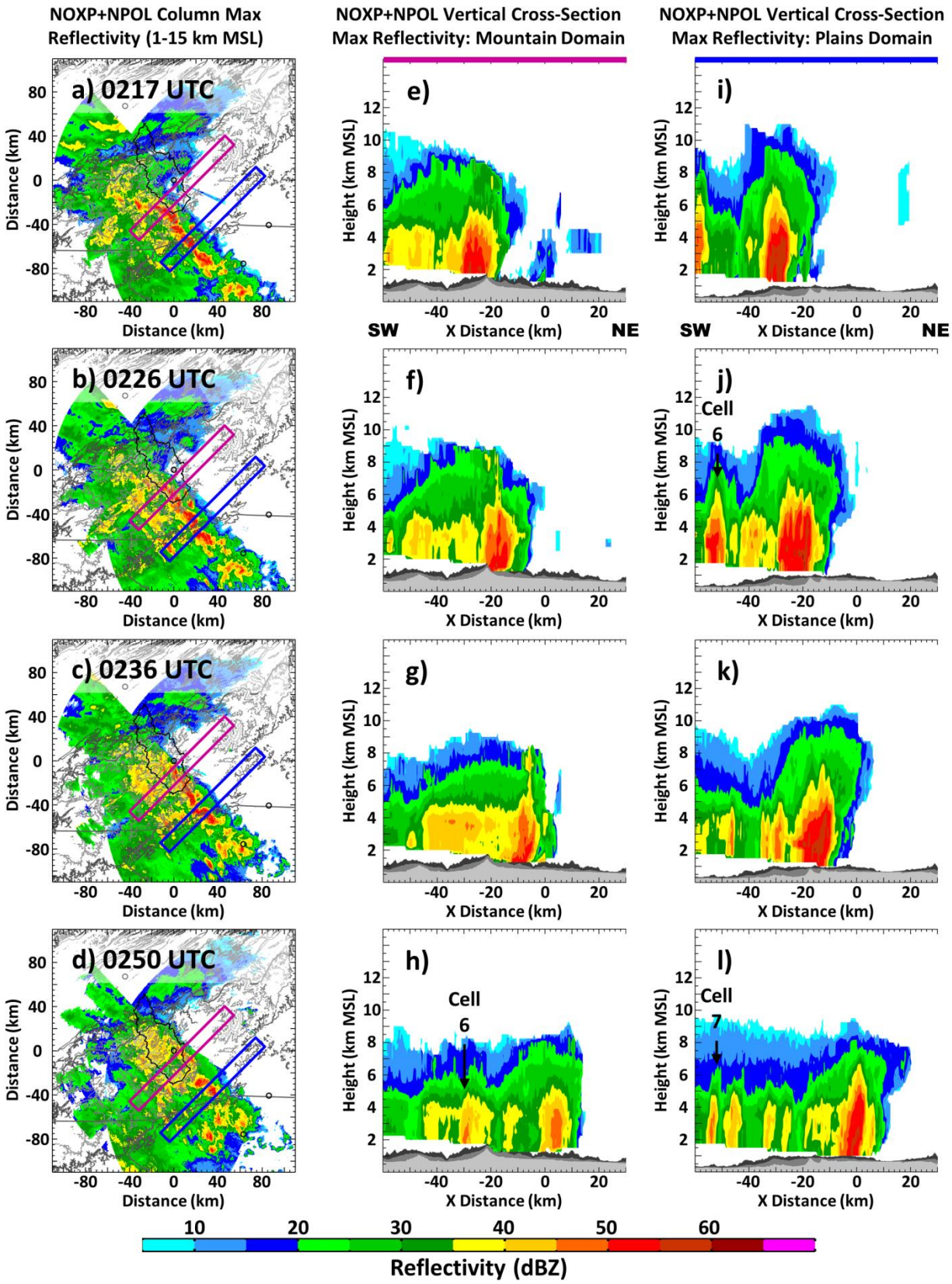
NOXP+NPOL Column Max Reflectivity (1-15 km MSL)
NOXP+NPOL Vertical Cross-Section Max Reflectivity: Mountain Domain
NOXP+NPOL Vertical Cross-Section Max Reflectivity: Plains Domain
a) 0217 UTC
b) 0226 UTC
c) 0236 UTC
d) 0250 UTC
e)
f)
g)
h)
i)
j)
k)
l)
Cell 6
Cell 6
Cell 7
SW
NE
Distance (km)
Height (km MSL)
X Distance (km)
10 20 30 40 50 60
Reflectivity (dBZ)

Figure 3.8: A time series of maximum reflectivity from the NOXP and NPOL merged radar volumes showing the passage of the squall line between 0217 UTC and 0250 UTC 15 May 2014. The left column shows maximum reflectivity in the vertical column between 1-15 km MSL at a) 0217 UTC, b) 0226 UTC, c) 0236 UTC, and d) 0250 UTC. USGS terrain elevation contours are overlaid in a) - d) every 500 m, with darker gray colors for lower elevations and lighter gray for higher elevations. The Pigeon River Basin is outlined in black for reference, see Figure 3.1. The center column e) - h) shows vertical cross-sections of maximum reflectivity within the center of the UT and DT domains, defined as y-axis grid distances between -15 km and -5 km from the NOXP radar for the grid volumes rotated -45° from true north, which is shown in a) - d) as the purple box. The right column i) - l) shows vertical cross-sections of maximum reflectivity within the center of the UP and DP domains, defined as y-axis grid distances between -55 km and -45 km from the NOXP radar for the rotated grid volumes, shown in a) - d) as a blue box. Minimum (light gray), mean (medium gray), and maximum (dark gray) terrain elevation profiles are overlaid in e) - l). See text for further details.

Overall, these radar observations elucidate that the squall line weakened and slowed from the UT to DT domain, with weakening even occurring downwind of the main ridge line at -20 km within the UT domain. Additionally, embedded convective cells formed within the trailing stratiform region upwind of the main mountain ridge within the UT domain, but dissipated before or shortly after entering the DT domain. To further determine the importance of the mountains on this dichotomy, we next compare these findings with the UP and DP domains.

3.5.2 Upwind vs. Downwind Plains

The squall line leading-line convection propagated through the flatter UP and DP domains between 0130-0400 UTC at a consistent speed of 13.7 m s^{-1} (Figure 3.9), but the squall line weakened and became disorganized from the UP to DP domain (Figures 3.5, 3.9a). The leading line convection reached a maximum in intensity with reflectivity 60-65 dBZ around 0230 UTC and -20 km within the UP domain (Figure 3.9a). This maximum in intensity is slightly larger than over the UT domain but occurs at a similar upwind distance. The leading-line convection

then weakened after entering the DP domain, with most of the linear structure of the squall line disappearing beyond 15 km downwind of the NOXP location and transitioning to more scattered convection (Figures 3.5c, 3.9a). Convective cells with intensity comparable to the leading-line convection (reflectivity 55-60 dBZ) were present within the trailing stratiform region of the UP domain, but not in the DP domain (cells 6-8; Figure 3.9a). Although these trailing convective cells were also present in the UT domain (Figure 3.6a), the cells within the UP domain were more intense (higher reflectivity).

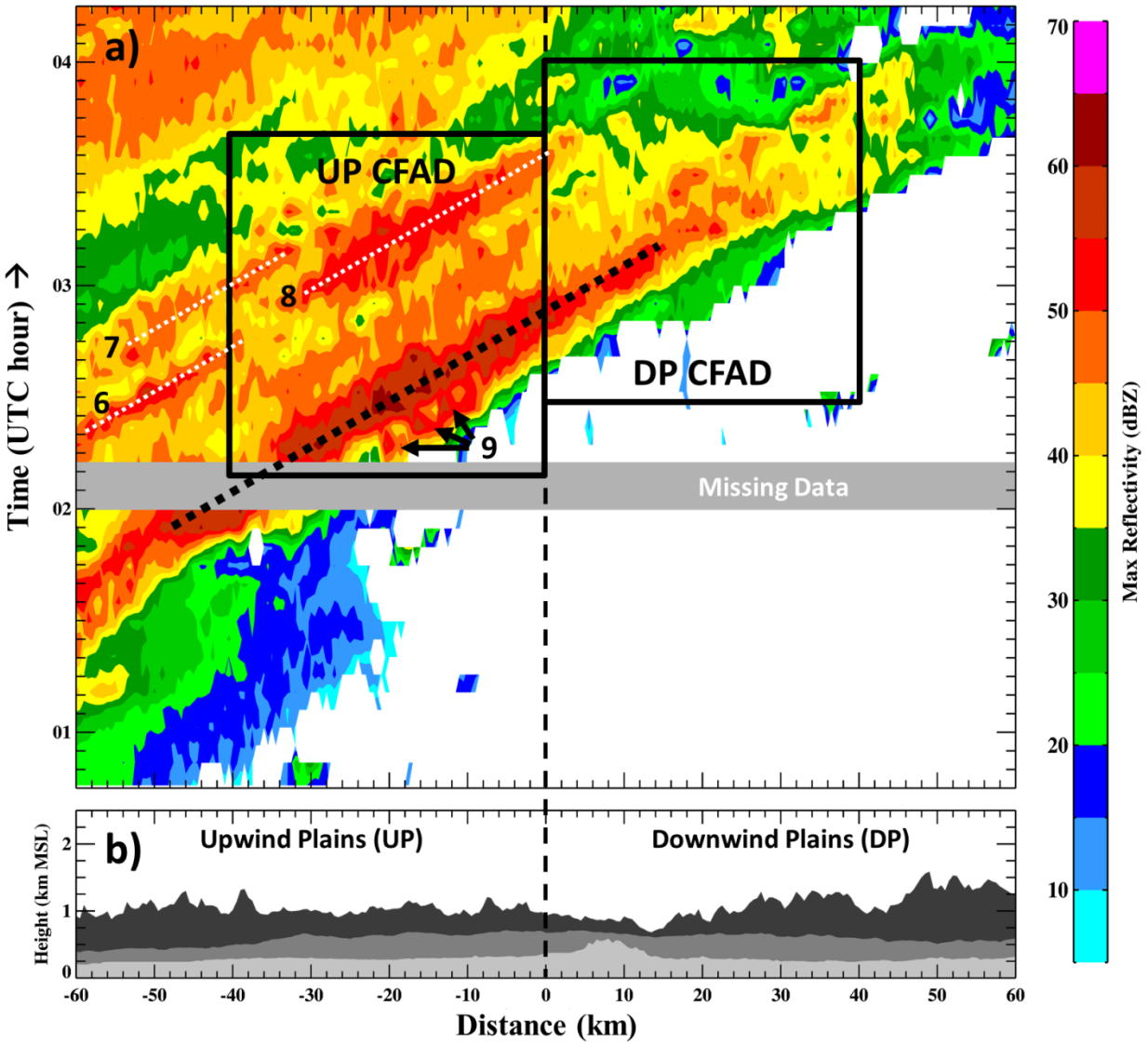

Figure 3.9: As in Figure 3.6, except for the UP and DP domains. The UP and DP CFAD domain boundaries used to compute data for Figure 3.10 are shown with black boxes. See Figure 3.6 and text for further details.

The vertical reflectivity profiles within the UP and DP CFAD domains, which only encompass the squall line (Figure 3.9a), show a consistent decrease in both mean (2-6 dB) and median reflectivity (1-3 dB) from UP to DP at all levels between 1-7 km MSL (Figure 3.10), indicating a weakening squall line. This decrease in squall line intensity is greater than that compared to going from the UT to DT CFAD domain (Figure 3.7), especially at upper levels (4-7 km MSL), indicating both

upper-level precipitation growth and convection weakened between the UP and DP domain.

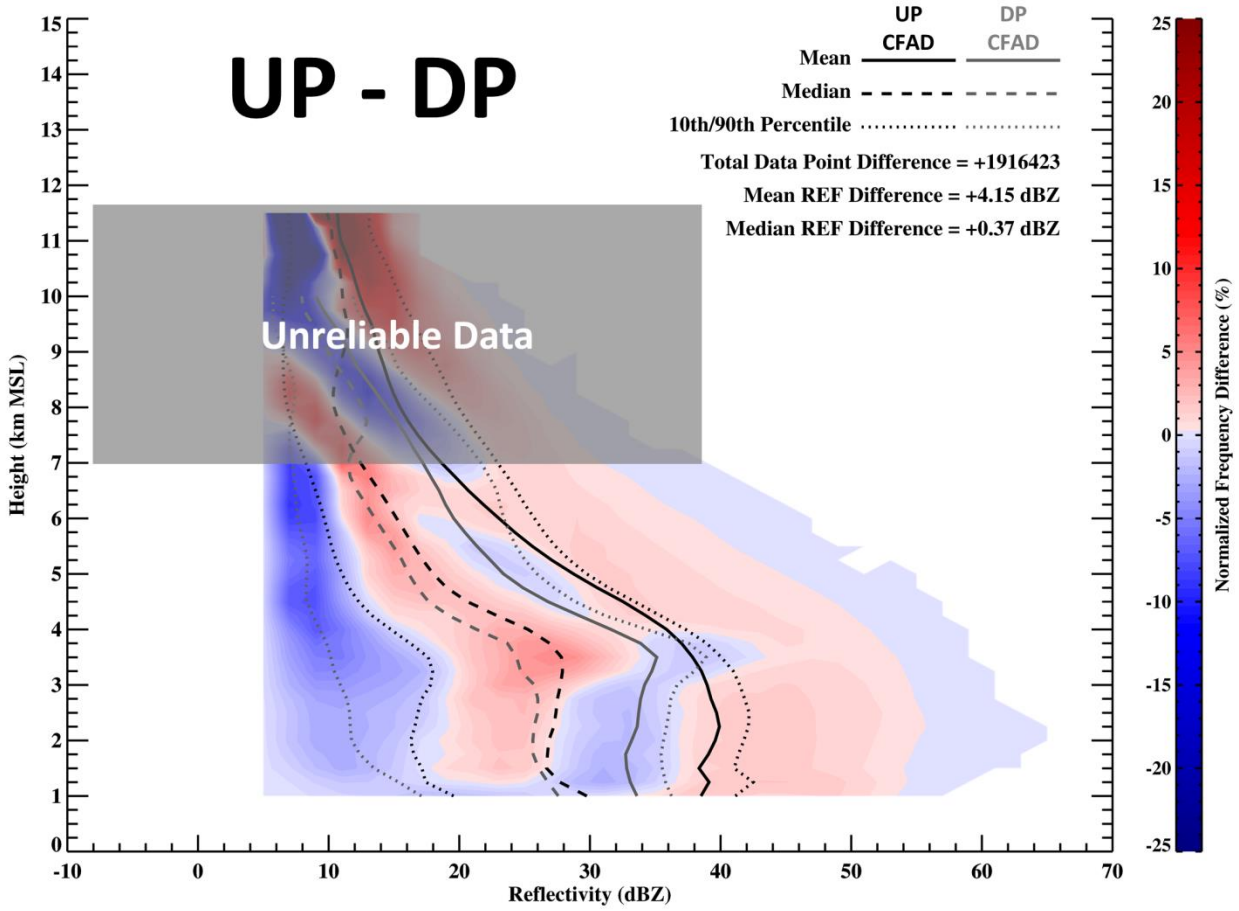

Figure 3.10: As in Figure 3.7, except CFAD differences between the UP and DP CFADs. The UP CFAD domain is shown in Figure 3.9 and includes gridded NOXP and NPOL reflectivity data between 0210 - 0340 UTC within a rotated grid domain of -40 km to 0 km in the x-dimension and -70 km to -30 km in the y-dimension. The DP CFAD is shown in Figure 3.9 and includes gridded NOXP and NPOL reflectivity data between 0230 - 0400 UTC within a rotated grid domain of 0 km to 40 km in the x-dimension and -70 km to -30 km in the y-dimension. See Figure 3.7 for more details.

The temporal evolution of the vertical structure of the squall line over the center of the UP and DP domains between 0217-0250 UTC (Figure 3.8i-l) shows that the leading-line convection was more intense compared to the UT/DT cross-section during this time (Figure 3.8e-h), but the trailing stratiform precipitation

was less extensive with more scattered convection present in the UP/DP cross-section. Reflectivity exceeded 55 dBZ within the leading-line convection at all times between 0217-0250 UTC in the UP/DP cross-section (Figure 3.8i-l), whereas maximum reflectivity dropped from 50-55 dBZ at 0217 UTC to 45-50 dBZ within the leading-line convection over the UT/DT cross-section (Figure 3.8e-h).

Overall, these observations show that the squall line leading-line convection was weakening from southwest to northeast regardless of the presence of the mountains in the UT domain. However, the leading-line convection was able to maintain its strength longer in the UP domain compared to the UT domain, indicating the significant mountain ridge centered at ~ -20 km upwind of the NOXP radar within the UT domain may be responsible for weakening the squall line leading-line convection as it propagated into the lee (between -20 km and 0 km) prior to entering the DT domain. Additionally, the trailing stratiform region was weaker and less continuous over the UP domain compared to the UT domain, but more numerous and intense convective cells were observed over the UP domain. We next identify additional differences between the mountainous terrain domains (UT and DT) and the flatter plains domains (UP and DP) that indicate the mountains modified precipitation during this period.

3.5.3 Terrain vs. Plains: Upwind Comparisons

Although the leading-line convection was more intense over the UP domain compared to the UT domain, the UT domain was overall more efficient in hydrometeor growth. Differences in the UT and UP CFAD reflectivity vertical

profiles show mean reflectivity 1-3 dB lower at all levels between 1-7 km MSL and median reflectivity 1-3 dB higher at all levels between 1-6 km MSL within the UT CFAD domain compared to the UP CFAD domain (Figure 3.11a). Because mean reflectivity values are heavily influenced by the largest hydrometeors, including large raindrops and hail commonly found during convection, the convective precipitation was stronger in the UP CFAD domain compared to the UT CFAD domain. This agrees with the maximum reflectivity time-series (Figures 3.5, 3.8) and Hovmöller analyses (Figures 3.6, 3.9) previously analyzed. The median reflectivity profile is a better estimate of the overall intensity of precipitation throughout the CFAD time period, which indicates that precipitation particles were consistently larger over the UT CFAD domain, at least below 6 km MSL. Overall, this indicates that a more efficient precipitation growth mechanism existed over the mountains of the UT domain compared to the flatter UP domain even though the squall line convection was more vigorous over the plains. A closer look outside the squall line leading-line convection indicates potential sources for this efficient precipitation growth mechanism.

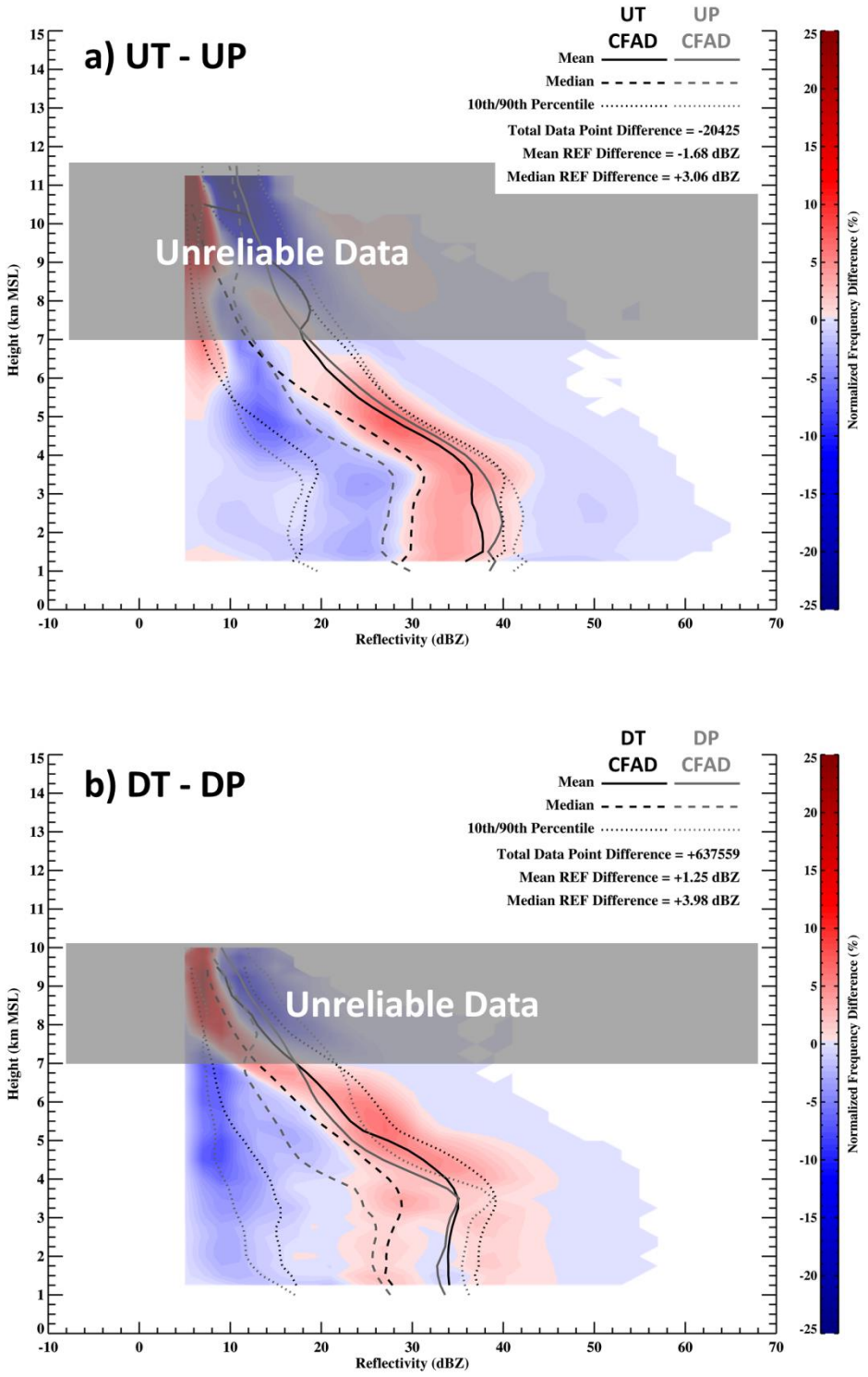

Figure 3.11: As in Figures 3.7 and 3.10, except for a) UT vs. UP CFADs and b) DT vs. DP CFADs. See Figures 3.7 and 3.10 and text for further details.

Convective cells outside the squall line leading-line convection seem to differ in number and strength between the UT and UP domains (denoted by numbers 1-8 in Figures 3.6a, 3.8, 3.9a), with small convective cells (cells 1-5) preferentially initiating over the UT domain prior to the leading-line convection (Figure 3.6a) and more vigorous (larger reflectivity) convective cells (cells 6 and 8) in the UP domain following the leading-line convection (Figures 3.6a, 3.8h,j, 3.9a). Additionally, only one of these cells was able to propagate into the DT domain before quickly weakening (cell 8; Fig 6a). These convective cells were short-lived (10-45 minutes) and do not appear to be part of the squall line leading-line convection as cells 1-5 never merged with the linear leading-line convection region and cells 6-8 were embedded in the trailing stratiform region. The independent convective cells 1-5 prior to the squall line leading-line convection were likely triggered by the underlying mountains through upslope flow or mountain-induced wave motions because they were absent in all other domains (Figures 3.6a, 3.9a) and appear to initiate near the 1000 m elevation contour along the southeastern boundary of the UT domain (supplemental Figure 2). Discrete propagation by gravity waves induced by the squall line itself (Fovell et al. 2006) likely played a role for convective cell 9 immediately ahead (within 5 km) of the squall line leading-line convection in the UP domain (Figures 3.8a-c, 3.9a). This cell merged into the leading-line convection, whereas cells 1-5 did not. Regardless, the mountainous UT domain experienced convection for a longer period of time compared to the UP domain because of the presence of cells 1-5, indicating the mountainous environment within the UT

domain was more efficient at releasing convective instability. In contrast, cells 6 and 8 were able to reach higher intensity (max reflectivity 55-60 dBZ; Figure 3.9a) in the UP domain compared to the UT domain (max reflectivity 50-55 dBZ; Figure 3.6a), likely due to increased moisture and instability farther south (section 3). However, careful tracking of these stratiform-embedded cells reveals that these cells are advecting northward (Figure 3.5, 3.8a-d; supplemental Figure 2), which is how cells 6-8 show up in both the UP and UT domains (Figures 3.6a, 3.9a). This means that convection within the UP domain will eventually advect into the UT or DT domains. Although cells 6 and 8 were not be able to maintain their strength over the UT domain, advection of hydrometeors aloft and orographic lift likely contributed to the more expansive and consistent trailing stratiform region observed over the UT domain (Figure 3.8a-h).

3.5.4 Terrain vs. Plains: Downwind Comparisons

The DT and DP domains both experienced a weakening and disorganizing squall line, but advection of hydrometeors aloft and convective cells parallel to the squall line allowed heavier precipitation to fall over the DT domain. The squall line leading-line convection was able to maintain its structure and intensity (reflectivity 50+ dBZ) longer in the DT domain (out to 30 km downwind; Figure 3.6a) compared to the DP domain (out to 15 km downwind; Figure 3.9a). Therefore, the mountains within the UT domain did not prevent the squall line leading-line convection from propagating downwind of the highest terrain. Comparing the vertical structures of the DT and DP CFAD domains shows that mean and median reflectivity is

generally larger (0-7 dB) within the DT CFAD domain at all levels between 1-7 km MSL (Figure 3.11b), with more significant differences above 4 km MSL. This indicates that the DT domain experienced larger hydrometeors and heavier rainfall compared to the DP domain. Because individual convective cells advected northward (Figure 3.8a-d; supplemental Figure 2), this caused convective cells to be advected out of the UP and DP domains and into the DT domain. This combined with the northeasterly propagating direction of the weakening squall line caused individual convective cells to track parallel to the squall line southeast/northwest orientation. Additionally, precipitation particles aloft were advected from south to north with the strong southerly upper-level winds (Figure 3.3b,e). Therefore, the DT and DP domains were largely influenced by convection that formed to their south. Because the UP domain contained stronger convection, this allowed heavier rainfall to advect into the DT domain compared to the DP domain. In fact, convective cell 8 advected from the UP domain into the DT domain (Figures 3.6a, 3.9a), skipping the DP domain almost entirely. The full radar time series (supplemental Figure 2) also shows that the southeasterly extend of the squall line moved north into the DP domain, became disorganized, and eventually all convection advected out of the DP domain and into the DT domain after 0400 UTC, thus cutting off precipitation within the DP domain due to the lack of continued convective initiation or orographic lift.

We next investigate how this radar-based squall line evolution relates to precipitation characteristics observed at the surface by rain gauges and disdrometers.

3.6 Squall Line Evolution: Surface Precipitation Characteristics

Rain gauges were grouped into seven southwest/northeast transects with similar distances southeast/northwest from the NOXP radar, with the Pigeon South gauges farthest to the southeast and the Great Smoky Mountains National Park (GSMNP) North gauges farthest to the northwest (Figure 3.12c). This allows comparison of the squall line precipitation as a function of distance southwest/northeast (perpendicular to the squall line orientation) and southeast/northwest (parallel to the squall line orientation). Rain gauge accumulation was summed over the time period starting when the squall line leading-line convection impacted the gauge and ending at the end of the trailing stratiform region for each gauge individually, using the radar mosaic to help identify these times. Most gauges observed detectable rainfall over a period of 50-80 minutes during the squall line passage, with less time for gauges farther northeast, which accounted for 10-25% of the total rainfall observed throughout the full prefrontal period from 0000-1200 UTC 15 May (not shown).

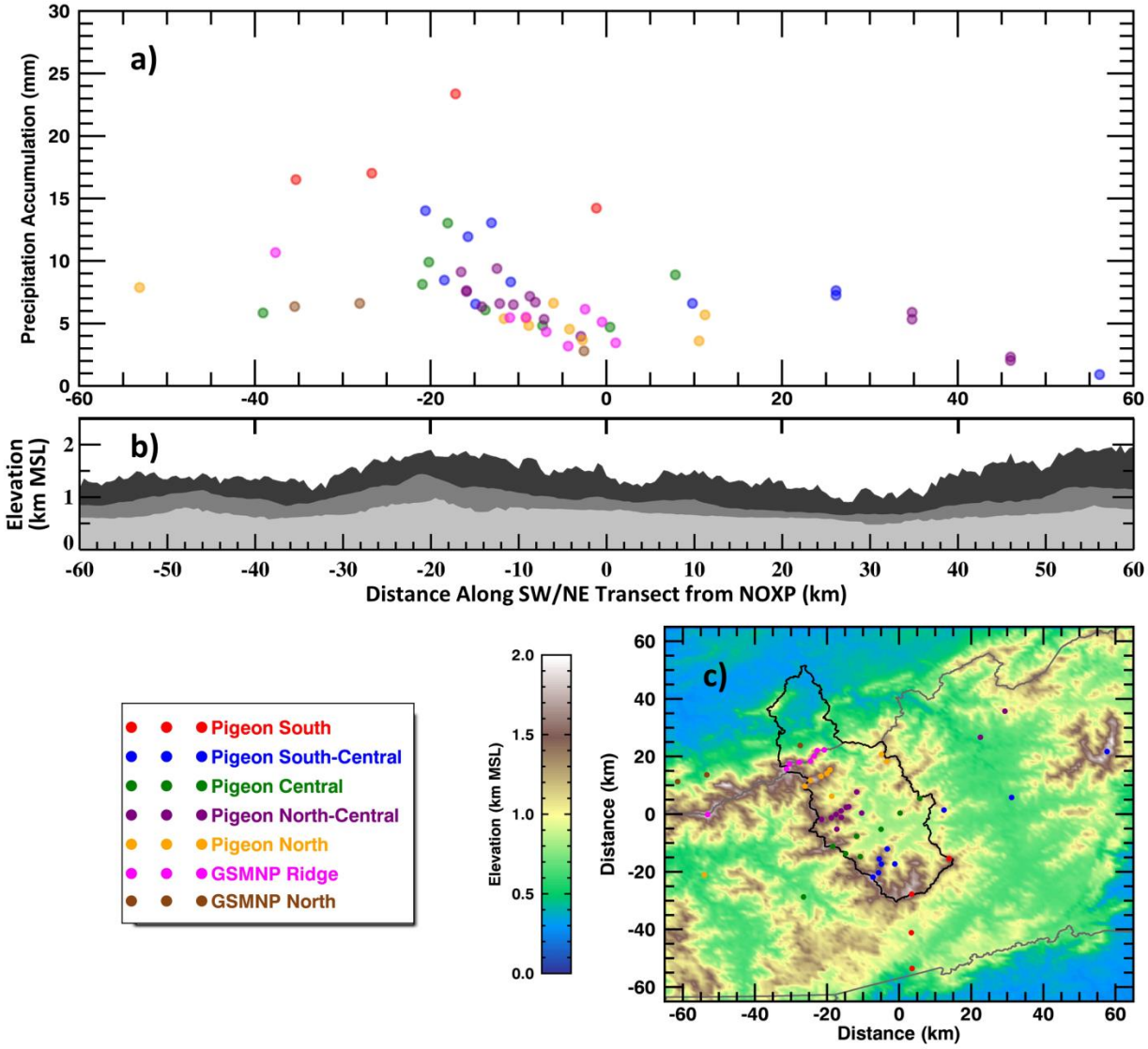

Figure 3.12: Rain gauge total rain accumulation (mm) is plotted in a) as a function of distance from the NOXP radar (km) along a southwest/northeast transect. Terrain minimum, mean, and maximum elevation profiles are shown in b) for the UT and DT domains, same as Figure 3.6b. Gauges are grouped into zones (color-coded) along similar distances from the NOXP radar along a southeast/northwest transect, perpendicular to the southwest/northeast transect and parallel to the squall line leading-line convection orientation. These color-coded gauge locations are plotted on a terrain elevation map in c). See Figure 3.1 and text for more details.

Rain gauge total accumulation during the squall line passage shows an overall decrease from southwest to northeast with a maximum (8-23 mm) located near the main mountain ridge at -20 km (Figure 3.12). This agrees with our radar

analysis (section 4) that indicated the squall line weakened over all domains from southwest to northeast with a maximum intensity near -20 km along the southwest/northeast transect (Figures 3.6a, 3.9a). Upwind of the main ridge line (-60 to -20 km), rain accumulation was similar within the valleys southeast and northwest of the Great Smokey Mountains (GSM) with 6-8 mm accumulating in the Pigeon Central, Pigeon North, and GSMNP North zones (Figure 3.12). Increased rain accumulation was observed at the GSMNP Ridge (11 mm) and Pigeon South (16-17 mm) gauges between -40 km and -25 km, likely due to some orographic enhancement at the GSMNP Ridge gauge and intense convection observed at the Pigeon South gauges (Figure 3.8a-d). Accumulation generally decreases linearly over the lee slope of the main ridge from the southwestern boundary of the Pigeon River Basin near -20 km (8-14 mm) to the central valley within the center of the Pigeon River Basin near 0 km (3-6 mm; Figure 3.12), which agrees with the weakening of the squall line leading-line convection identified by radar over the UT domain (section 4). Although the two Pigeon South gauges follow this decrease from -20 km to 0 km, rain accumulation at these gauges (23 and 14 mm) was well above all other gauges at similar southwest/northeast transect distances by 8-9 mm. This is likely due to their placement along the southern boundary of the Pigeon River Basin, which aligns with a southwest/northeast oriented mountain ridge (the maximum elevation contour shown in Figure 3.12b) that was the first major barrier that the intense squall line and trailing embedded convective cells impacted (Figure 3.8a-d). Additionally, the southeasterly low-level flow (Figure 3.4a) was likely

orographically lifted up this perpendicular ridge, allowing increased condensation and precipitation growth within the trailing stratiform region of the squall line. Rain accumulation increased slightly between 0 km and 40 km, with values 4-9 mm along the northeastern boundary of the Pigeon River Basin and within the valley northeast (20-40 km), but very little rain accumulation (< 3 mm) was generated by the squall line remnants beyond 40 km (Figure 3.12).

Comparison of rain gauge accumulations from southeast to northwest, parallel to the squall line orientation, shows a decrease in rainfall associated with the squall line (Figure 3.12), indicating the squall line was weaker along its northwestern section where it interacted with mountainous terrain. This agrees with our previous findings from the radar analysis (section 4), which shows the squall line leading-line convection was less intense farther northwest (Figure 3.8a-d). However, the more efficient hydrometeor growth identified over the UT domain (section 4) was not able to generate as much precipitation farther northwest, indicating the presence of convection played a larger role in generating precipitation at the surface during this short squall line passage.

In order to understand the changes in the dominant microphysical processes that impacted the surface rainfall characteristics during the squall line passage, the rain drop size distribution (DSD) measured by six PARSIVEL disdrometers will be analyzed from southwest to northeast (Figure 3.13). These six disdrometer locations were chosen because they represent a full southwest/northeast transect (-40 km upwind to 56 km downwind; Figure 3.13a,b) and all but one location (F) had second-

generation PARSIVELs available, which makes inter-comparison easier (see section 2d).

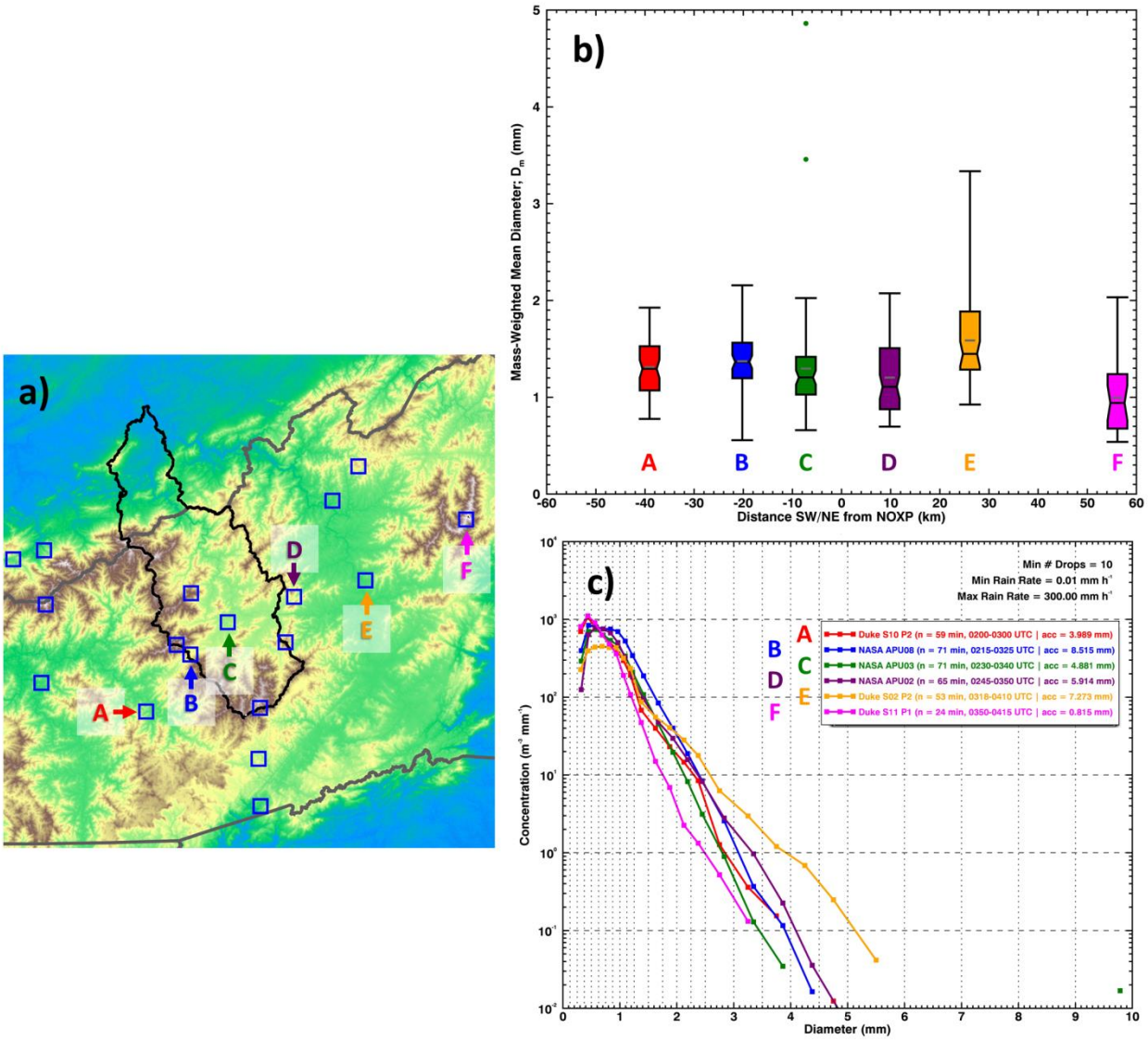

Figure 3.13: a) A terrain elevation map with all PARSIVEL disdrometer locations available during IPHEx identified by blue squares. b) A box and whiskers plot of mass-weighted mean drop diameter (Dm) observed by six PARSIVEL disdrometers during the squall line passage, plot as a function of distance southwest (negative) or northeast (positive) from the NOXP radar location. The black line at the center of the notch represents the median, the grey line represents the mean, the notched region represents the 95% confidence interval of the median, the bottom and top of the color-filled box represent the 25th and 75th quartile, the black whiskers represent the minimum and maximum, and circles above or below the whiskers represent outliers (beyond +/-3 times the interquartile range) in b). c) Mean drop concentration (m^-3 mm^-1) observed by the same six PARSIVEL disdrometers during the squall line passage for 1-minute observations with at least 10 detected drops and rain rates

greater than 0.01 mm/h (no rain rates were observed greater than 300 mm/h). PARSIVEL diameter bin edges are delineated by vertical dotted lines in c). Each of the six analyzed PARSIVEL disdrometers are color-coded and assigned letters A through F. The legend in c) describes the PARSIVEL site name, the number of "rainy minutes" (n) that satisfy the minimum drop and rain rate thresholds, the time range (hhmm-hhmm UTC) encompassing the squall line passage at each PARSIVEL location, and the total rain accumulation over this time period. Five of the PARSIVELs are second generation (A-E) and one is first generation (F). PARSIVELs A-F are also labeled in a). See text for additional information.

Across the Pigeon River Basin, mean and median mass-weighted drop diameter (D_m) and DSD-derived rain accumulation maximized at B along its southwestern boundary (Figure 3.13), co-located with the maximum squall line leading-line convection intensity (Figure 3.6a) and rain accumulation (Figure 3.12). Mean/median D_m reached 1.38/1.38 mm at B, slightly larger but not significantly different than that observed at A (1.31/1.30 mm), with decreasing values observed in the central part of the Pigeon River Basin at C (1.30/1.20 mm) and near the northeast boundary of the Pigeon River Basin at D (1.20/1.10 mm; Figure 3.13a,b). This lines up with the decreasing rain accumulation (Figure 3.12) and squall line leading-line convection intensity (Fig 8a-h) immediately in the lee (northeast) of the main ridge near -20 km from the NOXP radar. The mean DSD at B reveals an increase in mid-sized drops (0.9-2.0 mm) compared to the other gauges, but higher concentrations of large drops (> 3 mm) were observed at D and E (Figure 3.13c). These larger drops observed along the eastern boundary of the Pigeon River Basin at D helped increase the DSD-derived rain accumulation (5.91 mm) compared to the inner valley within the Pigeon River Basin at C (4.88 mm; Figure 3.13c), with similar observations from co-located rain gauges (4.83 mm at C, 6.60 mm at D; Figure 3.12). However, the longer duration rainfall (71 minutes) and more

numerous mid-sized drops at B (0.9-2.0 mm) allowed more rain to accumulate at B (8.52 mm DSD-derived, Figure 3.13c; 9.91 mm observed by rain gauge, Figure 3.12) compared to at D (5.91 mm over 65 minutes, Figure 3.13c). This indicates more consistent and heavier trailing stratiform rainfall was observed at B, which may partially be due to convergence of airflow through the terrain gap in which site B is located (Figures 3.1, 3.13a).

The largest drops and second largest DSD-derived rain accumulation were observed within the downwind valley at E (Figure 3.13), suggesting more intense convective rainfall dominated at E. The highest concentration of drop diameters greater than 2 mm and maximum mean/median D_m (1.60/1.45 mm) was observed at E, but the lowest concentration of small drops (0.4-0.9 mm) was also observed at E (Figure 3.13b,c). Drier air over location E (Figure 3.4a) may have evaporated small drops and thus may be responsible for the lower concentrations of small drops observed at E (Figure 3.13c). D_m reached up to 3.33 mm during the squall line passage at E, well above the maximum D_m of 2.16 mm at B (Figure 3.13b). Note that the outlier D_m values exceeding 3 mm at C were due to hail or non-hydrometeors contaminating the DSD for a 2-minute period where drops greater than 9 mm were observed (not shown). The increased drop sizes at E was also accompanied by the second highest DSD-derived rain accumulation (7.27 mm) out of the six PARSIVELs, which occurred over a shorter period of time (53 minutes) compared to B (71 minutes; Figure 3.13c). Rain gauge observations also show comparable accumulation at E (7.25-7.62 mm), which is the second highest rain

gauge accumulation downwind (northeast) of the NOXP radar location (Figure 3.12a).

Light rainfall and drizzle (accumulation < 1 mm), dominated by large concentrations of small drops (diameters 0.25-0.6 mm) and the smallest mean/median D_m (1.0/0.95 mm), was observed at F as it encountered a brief 24 minutes of precipitation associated with the squall line remnants (Figure 3.13b,c). The higher elevation at site F (1897 m MSL) likely prevented significant evaporation of small drops, like what was observed at the lower elevation site E, even though the driest air was located over this far northeast corner of the IPHEx domain (Figure 3.4a).

These DSD observations indicate stronger convective rainfall (larger drops) impacted location E even though the squall line had weakened and become more disorganized compared to locations B-D. This is likely due to the mountainous terrain disrupting more vigorous convection before reaching PARSIVEL sites A-D, whereas little to no mountainous terrain exists south of site E (Figures 3.1, 3.13a). The full radar time series (supplemental Figure 2) indicates the convection that impacted location E was from cells within the squall line leading line that advected northward out of the UP domain and thus did not interact with the mountainous terrain over the UT domain. This allowed the stronger convection observed over the UP domain (section 4) to maintain its strength longer as it moved over the flatter valley northeast of the Pigeon River Basin. This further supports our hypothesis

that the mountain terrain over the UT domain has a detrimental impact on squall line intensity.

3.7 Discussion and Conclusions

The high-amplitude atmospheric wave pattern and strong southerly moisture transport identified in this IPHEx case is typically observed with extreme precipitation events (EPEs) associated with ARs in the southeastern US (Moore et al. 2012; Moore et al. 2015; Mahoney et al. 2016; Miller et al. 2018). Mahoney et al. (2016) classified an AR in the southeastern US as a plume of IVT values exceeding 500 kg m^{-1} s^{-1} that is longer than it is wide. This IPHEx case easily satisfies these criteria (Figure 3.4). Moore et al. (2012) identified IWV up to 60 mm and IVT exceeding 1400 kg m^{-1} s^{-1} within the AR plume that contributed to a 48-hour flooding event over central Tennessee in May 2010, comparable to IWV (IVT) values of 55 mm (1200 kg m^{-1} s^{-1}) observed during our IPHEx case (Figure 3.4). The deep trough centered over the central US observed during our IPHEx case (Figure 3.3) aligns with the "Strong IVT" nontropical EPE composites identified in Moore at al. (2015) and the AR-influenced EPEs composites identified by Miller et al. (2018), although the 250 mb wave is more amplified during the IPHEx case creating more southerly flow over the southeastern US compared to the dominant southwesterly flow identified in the composites. Studies of EPEs have set varying precipitation accumulation thresholds, but generally an EPE can be classified by precipitation accumulations greater than as little as 75 mm (~ 3 in) over 24 hours in the southern Appalachians, although this varies spatially (Moore at al. 2015). Although the

squall line period analyzed in this IPHEx case only produced up to 23 mm of rainfall (Figure 3.12a), rain gauge analysis over the 24-hour period between 0000 UTC 15 May and 0000 UTC 16 May 2014 shows rainfall up to 100 mm along the southeastern boundary of the southern Appalachians, with 80 mm of rain falling by 1200 UTC 15 May (not shown). Therefore, the squall line analyzed in this IPHEx case could be considered embedded within an EPE that impacted the southeastern slopes of the southern Appalachians, even though this case was not identified in the top 2.5% of rain events observed by the Duke rain gauge network within the Pigeon River Basin between July 2009 and June 2014 (Miller et al. 2018). This is likely due to the faster movement of the system observed during this IPHEx case as the majority of rainfall occurred over ~ 12 hours, compared to 30-282 hour durations for identified EPEs by Miller et al. (2018).

The presence of mesoscale boundaries and organized MCSs within the AR environment played a large role in generating rainfall over the southern Appalachians during this IPHEx case, suggesting these small-scale convective mechanisms are just as important as the AR moisture transport in generating heavy rainfall. This is in contrast to US West Coast AR events, where a strong relationship exists between orographic lift along coastal mountains and precipitation generation (e.g., Neiman et al. 2002), and where reduced upwind surface instability exists due to the cooler Pacific Ocean waters. Mahoney et al. (2016) found that 60% of EPEs in the southeastern US between 2002-2011 were not associated with an AR, suggesting more mesoscale forcing mechanisms were

involved, including orographic and convectively-driven forcings like MCSs. However, larger spatial-scale EPEs were more frequently associated with ARs. This suggests that the combination of MCS maintenance within AR environments impacts more people. Additionally, the combination of strong moisture transport from the nearby warm Gulf of Mexico and Caribbean, deep convection and upscale growth upwind, and forced orographic lift by terrain makes the southern Appalachians a unique location within the US for EPEs to occur.

The southwest-to-northeast propagation of the squall line over the southern Appalachians analyzed in this IPHEx case differs from previous literature investigating squall line interactions with terrain. Although modeling studies frequently show lee-side re-invigoration of squall lines (Frame and Markowski 2006; Letkewicz and Parker 2010, 2011), our analyzed squall line dissipated rapidly beyond ~ 50 km downwind of a major mountain ridge. This is largely due to a strong moisture gradient observed in our case, partly due to physical blocking of low-level moisture by the mountains themselves, which differs significantly from the homogeneous high-instability modeled cases. The AR-transported low-level moisture was the main instability source for continued squall line maintenance in our nocturnal case. Future modeling studies should take into account these natural moisture and instability gradients created by the mountains themselves. Additionally, the squall line observed in our case propagated at least 50 km downwind of the main mountain ridge while maintaining its linear leading-line convection, albeit in a weakened state, whereas model simulations suggest an

almost complete destruction of this leading-line convection for a comparable mountain dimension height of 900 m and radius of 10 km (Frame and Markowski 2006). However, the modeled decrease in surface precipitation on the lee-side slope (within 20 km of the crest; Figures 7, 15 of Frame and Markowski 2006) is comparable to the observed rain accumulation during our IPHEx case (Figure 3.12). One major difference between the squall line analyzed in this paper with previous observational studies (Teng et al. 2000; Parker and Ahijevych 2007), is that the IPHEx squall line propagated from southwest to northeast, roughly perpendicular to the main Appalachian orientation, whereas prior studies focused on squall lines that impacted the mountain range roughly parallel with the higher terrain orientation. This allowed a comparison of the squall line structure both affected and unaffected by high terrain in our study. Additionally, Parker and Ajijevych (2007) only focused on squall lines passing the Appalachians from west to east, whereas the squall line in this paper originated south of the Appalachians. Future observational studies should compare west-to-east crossing MCSs from south-to-north crossing MCSs.

In summary, this paper analyzed a squall line interaction with the southern Appalachian Mountains utilizing high-resolution research radar and surface in-situ observations from the IPHEx field campaign. The main results of this paper are summarized as follows:

- The analyzed squall line was embedded within an AR (Zhu and Newell 1998) and weakened and became disorganized as it propagated from southwest to

northeast due to running into drier air along the leading edge of the AR moisture plume.

- The presence of the southern Appalachians prevented some low-level moisture from traveling farther north due to some combination of physical blocking of the low-level airflow and/or rain-out of moisture through orographic lift and MCSs, which created a strong precipitation accumulation gradient from south to north that is similarly observed in the annual precipitation climatology for this region (PRISM 2017).
- The presence of rough mountainous terrain over and southwest of the Pigeon River Basin (the UT domain) did not support as vigorous of deep convection compared to the flatter terrain south and southeast of the Pigeon River Basin (UP domain), but was more efficient at releasing convective instability along its southeastern slopes.
- A prominent ~ 20 km wide mountain ridge along the southwestern boundary of the Pigeon River Basin, roughly perpendicular to the squall line propagation direction, weakened the squall line leading convective line along its lee slope, as observed by a decrease in radar reflectivity and total rain accumulation from southwest to northeast. The leading-line convection maintained its strength longer in the UP domain devoid of any significant mountain barrier.
- A maximum in rain accumulation occurred along the southeastern boundary of the Pigeon River Basin during the squall line passage due to the presence

of stronger convection and likely additional orographic lift from low-level southeasterly winds.

- Increased rain accumulation and larger drops were observed in the downwind valley (DT domain) northeast of the Pigeon River Basin due to individual convective cells from the UP domain not interacting with high mountain barriers and maintaining its strength longer as they propagated northward (tracking parallel to the leading-line convection).
- Convective rainfall was the dominant microphysical growth process responsible for the heaviest rain accumulation during this quick (~ 1 hour) squall line passage, with little/no orographic enhancement observed.

Future work should focus on more coordinated radar and surface in-situ observations of squall lines interacting with the southern Appalachians. During the 6-week IPHEx IOP, the 15 May 2014 case analyzed in this paper provided one of maybe two cases in which organized convection impacted the IPHEx region. Miller et al. (2018) showed that some years are more active than others in terms of extreme rainfall events in and around the Pigeon River Basin, but generally 3-9 events can be expected in any given year.

High resolution weather models should be coupled with the IPHEx observations from the 15 May 2014 case analyzed in this paper to identify the evolution of the surface cold pool over the complex mountainous terrain of the southern Appalachians. This will help to understand the dynamically-driven processes that the analyzed squall line underwent.

3.8 Acknowledgements

We thank John Kalogiros and Marios Anagnostou from the National Observatory of Athens and Jonathan J. Gourley from NOAA/National Severe Storms Lab for help with processing NOXP radar data. We thank Ana Barros from Duke University for help with Duke instrumentation and site location information. We thank Mike Dixon from NCAR for tireless help with the Radx radar gridding software that was used in our analysis. Finally, we thank Brian Kawzenuk and Forest Cannon from the Center for Western Weather and Water Extremes at Scripps Institution of Oceanography for graciously providing GFS model analysis of Integrated Vapor Transport and Integrated Water Vapor for this case study.

4 Other Work

4.1 Analysis of NOAA G-IV Aircraft Tail Doppler Radar Data Over the Pacific Ocean from the CalWater2 Field Project

This section describes data analysis that I performed for NOAA's Physical Science Division (PSD) that led to two co-authored journal research articles listed below:

Neiman, P. J., B. J. Moore, A. B. White, G. A. Wick, J. Aikins, D. L. Jackson, J. R. Spackman, and F. M. Ralph, 2016: An airborne and ground-based study of a long-lived and intense atmospheric river with mesoscale frontal waves impacting California during CalWater-2014. *Mon. Wea. Rev.*, **144**, 1115–1144, doi:10.1175/MWR-D-15-0319.1.

Neiman, P. J., N. Gaggini, C. W. Fairall, J. Aikins, J. R. Spackman, L. R. Leung, J. Fan, J. Hardin, N. R. Nalli, and A. B. White, 2017: An analysis of coordinated observations from NOAA's Ronald H. Brown ship and G-IV aircraft in a landfalling atmospheric river over the North Pacific during CalWater-2015. *Mon. Wea. Rev.*, **145**, 3647–3669, doi:10.1175/MWR-D-17-0055.1.

Atmospheric rivers (ARs) are vitally important in transporting atmospheric moisture from the tropics to midlatitudes (Zhu and Newell 1998; Ralph et al. 2004), which typically create heavy precipitation as they make landfall along the mountainous coast of the western United States (e.g., Ralph et al. 2006; Neiman et al. 2008; Neiman et al. 2011; Smith et al. 2010; Guan et al. 2010; Ralph and Dettinger 2012). ARs are defined as "long, narrow, and transient corridors of strong horizontal water vapor transport that is typically associated with a low-level jet stream ahead of a cold front of an extratropical cyclone" (AMS 2017; Ralph et al. 2018). ARs are typically identified by satellites and weather models over the open ocean as corridors of increased integrated water vapor (IWV > 2 cm; e.g., Ralph et

al. 2004) and integrated water vapor transport (IVT > 250 kg m^{-1} s^{-1}; e.g., Ralph et al. 2018).

Due to their importance on US West Coast water supply, drought, and flooding (e.g., Ralph et al. 2006; Guan et al. 2010; Dettinger et al. 2011; Kim et al. 2013), AR monitoring techniques have been developed for forecasting purposes (Wick et al. 2013a,b; Cordeira et al. 2017), which have been implemented into real-time weather websites at NOAA[4] and Scripps Institution of Oceanography[5]. Additionally, a suite of surface-based instrumentation has been installed by NOAA and associated partners across California to monitor ARs in real-time and provide forecasts for water managers (White et al. 2013). However, in-situ observations of ARs over the open waters of the Pacific Ocean are less abundant, typically only available from research field projects.

The CalWater project is a multi-year field campaign designed to understand the structure, dynamics, and hydrometeorological impacts of ARs over California as well as the role of aerosols in modifying clouds and precipitation associated with ARs in a changing climate (Ralph et al. 2016). The first phase of the project, termed CalWater-1, took place during 2009-2011 with an increasing number of precipitation, aerosol, surface meteorological, and remote sensing instrumentation deployed each year, with a focus on the Sierra Nevada Mountains, Central Valley, and coast of California. The winter of 2011 provided a valuable dataset that lead to a better understanding of the interaction between overrunning ARs and the Sierra

[4] https://www.esrl.noaa.gov/psd/arportal/
[5] http://cw3e.ucsd.edu/

Barrier Jet (SBJ) over California's Central Valley (Kingsmill 2013; Neiman et al. 2013). The second phase of the project, termed CalWater-2, took place during the winters of 2014 and 2015 and focused on coastal and offshore observations. A key observational facility deployed for CalWater-2 was the NOAA G-IV aircraft instrumented with dropsondes and an X-band tail Doppler radar meant to measure the AR structure well offshore over the open waters of the Pacific Ocean.

My role in assisting with the CalWater-2 research at NOAA's Physical Science Division (PSD) was to 1) de-clutter and de-alias Doppler radar scans from the new NOAA G-IV tail Doppler radar, and 2) grid this quality-controlled NOAA G-IV tail Doppler radar data to a 3-dimensional Cartesian grid in order to analyze the horizontal and vertical distribution of precipitation associated with two offshore ARs on 8-9 February 2014 (Neiman et al. 2016) and 24 January 2015 (Neiman et al. 2017). The NOAA G-IV tail Doppler radar is an X-band (3.22 cm wavelength) single-polarization Doppler radar that includes two flat-plate antennas, with one facing 20° off nadir towards the front of the aircraft (fore scans) and one facing 20° off-nadir towards the rear of the aircraft (aft scans). See the inset image in Figure 4.4 for a diagram of this fore/aft scan strategy. The NOAA G-IV tail Doppler radar is similar to the tail Doppler radar aboard the NOAA WP-3D Orion "Hurricane Hunter" aircraft and is mainly used for hurricane research. One advantage of the NOAA G-IV aircraft is that it can fly at higher altitudes (~14 km MSL) than the NOAA WP-3D Orion (~8 km MSL), which allows full vertical profiles of clouds and precipitation through the majority of the troposphere by the tail Doppler radar.

Because the NOAA G-IV tail Doppler radar was mainly used for hurricane forecasting and research, no one had used it to document the spatial structure of clouds and precipitation within an extratropical cyclone, so the analysis presented here was one of the first of its kind.

The first step in this analysis involved identifying straight flight legs where the aircraft was not turning, so I plotted aircraft flight data, including flight altitude, flight track location, aircraft pitch and roll angles, aircraft heading and track angles, and air and ground speeds. Sections of the flight track that had a consistent track angle, roll angles near zero, and no major altitude and pitch angle changes were designated flight legs. Additionally, the tail Doppler radar scans were used to identify flight sections within these straight flight legs where clouds and precipitation were observed. An example of this flight data is plotted in Figure 4.1 for the flight leg (LEG02precip) used in the analysis for Neiman et al. (2017).

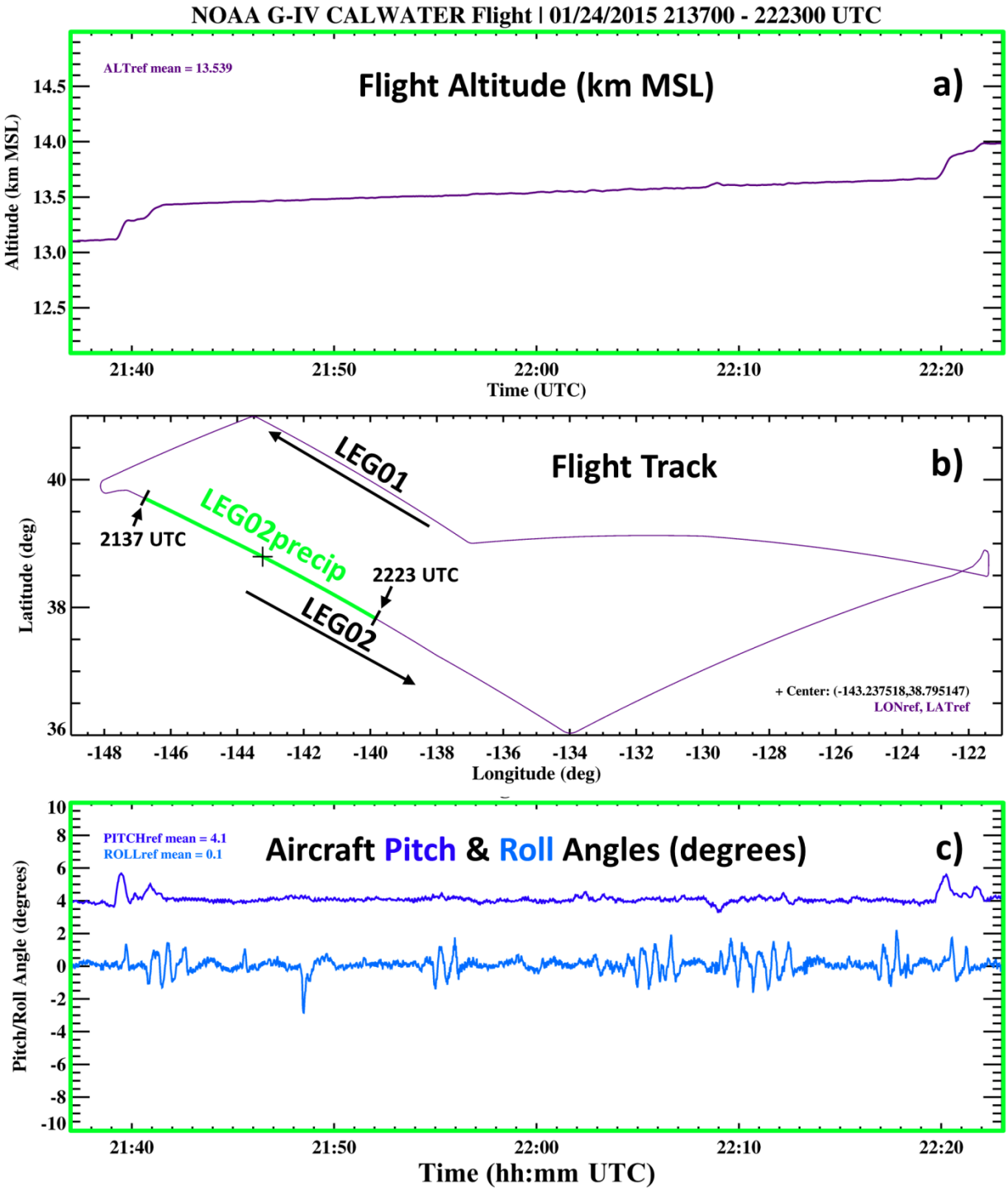

Figure 4.1: The a) flight altitude, b) flight track latitude and longitude location, and c) aircraft pitch and roll angles are plotted between 2137 UTC and 2223 UTC on 24 January 2015 for the NOAA G-IV aircraft. The full flight track is shown in purple in b) with the LEG02precip flight leg identified by green. The center location of the LEG02precip flight leg is identified in b) as a black cross, with its corresponding latitude and longitude value labeled in the bottom right corner. Mean flight altitude (km MSL) is labeled in a), and mean pitch and roll angles are labeled in c).

The next step in the analysis involved editing individual tail Doppler radar scans (sweeps) within the flight legs in order to remove radar echoes that did not correspond with cloud or precipitation particles (non-hydrometeor echoes). Non-hydrometeor echoes were identified by inspecting clear-air sweeps. Figure 4.2 shows an example clear-air sweep on 8 February 2014 with the three major non-hydrometeor echoes, including i) the ocean surface, ii) radar side-lobe contamination above the ocean surface in a ring surrounding the aircraft location, and iii) speckling of random noise. These non-hydrometeor echoes are considered clutter and were manually removed through hand-editing using the Soloii radar software. Additionally, Doppler velocity fields for each sweep were corrected for aircraft motion, following the approach documented by Lee et al. (1994), and de-aliased using Soloii. This resulted in the hand-editing of a total of 980 sweeps (46 minutes of flight time) for the 24 January 2015 CalWater-2 flight and a total of 1431 sweeps (67 minutes of flight time) for the 8-9 February 2014 flight, including both fore and aft scans with a complete 360° rotation taking ~ 6 seconds. An example comparison of un-corrected and corrected reflectivity and Doppler velocity fields is shown in Figure 4.3 for one sweep during the 24 January 2015 CalWater flight leg. Notice the side-lobe clutter is sometimes over-powered by the precipitation echoes. The variance (or texture) of the Doppler velocity field was key in distinguishing clutter from hydrometeor echoes during sweeps like these, where increased Doppler velocity texture indicated potential clutter contamination.

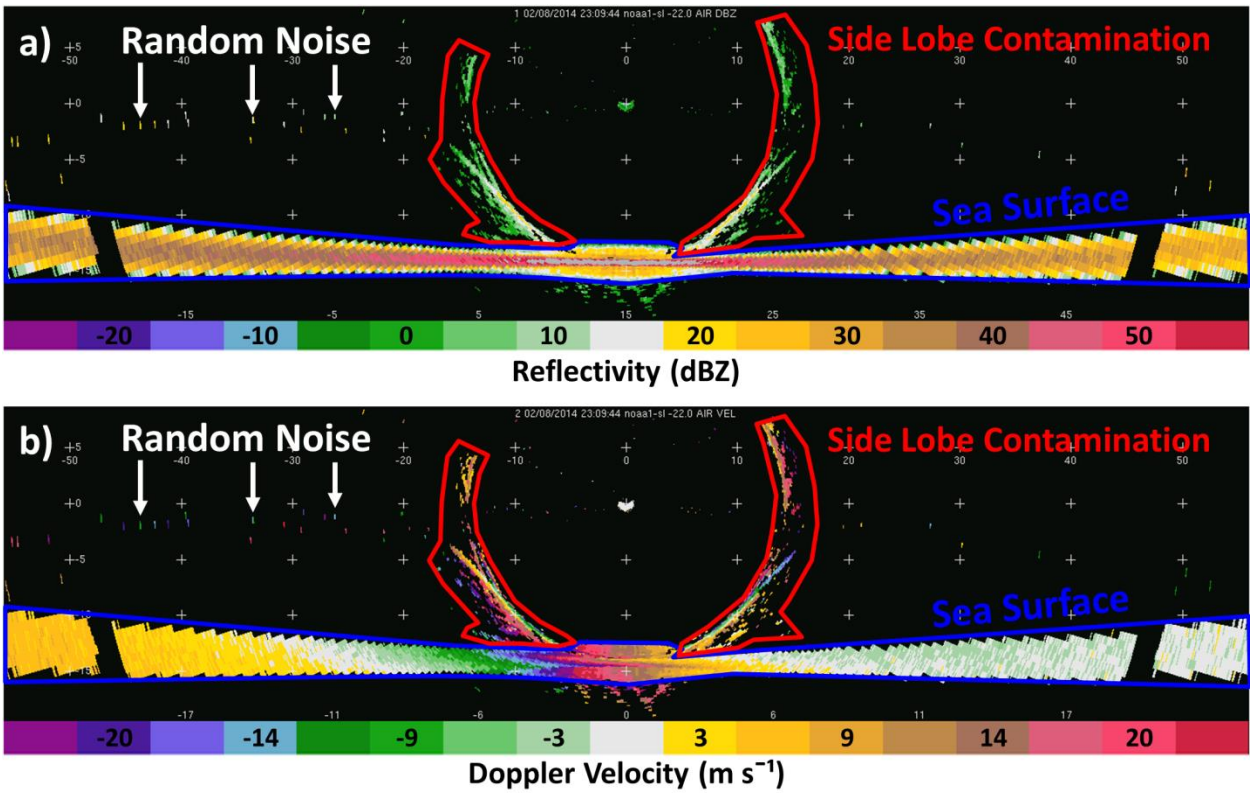

Figure 4.2: A single aft (rear-facing) scan from the NOAA G-IV tail Doppler radar at 23:09:44 UTC 8 February 2014 showing a) reflectivity and b) Doppler velocity. The data shown in this figure are prior to removal of non-hydrometeor echoes and Doppler velocity correction for aircraft motion. Non-hydrometeor echoes (clutter artifacts) are identified within the figure.

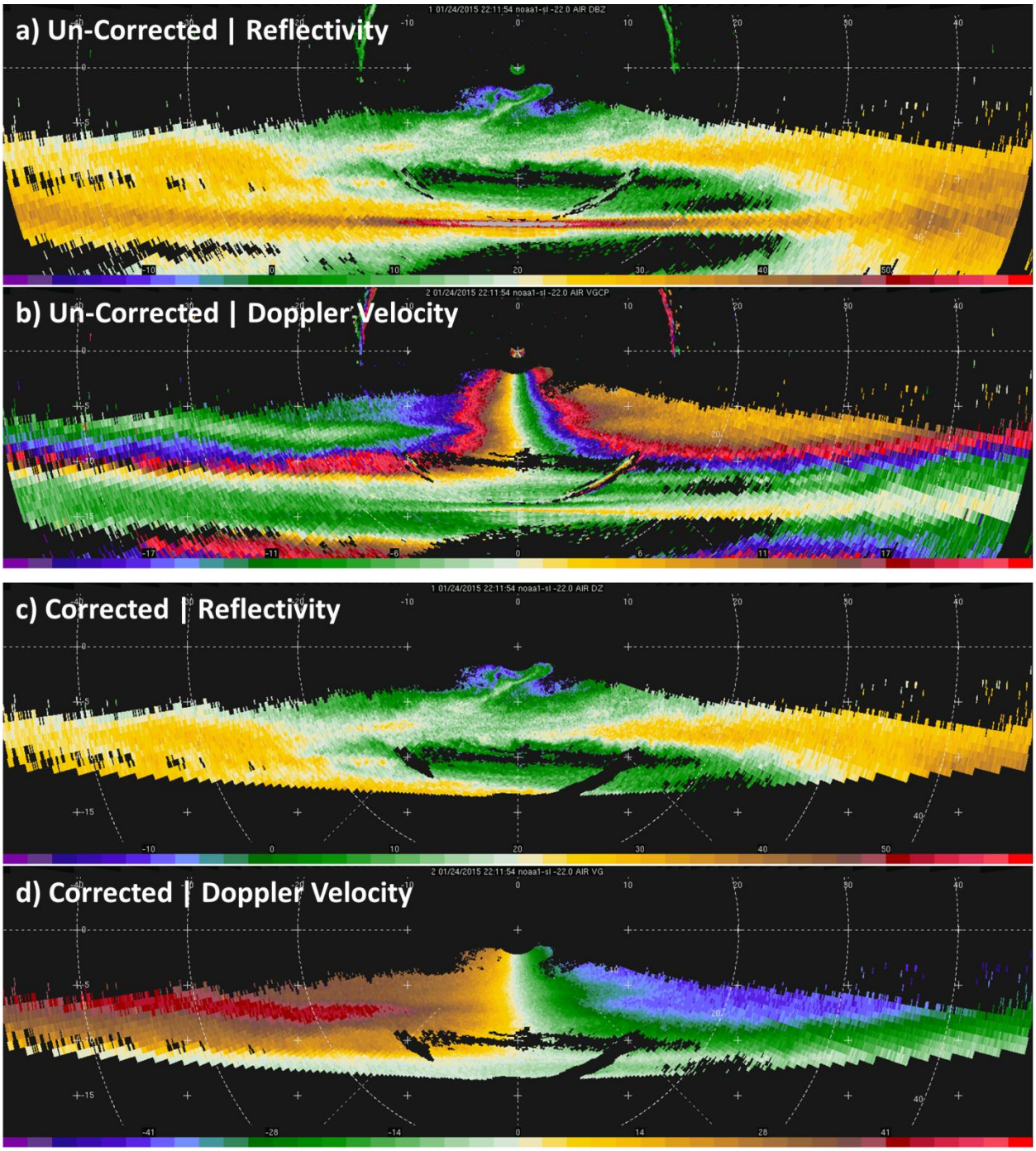

Figure 4.3: Raw un-corrected a) reflectivity and b) Doppler velocity from the NOAA G-IV tail Doppler radar at 22:11:54 UTC on 24 January 2015 during a CalWater-2 flight. Reflectivity after removing non-hydrometeor clutter is shown in c) for the same scan shown in a). Doppler velocity after removing non-hydrometeor clutter, correcting for aircraft motion, and de-aliasing is shown in d) for the same scan shown in b). The reflectivity and Doppler velocity colorbar is shown at the bottom of each panel. Note that the Doppler velocity colorbar changes from b) to d) due to the larger de-aliased Doppler velocities in d).

The final piece of the analysis involved using the NCAR legacy REORDER software to map the de-cluttered NOAA G-IV tail Doppler radar sweeps to a 3-dimensional Cartesian grid. Each flight leg center point, calculated as the location half way between the start and stop time of the leg and shown in Figure 4.1 for the 24 January 2015 flight, is used as the grid origin. The optimal horizontal grid spacing was determined based on the mean ground speed (210-230 m s^{-1}) of the aircraft and the time to collect a full radar sweep (~ 6 seconds), which resulted in repeat observations every 1.3-1.4 km in the along-track distance. To ensure that at least one radar range gate existed within each horizontal grid cell, I set the horizontal grid resolution to 1.5 km. The optimal vertical grid spacing was set to 0.5 km based on the width of the radar beam at ~ 30 km from the aircraft, which was the farthest distance used in the analysis due to degrading sensitivity and increasing beam broadening preventing detailed visualization of the vertical structure of clouds and precipitation. Figure 4.4 provides a horizontal view example of the gridded reflectivity field at 2 km above mean sea level for leg 2 of the 24 January 2015 CalWater-2 flight. Figure 4.5 shows the mean gridded reflectivity vertical cross-section corresponding to the same flight leg as Figure 4.4. Together, these horizontal and vertical gridded fields provide a complete picture of the structure of precipitation over the open ocean within this AR.

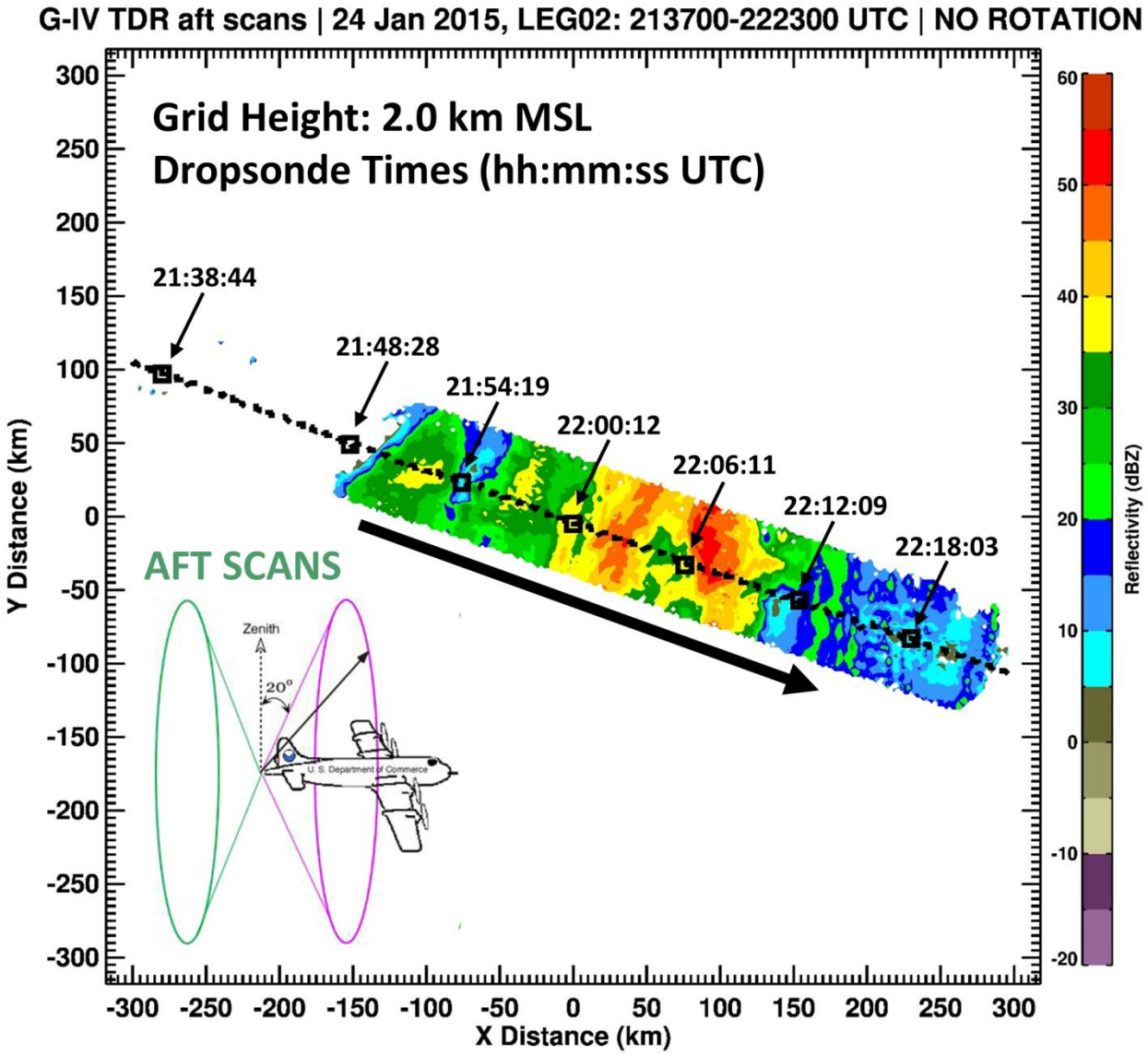

Figure 4.4: Gridded NOAA G-IV tail Doppler radar reflectivity at 2 km above mean sea level during 2137-2223 UTC on 24 January 2015 (LEG02). The gridded reflectivity field was derived from aft scans only, and the flight direction is indicated with the thick black arrow. The grid was un-rotated, so the y-axis aligns with north. The locations of dropsondes released during this flight leg are labeled with a black square and their corresponding drop time. The reflectivity colorbar is shown on the right.

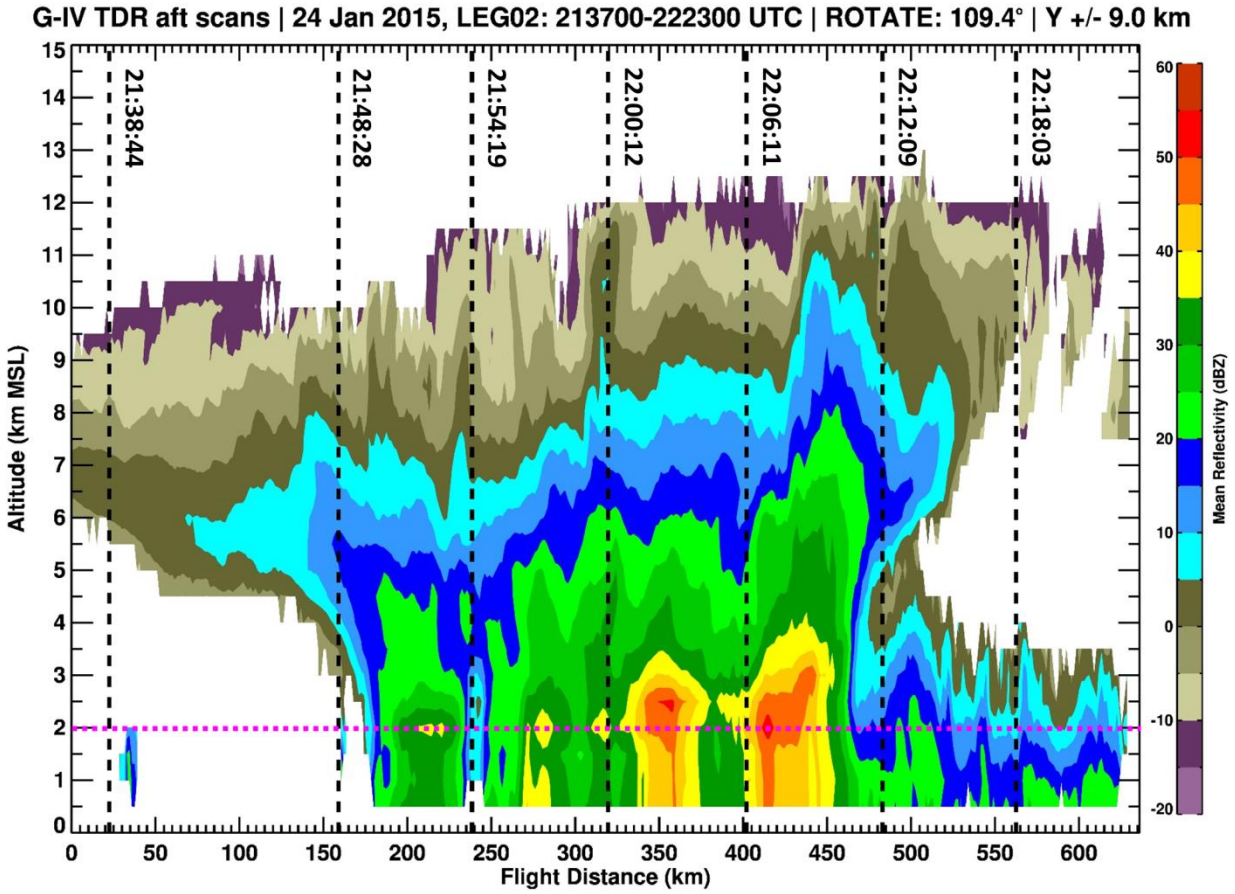

Figure 4.5: Vertical cross-section of mean gridded NOAA G-IV tail Doppler radar reflectivity within +/-9 km of the aircraft in the cross-track direction during 2137-2223 UTC on 24 January 2015 (LEG02). The times and locations (vertical dashed line) that dropsondes were released are labeled. The horizontal dotted pink line indicates the altitude at which Figure 4.4 was plotted. The flight distance x-axis is aligned with the mean flight track during this flight leg of 109.4° from north. The reflectivity colorbar is shown at the right.

The horizontal and vertical structure of precipitation visualized by my first-of-a-kind gridded NOAA G-IV tail Doppler radar analyses was analyzed in reference to the thermodynamic structure of two ARs during the CalWater-2 project and incorporated into two co-authored journal articles (Figure 15 of Neiman et al. 2016; Figure 13 of Neiman et al. 2017). The varying bright band indicated by my NOAA G-IV tail Doppler radar analysis was useful in verifying the sloping freezing level from higher altitudes over the warm sector of the AR to lower altitudes behind the

surface cold front associated with the extratropical cyclone. My analysis was also vital in distinguishing between deep stratiform, convective, and shallow warm rainfall, which aligned with surface disdrometer observations from a ship located along the leg 2 G-IV flight path (Neiman et al. 2017). Overall, these papers are contributing to our understanding of the thermodynamic and microphysical properties of ARs over data-sparse regions of the open ocean.

4.2 The 2017 Seeded and Natural Orographic Wintertime clouds - The Idaho Experiment (SNOWIE)

This section describes my work operating and maintaining radars and in-situ instrumentation during the SNOWIE field project as the lead CU Boulder graduate student. This field work has lead to one co-authored paper listed below:

Tessendorf, S. A., J. French, K. Friedrich, B. Geerts, R. M. Rauber, R. M. Rasmussen, L. Xue, K. Ikeda, D. R. Blestrud, M. L. Kunkel, S. Parkinson, J. R. Snider, J. Aikins, S. Faber, A. Majewski, C. Grasmick, A. Janiszeski, A. Springer, C. Weeks, D. J. Serke, and R. Bruintjes, 2018: Transformational approach to winter orographic weather modification research: The SNOWIE Project. Submitted to *The Bulletin of the American Meteorological Society*, March 2018.

The Seeded and Natural Orographic Wintertime Clouds: The Idaho Experiment (SNOWIE)[6] field project took place between 7 January and 17 March

[6] https://www.eol.ucar.edu/field_projects/snowie

2017 in the Payette River Basin of central Idaho, with a dual goal of understanding 1) the natural dynamical and microphysical processes by which precipitation forms and evolves within orographic winter storms and 2) the physical processes by which cloud seeding with silver iodide (AgI) impacts the amount and spatial distribution of snow falling across a river basin. The SNOWIE project builds upon the ASCII project, explained in section 2, and allowed partnering with the private sector (Idaho Power Company, IPC), who maintain an operational seeding program in the study region. Additionally, the SNOWIE project provided airborne seeding opportunities, whereas only ground-based seeding was possible during the ASCII project. Cloud seeding to boost mountain snowpack is being increasingly pursued in the western US due to strains on water resources from population growth and a warming climate, but the effectiveness of cloud seeding is still scientifically uncertain. The dataset collected during SNOWIE will assist in reducing the uncertainties associated with glaciogenic cloud seeding as well as provide unique observations of natural snow growth and fallout within an orographic winter environment.

My role during the SNOWIE project was to operate the two X-band Doppler On Wheels (DOW) mobile radars and set up and maintain the University of Colorado Particle Size and Velocity (PARSIVEL) optical disdrometer, Micro Rain Radar (MRR), and microwave radiometer. One DOW radar was deployed at 7000 ft elevation on a mountain ridge site called Packer John, and the second DOW radar was deployed at 8000 ft elevation on a mountain ridge ~ 25 km to the northwest of

Packer John at a site called Snowbank. These DOW radars were the core observing facility during SNOWIE as they provided surveillance scans of clouds and precipitation over the SNOWIE study area before, during, and after cloud seeding. Due to their remote locations, transportation to and from the DOW radars was mainly via snowmobile, and nights were spent in a camper nearby the radar. During intensive observational periods (IOPs) my job was to ensure the DOW radar truck was level, run pre-programmed plan position indicator (PPI) and range height indicator (RHI) scan sequences, troubleshoot any software or hardware malfunctions, and maintain a detailed log documenting scan sequence changes, radar down times due to malfunctions, and periodic weather observations. The University of Colorado PARSIVEL disdrometer and MRR were installed at the Packer John site, so during IOPs at Packer John I was also responsible for starting/stopping their data collection and clearing rime ice buildup that could prevent reliable observations. In total, I assisted in data collection for all but one of the 24 IOPs during the SNOWIE field campaign, which resulted in the largest dataset collected by the DOW radars for a single field project.

Following the SNOWIE field deployment, I have been assisting with de-cluttering DOW radar data and mapping these corrected data to the mountainous terrain of central Idaho using the techniques developed during my PhD research presented in section 2 and 3 of this dissertation. The fuzzy-logic de-cluttering algorithm that I adapted from Gourley et al. (2007) and implemented on the DOW radar data from ASCII (section 2) has shown to work well on the SNOWIE DOW

radar data as well (Figure 4.6). Due to its useage of dual-polarization fields, this fuzzy-logic de-cluttering algorithm removes obvious ground clutter (high reflectivity regions) as well as less-obvious side-lobe contamination well above the terrain surface that is difficult to discern from hydrometeor echoes using reflectivity alone. The corrected DOW radar data has already been used in one published study to provide unambiguous evidence that glaciogenic cloud seeding can enhance natural snow growth and fallout within the Payette Basin for one SNOWIE IOP, moisture that would otherwise have fallen out farther downstream (French et al. 2018). These data are also being used in a recently submitted co-authored Bulletin of the American Meteorological Society (BAMS) research paper highlighting three IOPs where clear airborne glaciogenic cloud seeding resulted in enhanced snow growth and fallout within the targeted Payette Basin (Tessendorf et al. 2018). These studies, and numerous future ones, are providing the best-ever observations of cloud seeding working and will help identify the optimal atmospheric conditions under which cloud seeding is effective, thus providing ground-breaking results in the cloud seeding research field.

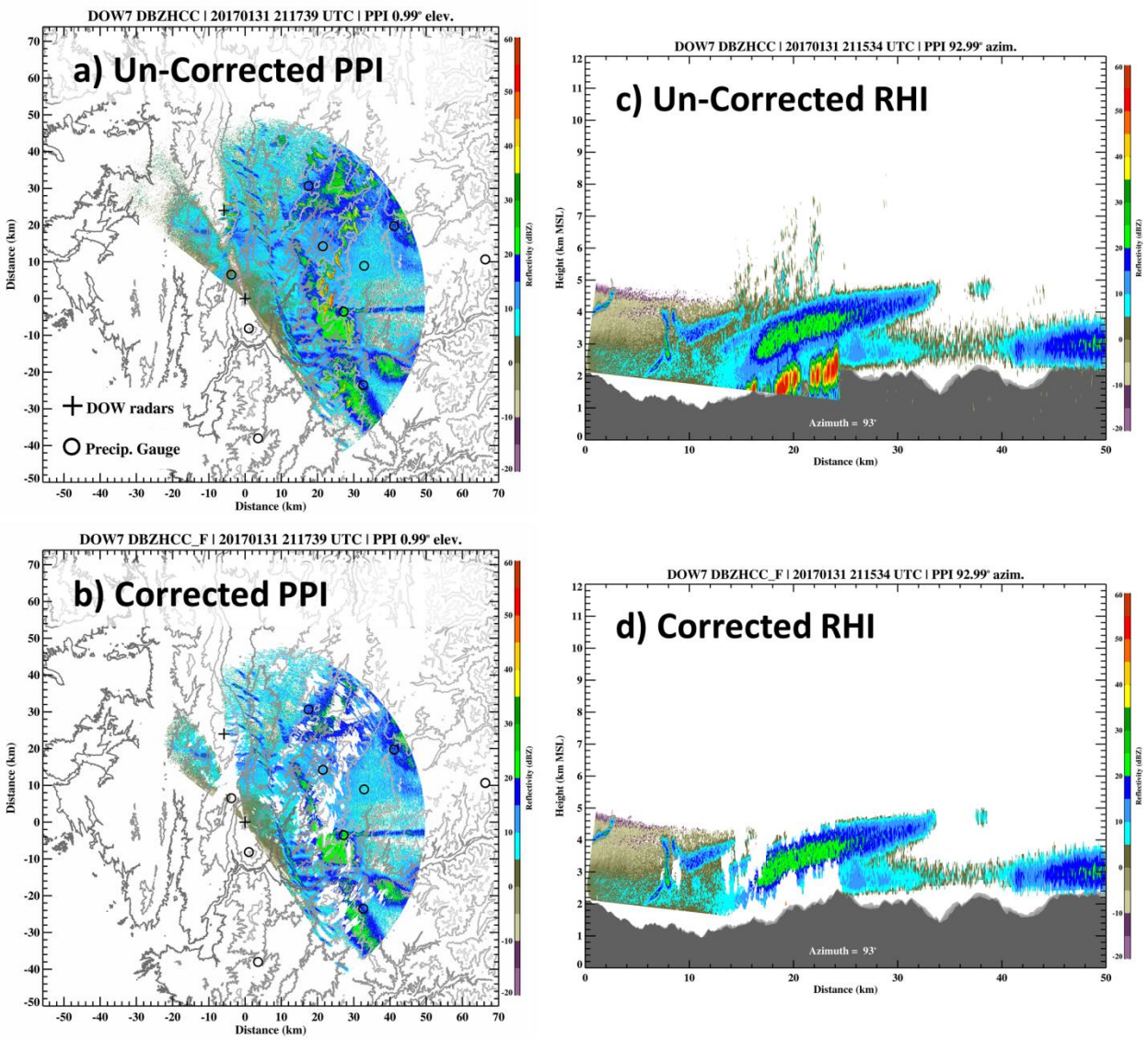

Figure 4.6: Reflectivity observations from the DOW radar at Packer John (DOW7) both a), c) before and b), d) after correction through removal of ground clutter. A PPI scan at an elevation of 0.99° at 21:17:39 UTC on 31 January 2017 (SNOWIE IOP09) is shown in a) and b). An RHI scan at an azimuth of 92.99° at 21:15:34 UTC on 31 January 2017 (SNOWIE IOP09) is shown in c) and d). USGS terrain elevation contours are overlaid every 500 m in shades of grey in a) and b), with darker shades of grey for lower elevations and lighter grey for higher elevations. Similarly, the minimum (dark grey), mean (medium grey), and maximum (light grey) USGS terrain elevation profile is overlaid in c) and d) corresponding to the terrain within a 1° beam width centered on the closest azimuth whole degree of the RHI scan. The location of the DOW radars are identified with black crosses and nearby precipitation gauges are identified with black circles in a) and b).

5 Overall Conclusions

5.1 Summary of Major Findings

In section 2 of this dissertation I explored small-scale dynamical mechanisms associated with strong wind shear and induced turbulence that affected microphysical growth of snow within a cold post-frontal orographic environment over an interior mountain range. I utilized a suite of in-situ and remote sensing observations to show theorized microphysical processes in action and highlight the importance of small scale motions (sub-kilometer scale up to ~ 1 km) on these microphysical processes. This work also extended the research of shear-induced turbulent zones near the top of de-coupled low-level environments to a small mountain range within the interior of the western US, which had previously only focused on US West Coast mountain ranges where warmer and moister environments create very different microphysical growth mechanisms. The work presented in section 2 is important for operational weather forecasting within the mountainous interior region of the western US, as well as other mountainous regions of the world, because these small-scale mechanisms cannot currently be resolved by operational numerical weather forecast models.

In section 3 of this dissertation I utilized a suite of in-situ surface observations and two research radars to document the impact of mountainous terrain on an organized MCS (squall line) within an AR in the southeastern US. My findings suggest that the Appalachian Mountains weaken the convection associated with the squall line but support more persistent microphysical growth along upwind

mountain slopes, both through release of instability and persistent orographic rising motion. Alternatively, downslope flow in the lee of a major mountain ridge suppressed rainfall, both by weakening convection and evaporation. The blockage of low-level moisture by the Appalachian Mountains was also apparent, leading to reduced instability in the lee during this nocturnal case study. This work is one of very few that has used observations to document the orographic modification of MCSs. Previous work has largely focused on understanding the kinematics and microphysics of MCSs over the flat terrain of the US Great Plains. Additionally, the impacts of ARs over the eastern US is something that has only recently started to be investigated as the majority of the AR literature has focused on ARs over the Pacific Ocean and US West Coast. My work in section 3 has shown the importance of mesoscale features, specifically convection and MCSs, within the larger AR moisture transport in generating heavy rainfall along the southeastern boundary of the Appalachians in the southeastern US. This differs from the impacts of ARs along the US West Coast, where strong orographic lift is the primary mechanism for heavy rainfall associated with landfalling ARs. The lack of strong instability upwind over the cool waters of the Pacific Ocean likely limit MCS development. The work presented in section 3 is important for forecasting the maintenance or dissipation of MCSs that impact the Appalachians, which can sometimes be associated with severe weather hazards like strong straight-line winds and hail.

My additional work presented in section 4.1 and 4.2 has helped show rare observations to the world, including precipitation structures within an AR over the

data-sparse Pacific Ocean (section 4.1) and the best-ever evidence of glaciogenic cloud seeding creating man-made precipitation over a river basin (section 4.2). This work has already been used in research studies to advance our understanding of precipitation generation in our atmosphere, both by natural and man-made mechanisms, and will continue to be used in future studies.

The over-arching theme of this dissertation is to document the small-scale mechanisms present in our atmosphere that affect precipitation growth and fallout, especially mechanisms associated with mountainous terrain. With today's advancing instrumentation, higher resolution and higher quality observations are being collected by scientists in the atmospheric sciences research field. It is vital that we continue to utilize these observations to back up or refute previous theoretical and observational findings as well as advance the field by identifying new mechanisms that may have previously been unobservable. The work presented in this dissertation has contributed to both of these areas.

5.2 Future Work

A treasure trove of additional observations are still available from the ASCII project as I only focused on one IOP for my analysis in section 2. A total of 17 IOPs are available from the ASCII dataset. Additional work on this dataset could include documenting additional cases where a turbulent shear layer influenced precipitation generation and comparing the microphysical growth mechanism induced by these turbulent shear layers with that observed during the analyzed

IOP2 case. Additionally, high-resolution mesoscale models could be run for the ASCII domain both over the course of the field mission as well as extended to a full year or decade to identify additional periods in which these turbulent shear zones are present. This would give a better understanding of the prevalence of turbulent shear zones in modifying precipitation in the climatology of this interior mountain region of the US.

Similarly, much more data is available from the IPHEx project as I only focused on one 4-hour period of observations during the 46-day field campaign. Additional work could focus on identifying additional cases where MCSs impacted the IPHEx region and comparing these interactions with my analysis from the 15 May 2014 case. Does the time-of-day and/or presence of an AR matter in determining how the Appalachians impact MCSs? It would also be valuable to run a high-resolution mesoscale model with realistic terrain over the IPHEx domain during the squall line case analyzed in section 3 to document terrain modifications of the cold pool and other kinematics associated with the squall line. This would give a more complete picture of the orographic modification of the squall line dynamics, especially at the lowest levels closest to the terrain, something that the radars were unable to observe.

I plan on working with the incredible SNOWIE dataset to continue my research on identifying natural small-scale mechanisms that influence orographic precipitation generation as well as to implement and improve my radar de-cluttering algorithm. Also, the availability of two DOW radars during SNOWIE may

allow a dual-Doppler radar analysis over the Payette River Basin, which could document the three-dimensional airflow over this mountainous terrain. This would be valuable in understanding what controls the precipitation distribution over the Payette River Basin and potentially identify optimal cloud seeding strategies.

References

American Meteorological Society (AMS), 2017: Atmospheric river. *Glossary of Meteorology*, http://glossary.ametsoc.org/wiki/Atmospheric_river.

Anagnostou, M. N., J. Kalogiros, F. S. Marzano, E. N. Anagnostou, M. Montopoli, and E. Piccioti, 2013: Performance evaluation of a new dual-polarization microphysical algorithm based on long-term X-band radar and disdrometer observations. *J. Hydrometeor.*, **14**, 560–576, doi:10.1175/JHM-D-12-057.1.

Andrić, J., D. Zrnić, J. M. Straka, and V. Melnikov, 2010: The enhanced ZDR signature in stratiform clouds above melting layer. *13th Conf. on Cloud Physics*, Portland, OR, Amer. Meteor. Soc., P2.89. [Available online at https://ams.confex.com/ams/pdfpapers/171308.pdf.]

Andrić, J., M. R. Kumjian, D. S. Zrnić, J. M. Straka, and V. M. Melnikov, 2013: Polarimetric signatures above the melting layer in winter storms: An observational and modeling study. *J. Appl. Meteor. Climatol.*, **52**, 682–700, doi:10.1175/JAMC-D-12-028.1.

Atlas, D., R. C. Srivastava, and R. S. Sekhon, 1973: Doppler radar characteristics of precipitation at vertical incidence. *Rev. Geophys.*, **11**, 1–35, doi:10.1029/RG011i001p00001.

Bailey, M. P., and J. Hallett, 2009: A comprehensive habit diagram for atmospheric ice crystals: Confirmation from the laboratory, AIRS II, and other field studies. *J. Atmos. Sci.*, **66**, 2888–2899, doi:10.1175/2009JAS2883.1.

Bardsley, T., A. Wood, M. Hobbins, T. Kirkham, L. Briefer, J. Niermeyer, and S. Burian, 2013: Planning for an uncertain future: Climate change sensitivity assessment toward adaptation planning for public water supply. *Earth Interact.*, **17**, 1–26, doi:10.1175/2012EI000501.1.

Barros, A. P. and Coauthors 2014: NASA GPM-ground validation: Integrated Precipitation and Hydrology Experiment 2014 science plan. NASA. Text. http://dx.doi.org/10.7924/G8CC0XMR.

Battaglia, A., E. Rustemeier, A. Tokay, U. Blahak, and C. Simmer, 2010: PARSIVEL snow observations: A critical assessment. *J. Atmos. Oceanic Technol.*, **27**, 333–344, doi:10.1175/2009JTECHA1332.1.

Beard, K. V., 1976: Terminal velocity and shape of cloud and precipitation drops aloft. *J. Atmos. Sci.*, **33**, 851–864, doi:10.1175/1520-0469(1976)033<0851:TVASOC>2.0.CO;2.

Beard, K. V., 1977: Terminal velocity adjustment for cloud and precipitation drops aloft. *J. Atmos. Sci.*, **34**, 1293–1298, doi:10.1175/1520-0469(1977)034<1293:TVAFCA>2.0.CO;2.

Bechini, R., L. Baldini, and V. Chandrasekar, 2013: Polarimetric radar observations in the ice region of precipitating clouds at C-band and X-band radar frequencies. *J. Appl. Meteor. Climatol.*, **52**, 1147–1169, doi:10.1175/JAMC-D-12-055.1.

Blanchard, D. O., 1990: Mesoscale convective patterns of the southern high plains. *Bull. Amer. Meteor. Soc.*, **71**, 994–1005, doi:10.1175/1520-0477(1990)071<0994:MCPOTS>2.0.CO;2.

Bluestein, H. B., and M. H. Jain, 1985: Formation of mesoscale lines of precipitation: Severe squall lines in Oklahoma during the spring. *J. Atmos. Sci.*, **42**, 1711–1732, doi:10.1175/1520-0469(1985)042<1711:FOMLOP>2.0.CO;2.

Bluestein, H. B., G. T. Marx, and M. H. Jain, 1987: Formation of mesoscale lines of precipitation: Nonsevere squall lines in Oklahoma during the spring. *Mon. Wea. Rev.*, **115**, 2719–2727, doi:10.1175/1520-0493(1987)115<2719:FOMLOP>2.0.CO;2.

Brandes, E. A., K. Ikeda, G. Thompson, and M. Schönhuber, 2008: Aggregate terminal velocity/temperature relations. *J. Appl. Meteor. Climatol.*, **47**, 2729–2736, doi:10.1175/2008JAMC1869.1.

Brandes, E. A., K. Ikeda, G. Zhang, M. Schönhuber, and R. M. Rasmussen, 2007: A statistical and physical description of hydrometeor distributions in Colorado snowstorms using a video disdrometer. *J. Appl. Meteor. Climatol.*, **46**, 634–650, doi:10.1175/JAM2489.1.

Bureau of Reclamation, 2016: SECURE Water Act Section 9503(c): Reclamation Climate Change and Water 2016. Bureau of Reclamation Rep., 307 pp. [Available online at https://www.usbr.gov/climate/secure/docs/2016secure/2016SECUREReport.pdf.]

Chong, M., P. Amayenc, G. Scialom, and J. Testud, 1987: A tropical squall line observed during the COPT 81 Experiment in West Africa. Part 1: Kinematic structure inferred from dual-Doppler radar data. *Mon. Wea. Rev.*, **115**, 670–694, doi:10.1175/1520-0493(1987)115<0670:ATSLOD>2.0.CO;2.

Ciach, G. J., 2003: Local random errors in tipping-bucket rain gauge measurements. *J. Atmos. Oceanic Technol.*, **20**, 752–759, doi:10.1175/1520-0426(2003)20<752:LREITB>2.0.CO;2.

Cordeira, J. M., F. M. Ralph, A. Martin, N. Gaggini, J. R. Spackman, P. J. Neiman, J. J. Rutz, and R. Pierce, 2017: Forecasting atmospheric rivers during CalWater 2015. *Bull. Amer. Meteor. Soc.*, **98**, 449–459, doi:10.1175/BAMS-D-15-00245.1.

Cosma, S., E. Richard, and F. Miniscloux, 2002: The role of small-scale orographic features in the spatial distribution of precipitation. *Quart. J. Roy. Meteor. Soc.*, **128**, 75–92, doi:10.1256/00359000260498798.

Dettinger, M. D., F. M. Ralph, T. Das, P. J. Neiman, and D. R. Cayan, 2011: Atmospheric rivers, floods and the water resources of California. *Water*, **3**, 445–478, doi:10.3390/w3020445.

Duchon, C. E., and C. J. Biddle, 2010: Undercatch of tipping-bucket gauges in high rain rate events. *Adv. Geosci.*, **25**, 11–15, doi:10.5194/adgeo-25-11-2010.

Duchon, C. E., and G. R. Essenberg, 2001: Comparative rainfall observations from pit and aboveground rain gauges with and without wind shields. *Water Resour. Res.*, **37**, 3253–3263, doi:10.1029/2001WR000541.

Duchon, C. E., C. Fiebrich, and D. Grimsley, 2014: Using high-speed photography to study undercatch in tipping-bucket rain gauges. *J. Atmos. Oceanic Technol.*, **31**, 1330–1336, doi:10.1175/JTECH-D-13-00169.1.

Fovell, R. G., G. L. Mullendore, and S.-H. Kim, 2006: Discrete propagation in numerically simulated nocturnal squall lines. *Mon. Wea. Rev.*, **134**, 3735–3752, doi:10.1175/MWR3268.1.

Frame, J., and P. Markowski, 2006: The interaction of simulated squall lines with idealized mountain ridges. *Mon. Wea. Rev.*, **134**, 1919–1941, doi:10.1175/MWR3157.1.

French, J. R., and Coauthors, 2018: Precipitation formation from orographic cloud seeding. *Proc. Natl. Acad. Sci. USA*, doi:10.1073/pnas.1716995115.

Friedrich, K., E. A. Kalina, F. J. Masters, and C. R. Lopez, 2013: Drop-size distributions in thunderstorms measured by optical disdrometers during VORTEX2. *Mon. Wea. Rev.*, **141**, 1182–1203, doi:10.1175/MWR-D-12-00116.1.

Garvert, M. F., B. Smull, and C. Mass, 2007: Multiscale mountain waves influencing a major orographic precipitation event. *J. Atmos. Sci.*, **64**, 711–737, doi:10.1175/JAS3876.1.

Geerts, B., and Coauthors, 2013: The AgI Seeding Cloud Impact Investigation (ASCII) campaign 2012: Overview and preliminary results. *J. Wea. Mod.*, **45**, 24–43.

Geerts, B., Q. Miao, and Y. Yang, 2011: Boundary layer turbulence and orographic precipitation growth in cold clouds: Evidence from profiling airborne radar data. *J. Atmos. Sci.*, **68**, 2344–2365, doi:10.1175/JAS-D-10-05009.1.

Geerts, B., R. Damiani, and S. Haimov, 2006: Finescale vertical structure of a cold front as revealed by an airborne Doppler radar. *Mon. Wea. Rev.*, **134**, 251–271, doi:10.1175/MWR3056.1.

Geerts, B., Y. Yang, R. Rasmussen, S. Haimov, and B. Pokharel, 2015: Snow growth and transport patterns in orographic storms as estimated from airborne vertical-plane dual-Doppler radar data. *Mon. Wea. Rev.*, **143**, 644–665, doi:10.1175/MWR-D-14-00199.1.

Gossard, E. E., R. G. Strauch, D. C. Welsh, and S. Y. Matrosov, 1992: Cloud layers, particle identification, and rain-rate profiles from ZRVf measurements by clear-air Doppler radars. *J. Atmos. Oceanic Technol.*, **9**, 108–119, doi:10.1175/1520-0426(1992)009<0108:CLPIAR>2.0.CO;2.

Gourley, J. J., P. Tabary, and J. Parent du Chatelet, 2007: A fuzzy logic algorithm for the separation of precipitating from nonprecipitating echoes using polarimetric radar observations. *J. Atmos. Oceanic Technol.*, **24**, 1439–1451, doi:10.1175/JTECH2035.1.

Gowan, T. M., W. J. Steenburgh, and C. S. Schwartz, 2018: Validation of mountain precipitation forecasts from the convection-permitting NCAR Ensemble and operational forecast systems over the western United States. *Wea. Forecasting*, **33**, 739–765, doi:10.1175/WAF-D-17-0144.1.

Guan, B., N. P. Molotch, D. E. Waliser, E. J. Fetzer, and P. J. Neiman, 2010: Extreme snowfall events linked to atmospheric rivers and surface air temperature via satellite measurements. *Geophys. Res. Lett.*, **37**, L20401, doi:10.1029/2010GL044696.

Hindman, E. E., 1986: Characteristics of supercooled liquid water in clouds at mountaintop sites in the Colorado Rockies. *J. Climate Appl. Meteor.*, **25**, 1271–1279, doi:10.1175/1520-0450(1986)025<1271:COSLWI>2.0.CO;2.

Hogan, R. J., P. R. Field, A. J. Illingworth, R. J. Cotton, and T. W. Choularton, 2002: Properties of embedded convection in warm-frontal mixed-phase cloud from aircraft and polarimetric radar. *Quart. J. Roy. Meteor. Soc.*, **128**, 451–476, doi:10.1256/003590002321042054.

Houze, R. A., 1977: Structure and dynamics of a tropical squall–line system. *Mon. Wea. Rev.*, **105**, 1540–1567, doi:10.1175/1520-0493(1977)105<1540:SADOAT>2.0.CO;2.

Houze, R. A., 2004: Mesoscale convective systems. *Rev. Geophys.*, **42**, doi:10.1029/2004RG000150. http://dx.doi.org/10.1029/2004RG000150.

Houze, R. A., 2014: *Cloud Dynamics (2nd Edition)*. Academic Press, 496 pp.

Houze, R. A., and S. Medina, 2005: Turbulence as a mechanism for orographic precipitation enhancement. *J. Atmos. Sci.*, **62**, 3599–3623, doi:10.1175/JAS3555.1.

Houze, R. A., B. F. Smull, and P. Dodge, 1990: Mesoscale organization of springtime rainstorms in Oklahoma. *Mon. Wea. Rev.*, **118**, 613–654, doi:10.1175/1520-0493(1990)118<0613:MOOSRI>2.0.CO;2.

Houze, R. A., M. I. Biggerstaff, S. A. Rutledge, and B. F. Smull, 1989: Interpretation of Doppler weather radar displays of midlatitude mesoscale convective systems. *Bull. Amer. Meteor. Soc.*, **70**, 608–619, doi:10.1175/1520-0477(1989)070<0608:IODWRD>2.0.CO;2.

Hovmöller, E., 1949: The trough-and-ridge diagram. *Tellus*, **1**, 2, 62–66, doi:10.1111/j.2153-3490.1949.tb01260.x.

Jaffrain, J., and A. Berne, 2011: Experimental quantification of the sampling uncertainty associated with measurements from PARSIVEL disdrometers. *J. Hydrometeor.*, **12**, 352–370, doi:10.1175/2010JHM1244.1.

Jing, X., and B. Geerts, 2015: Dual-polarization radar data analysis of the impact of ground-based glaciogenic seeding on winter orographic clouds. Part II: Convective clouds. *J. Appl. Meteor. Climatol.*, **54**, 2099–2117, doi:10.1175/JAMC-D-15-0056.1.

Jing, X., B. Geerts, K. Friedrich, and B. Pokharel, 2015: Dual-polarization radar data analysis of the impact of ground-based glaciogenic seeding on winter orographic clouds. Part I: Mostly stratiform clouds. *J. Appl. Meteor. Climatol.*, **54**, 1944–1969, doi:10.1175/JAMC-D-14-0257.1.

Kalogiros, J., M. N. Anagnostou, E. N. Anagnostou, M. Montopoli, E. Picciotti, and F. S. Marzano, 2013: Optimum estimation of rain microphysical parameters from X-band dual-polarization radar observables. *IEEE Geosci. Remote Sens.*, **51**, 3063–3076, doi:10.1109/TGRS.2012.2211606.

Kalogiros, J., M. N. Anagnostou, E. N. Anagnostou, M. Montopoli, E. Picciotti, and F. S. Marzano, 2014: Evaluation of a new polarimetric algorithm for rain-path attenuation correction of X-band radar observations against disdrometer. *IEEE Geosci. Remote Sens.*, **52**, 1369–1380, doi:10.1109/TGRS.2013.2250979.

Kennedy, P. C., and S. A. Rutledge, 2011: S-band dual-polarization radar observations of winter storms. *J. Appl. Meteor. Climatol.*, **50**, 844–858, doi:10.1175/2010JAMC2558.1.

Kim, J., D. Waliser, P. Neiman, B. Guan, J.-M. Ryoo, and G. Wick, 2013: Effects of atmospheric river landfalls on the cold season precipitation in California. *Climate Dynamics*, **40**, 465–474, doi:10.1007/s00382-012-1322-3.

Kingsmill, D. E., P. J. Neiman, B. J. Moore, M. Hughes, S. E. Yuter, and F. M. Ralph, 2013: Kinematic and thermodynamic structures of Sierra barrier jets and overrunning atmospheric rivers during a landfalling winter storm in northern California. *Mon. Wea. Rev.*, **141**, 2015–2036, doi:10.1175/MWR-D-12-00277.1.

Kirshbaum, D. J., G. H. Bryan, R. Rotunno, and D. R. Durran, 2007: The triggering of orographic rainbands by small-scale topography. *J. Atmos. Sci.*, **64**, 1530–1549, doi:10.1175/JAS3924.1.

Kumjian, M. R., S. A. Rutledge, R. M. Rasmussen, P. C. Kennedy, and M. Dixon, 2014: High-resolution polarimetric radar observations of snow-generating

cells. *J. Appl. Meteor. Climatol.*, **53**, 1636–1658, doi:10.1175/JAMC-D-13-0312.1.

Lamb, D., and J. Verlinde, 2011: *Physics and Chemistry of Clouds*. Cambridge University Press, 584 pp.

Lee, W.-C., P. Dodge, F. D. Marks, and P. H. Hildebrand, 1994: Mapping of airborne Doppler radar data. *J. Atmos. Oceanic Technol.*, **11**, 572–578, doi:10.1175/1520-0426(1994)011<0572:MOADRD>2.0.CO;2.

Letkewicz, C. E., and M. D. Parker, 2010: Forecasting the maintenance of mesoscale convective systems crossing the Appalachian Mountains. *Wea. Forecasting*, **25**, 1179–1195, doi:10.1175/2010WAF2222379.1.

Letkewicz, C. E., and M. D. Parker, 2011: Impact of environmental variations on simulated squall lines interacting with terrain. *Mon. Wea. Rev.*, **139**, 3163–3183, doi:10.1175/2011MWR3635.1.

Locatelli, J. D., and P. V. Hobbs, 1974: Fall speeds and masses of solid precipitation particles. *J. Geophys. Res.*, **79**, 2185–2197, doi:10.1029/JC079i015p02185.

Loescher, K. A., G. S. Young, B. A. Colle, and N. S. Winstead, 2006: Climatology of barrier jets along the Alaskan coast. Part I: Spatial and temporal distributions. *Mon. Wea. Rev.*, **134**, 437–453, doi:10.1175/MWR3037.1.

Löffler-Mang, M., M. Kunz, and W. Schmid, 1999: On the performance of a low-cost K-band Doppler radar for quantitative rain measurements. *J. Atmos. Oceanic Technol.*, **16**, 379–387, doi:10.1175/1520-0426(1999)016<0379:OTPOAL>2.0.CO;2.

Maahn, M., and P. Kollias, 2012: Improved Micro Rain Radar snow measurements using Doppler spectra post-processing. *Atmos. Meas. Tech.*, **5**, 2661–2673, doi:10.5194/amt-5-2661-2012.

MacCready, P. B., 1964: Standardization of gustiness values from aircraft. *J. Appl. Meteor.*, **3**, 439–449, doi:10.1175/1520-0450(1964)003<0439:SOGVFA>2.0.CO;2.

Mahoney, K., and Coauthors, 2016: Understanding the role of atmospheric rivers in heavy precipitation in the southeast United States. *Mon. Wea. Rev.*, **144**, 1617–1632, doi:10.1175/MWR-D-15-0279.1.

Marwitz, J. D., 1983: The kinematics of orographic airflow during Sierra storms. *J. Atmos. Sci.*, **40**, 1218–1227, doi:10.1175/1520-0469(1983)040<1218:TKOOAD>2.0.CO;2.

Medina, S., and R. A. Houze, 2003: Air motions and precipitation growth in Alpine storms. *Quart. J. Roy. Meteor. Soc.*, **129**, 345–371, doi:10.1256/qj.02.13.

Medina, S., and R. A. Houze, 2015: Small-scale precipitation elements in midlatitude cyclones crossing the California Sierra Nevada. *Mon. Wea. Rev.*, **143**, 2842–2870, doi:10.1175/MWR-D-14-00124.1.

Medina, S., B. F. Smull, R. A. Houze, and M. Steiner, 2005: Cross-barrier flow during orographic precipitation events: Results from MAP and IMPROVE. *J. Atmos. Sci.*, **62**, 3580–3598, doi:10.1175/JAS3554.1.

Miller, D. K., D. Hotz, J. Winton, and L. Stewart, 2018: Investigation of atmospheric rivers impacting the Pigeon River Basin of the Southern Appalachian Mountains. *Wea. Forecasting*, **33**, 283–299, doi:10.1175/WAF-D-17-0060.1.

Moisseev, D., E. Saltikoff, and M. Leskinen, 2009: Dual-Polarization Weather Radar Observations of Snow Growth Processes. *34th Conf. on Radar Meteor.*, Williamsburg, VA, Amer. Meteor. Soc., 13B.2. [Available online at https://ams.confex.com/ams/pdfpapers/156123.pdf]

Moore, B. J., K. M. Mahoney, E. M. Sukovich, R. Cifelli, and T. M. Hamill, 2015: Climatology and environmental characteristics of extreme precipitation events in the southeastern United States. *Mon. Wea. Rev.*, **143**, 718–741, doi:10.1175/MWR-D-14-00065.1.

Moore, B. J., P. J. Neiman, F. M. Ralph, and F. E. Barthold, 2012: Physical processes associated with heavy flooding rainfall in Nashville, Tennessee, and vicinity during 1–2 May 2010: The role of an atmospheric river and mesoscale convective systems. *Mon. Wea. Rev.*, **140**, 358–378, doi:10.1175/MWR-D-11-00126.1.

Neiman, P. J., and Coauthors, 2017: An Analysis of Coordinated Observations from NOAA's Ronald H. Brown Ship and G-IV Aircraft in a Landfalling Atmospheric River over the North Pacific during CalWater-2015. *Mon. Wea. Rev.*, **145**, 3647–3669, doi:10.1175/MWR-D-17-0055.1.

Neiman, P. J., B. J. Moore, A. B. White, G. A. Wick, J. Aikins, D. L. Jackson, J. R. Spackman, and F. M. Ralph, 2016: An airborne and ground-based study of a

long-lived and intense atmospheric river with mesoscale frontal waves impacting California during CalWater-2014. *Mon. Wea. Rev.*, **144**, 1115–1144, doi:10.1175/MWR-D-15-0319.1.

Neiman, P. J., F. M. Ralph, A. B. White, D. E. Kingsmill, and P. O. G. Persson, 2002: The statistical relationship between upslope flow and rainfall in California's Coastal Mountains: Observations during CALJET. *Mon. Wea. Rev.*, **130**, 1468–1492, doi:10.1175/1520-0493(2002)130<1468:TSRBUF>2.0.CO;2.

Neiman, P. J., F. M. Ralph, A. B. White, D. E. Kingsmill, and P. O. G. Persson, 2002: The statistical relationship between upslope flow and rainfall in California's Coastal Mountains: Observations during CALJET. *Mon. Wea. Rev.*, **130**, 1468–1492, doi:10.1175/1520-0493(2002)130<1468:TSRBUF>2.0.CO;2.

Neiman, P. J., F. M. Ralph, G. A. Wick, J. D. Lundquist, and M. D. Dettinger, 2008: Meteorological Characteristics and Overland Precipitation Impacts of Atmospheric Rivers Affecting the West Coast of North America Based on Eight Years of SSM/I Satellite Observations. *J. Hydrometeor.*, **9**, 22–47, doi:10.1175/2007JHM855.1.

Neiman, P. J., F. M. Ralph, P. O. G. Persson, A. B. White, D. P. Jorgensen, and D. E. Kingsmill, 2004: Modification of fronts and precipitation by coastal blocking during an intense landfalling winter storm in southern California: Observations during CALJET. *Mon. Wea. Rev.*, **132**, 242–273, doi:10.1175/1520-0493(2004)132<0242:MOFAPB>2.0.CO;2.

Neiman, P. J., L. J. Schick, F. M. Ralph, M. Hughes, and G. A. Wick, 2011: Flooding in western Washington: The connection to atmospheric rivers. *J. Hydrometeor.*, **12**, 1337–1358, doi:10.1175/2011JHM1358.1.

Neiman, P. J., M. Hughes, B. J. Moore, F. M. Ralph, and E. M. Sukovich, 2013: Sierra barrier jets, atmospheric rivers, and precipitation characteristics in northern California: A composite perspective based on a network of wind profilers. *Mon. Wea. Rev.*, **141**, 4211–4233, doi:10.1175/MWR-D-13-00112.1.

Ogura, Y., and M.-T. Liou, 1980: The structure of a midlatitude squall line: A case study. *J. Atmos. Sci.*, **37**, 553–567, doi:10.1175/1520-0469(1980)037<0553:TSOAMS>2.0.CO;2.

Olson, J. B., and B. A. Colle, 2009: Three-dimensional idealized simulations of barrier jets along the southeast coast of Alaska. *Mon. Wea. Rev.*, **137**, 391–413, doi:10.1175/2008MWR2480.1.

Olson, J. B., B. A. Colle, N. A. Bond, and N. Winstead, 2007: A comparison of two coastal barrier jet events along the southeast Alaskan coast during the SARJET field experiment. *Mon. Wea. Rev.*, **135**, 3642–3663, doi:10.1175/MWR3448.E1.

Overland, J. E., and N. A. Bond, 1995: Observations and scale analysis of coastal wind jets. *Mon. Wea. Rev.*, **123**, 2934–2941, doi:10.1175/1520-0493(1995)123<2934:OASAOC>2.0.CO;2.

Parker, M. D., and D. A. Ahijevych, 2007: Convective episodes in the east-central United States. *Mon. Wea. Rev.*, **135**, 3707–3727, doi:10.1175/2007MWR2098.1.

Parker, M. D., and R. H. Johnson, 2000: Organizational modes of midlatitude mesoscale convective systems. *Mon. Wea. Rev.*, **128**, 3413–3436, doi:10.1175/1520-0493(2001)129<3413:OMOMMC>2.0.CO;2.

Peters, G., B. Fischer, and T. Andersson, 2002: Rain observations with a vertically looking Micro Rain Radar (MRR). *Boreal Env. Res.*, **7**, 353-362.

Peters, G., B. Fischer, H. Münster, M. Clemens, and A. Wagner, 2005: Profiles of raindrop size distributions as retrieved by microrain radars. *J. Appl. Meteor.*, **44**, 1930–1949, doi:10.1175/JAM2316.1.

Petersen, W. A., D. B. Wolff, J. Wang, and A. Tokay, 2016: GPM Ground Validation Met One Rain Gauge Pairs IPHEX V2. NASA Global Hydrology Center Distributed Active Archive Center, accessed 21 June 2016, http://dx.doi.org/10.5067/GPMGV/IPHEX/GAUGES/DATA201.

Pippitt, J. L., D. A. Marks, and D. B. Wolff, 2013: Dual polarimetric quality control for NASA's Global Precipitation Measurement (GPM) mission ground validation program. *36th Conf. on Radar Meteorology*, Breckenridge, CO, Amer. Meteor. Soc., 235, https://ams.confex.com/ams/36Radar/webprogram/Paper228522.html.

Plummer, D. M., G. M. McFarquhar, R. M. Rauber, B. F. Jewett, and D. C. Leon, 2014: Structure and statistical analysis of the microphysical properties of

generating cells in the comma head region of continental winter cyclones. *J. Atmos. Sci.*, **71**, 4181–4203, doi:10.1175/JAS-D-14-0100.1.

Pokharel, B., B. Geerts, and X. Jing, 2014a: The impact of ground-based glaciogenic seeding on orographic clouds and precipitation: A multisensor case study. *J. Appl. Meteor. Climatol.*, **53**, 890–909, doi:10.1175/JAMC-D-13-0290.1.

Pokharel, B., B. Geerts, and X. Jing, 2015: The impact of ground-based glaciogenic seeding on clouds and precipitation over mountains: A case study of a shallow orographic cloud with large supercooled droplets. *J. Geophys. Res. Atmos.*, **120**, 6056–6079, doi:10.1002/2014JD022693.

Pokharel, B., B. Geerts, X. Jing, K. Friedrich, J. Aikins, D. Breed, R. Rasmussen, and A. Huggins, 2014b: The impact of ground-based glaciogenic seeding on clouds and precipitation over mountains: A multi-sensor case study of shallow precipitating orographic cumuli. *Atmos. Res.*, **147-148**, 162–182, doi:10.1016/j.atmosres.2014.05.014.

PRISM Climate Group, 2017: 30-yr Normal Precipitation. Oregon State University, http://www.prism.oregonstate.edu/normals/.

Przybylinski, R. W., 1995: The Bow Echo: Observations, numerical simulations, and severe weather detection methods. *Wea. Forecasting*, **10**, 203–218, doi:10.1175/1520-0434(1995)010<0203:TBEONS>2.0.CO;2.

Ralph, F. M., and Coauthors, 2016: CalWater field studies designed to quantify the roles of atmospheric rivers and aerosols in modulating U.S. West Coast precipitation in a changing climate. *Bull. Amer. Meteor. Soc.*, **97**, 1209–1228, doi:10.1175/BAMS-D-14-00043.1.

Ralph, F. M., and M. D. Dettinger, 2012: Historical and National Perspectives on Extreme West Coast Precipitation Associated with Atmospheric Rivers during December 2010. *Bull. Amer. Meteor. Soc.*, **93**, 783–790, doi:10.1175/BAMS-D-11-00188.1.

Ralph, F. M., M. D. Dettinger, M. M. Cairns, T. J. Galarneau, and J. Eylander, 2018: Defining "Atmospheric River": How the Glossary of Meteorology helped resolve a debate. *Bull. Amer. Meteor. Soc.*, **99**, 837–839, doi:10.1175/BAMS-D-17-0157.1.

Ralph, F. M., P. J. Neiman, and G. A. Wick, 2004: Satellite and CALJET aircraft observations of atmospheric rivers over the eastern North Pacific Ocean

during the winter of 1997/98. *Mon. Wea. Rev.*, **132**, 1721–1745, doi:10.1175/1520-0493(2004)132<1721:SACAOO>2.0.CO;2.

Ralph, F. M., P. J. Neiman, G. A. Wick, S. I. Gutman, M. D. Dettinger, D. R. Cayan, and A. B. White, 2006: Flooding on California's Russian River: Role of atmospheric rivers. *Geophys. Res. Lett.*, **33**, L13801, doi:10.1029/2006GL026689.

Rauber, R. M., 1987: Characteristics of cloud ice and precipitation during wintertime storms over the mountains of northern Colorado. *J. Climate Appl. Meteor.*, **26**, 488–524, doi:10.1175/1520-0450(1987)026<0488:COCIAP>2.0.CO;2.

Rauber, R. M., 1992: Microphysical structure and evolution of a central Sierra Nevada orographic cloud system. *J. Appl. Meteor.*, **31**, 3–24, doi:10.1175/1520-0450(1992)031<0003:MSAEOA>2.0.CO;2.

Rauber, R. M., and L. O. Grant, 1986: The characteristics and distribution of cloud water over the mountains of northern Colorado during wintertime storms. Part II: Spatial distribution and microphysical characteristics. *J. Climate Appl. Meteor.*, **25**, 489–504, doi:10.1175/1520-0450(1986)025<0489:TCADOC>2.0.CO;2.

Rollenbeck, R., J. Bendix, P. Fabian, J. Boy, W. Wilcke, H. Dalitz, M. Oesker, and P. Emck, 2007: Comparison of different techniques for the measurement of precipitation in tropical montane rain forest regions. *J. Atmos. Oceanic Technol.*, **24**, 156–168, doi:10.1175/JTECH1970.1.

Rosenkranz, P. W., 1998: Water vapor microwave continuum absorption: A comparison of measurements and models. *Radio Sci.*, **33**, 919–928, doi:10.1029/98RS01182.

Rosenow, A. A., D. M. Plummer, R. M. Rauber, G. M. McFarquhar, B. F. Jewett, and D. Leon, 2014: Vertical velocity and physical structure of generating cells and convection in the comma head region of continental winter cyclones. *J. Atmos. Sci.*, **71**, 1538–1558, doi:10.1175/JAS-D-13-0249.1.

Rotunno, R., and R. A. Houze, 2007: Lessons on orographic precipitation from the Mesoscale Alpine Programme. *Quart. J. Roy. Meteor. Soc.*, **133**, 811–830, doi:10.1002/qj.67.

Rotunno, R., J. B. Klemp, and M. L. Weisman, 1988: A theory for strong, long-lived squall lines. *J. Atmos. Sci.*, **45**, 463–485, doi:10.1175/1520-0469(1988)045<0463:ATFSLL>2.0.CO;2.

Ryzhkov, A. V., and D. S. Zrnić, 1998: Discrimination between rain and snow with a polarimetric radar. *J. Appl. Meteor.*, **37**, 1228–1240, doi:10.1175/1520-0450(1998)037<1228:DBRASW>2.0.CO;2.

Saleeby, S. M., W. R. Cotton, and J. D. Fuller, 2011: The cumulative impact of cloud droplet nucleating aerosols on orographic snowfall in Colorado. *J. Appl. Meteor. Climatol.*, **50**, 604–625, doi:10.1175/2010JAMC2594.1.

Saleeby, S. M., W. R. Cotton, D. Lowenthal, and J. Messina, 2013: Aerosol impacts on the microphysical growth processes of orographic snowfall. *J. Appl. Meteor. Climatol.*, **52**, 834–852, doi:10.1175/JAMC-D-12-0193.1.

Schneebeli, M., N. Dawes, M. Lehning, and A. Berne, 2013: High-resolution vertical profiles of X-band polarimetric radar observables during snowfall in the Swiss Alps. *J. Appl. Meteor. Climatol.*, **52**, 378–394, doi:10.1175/JAMC-D-12-015.1.

Smith, B. L., S. E. Yuter, P. J. Neiman, and D. E. Kingsmill, 2010: Water vapor fluxes and orographic precipitation over northern California associated with a landfalling atmospheric river. *Mon. Wea. Rev.*, **138**, 74–100, doi:10.1175/2009MWR2939.1.

Smith, R. B., and Coauthors, 2012: Orographic precipitation in the tropics: The Dominica Experiment. *Bull. Amer. Meteor. Soc.*, **93**, 1567–1579, doi:10.1175/BAMS-D-11-00194.1.

Smull, B. F., and R. A. Houze, 1987: Rear inflow in squall lines with trailing stratiform precipitation. *Mon. Wea. Rev.*, **115**, 2869–2889, doi:10.1175/1520-0493(1987)115<2869:RIISLW>2.0.CO;2.

Solheim, F., J. Godwin, and R. Ware, 1998a: Passive ground-based remote sensing of atmospheric temperature, water vapor, and cloud liquid water profiles by a frequency synthesized microwave radiometer, *Met. Z.*, **7**, 370-376.

Solheim, F., J. Godwin, E. Westwater, Y. Han, S. Keihm, K. Marsh, and R. Ware, 1998b: Radiometric profiling of temperature, water vapor and cloud liquid water using various inversion methods, *Radio Sci.*, **33**, 393-404.

Stewart, I. T., D. R. Cayan, and M. D. Dettinger, 2005: Changes toward earlier streamflow timing across western North America. *J. Climate*, **18**, 1136–1155, doi:10.1175/JCLI3321.1.

Strauss, L., S. Serafin, S. Haimov, and V. Grubišić, 2015: Turbulence in breaking mountain waves and atmospheric rotors estimated from airborne in situ and Doppler radar measurements. *Quart. J. Roy. Meteor. Soc.*, **141**, 3207–3225, doi:10.1002/qj.2604.

Tao, J., D. Wu, J. Gourley, S. Q. Zhang, W. Crow, C. Peters-Lidard, and A. P. Barros, 2016: Operational hydrological forecasting during the IPHEx-IOP campaign – Meet the challenge. *J. Hydrol.*, **541, Part A**, 434–456, doi:10.1016/j.jhydrol.2016.02.019.

Teng, J.-H., C.-S. Chen, T.-C. C. Wang, and Y.-L. Chen, 2000: Orographic effects on a squall line system over Taiwan. *Mon. Wea. Rev.*, **128**, 1123–1138, doi:10.1175/1520-0493(2000)128<1123:OEOASL>2.0.CO;2.

Tessendorf, S. A., J. French, K. Friedrich, B. Geerts, R. M. Rauber, R. M. Rasmussen, L. Xue, K. Ikeda, D. R. Blestrud, M. L. Kunkel, S. Parkinson, J. R. Snider, J. Aikins, S. Faber, A. Majewski, C. Grasmick, A. Janiszeski, A. Springer, C. Weeks, D. J. Serke, and R. Bruintjes, 2018: Transformational approach to winter orographic weather modification research: The SNOWIE Project. Submitted to *The Bulletin of the American Meteorological Society*, March 2018.

Testud, J., S. Oury, R. A. Black, P. Amayenc, and X. Dou, 2001: The concept of "normalized" distribution to describe raindrop spectra: A tool for cloud physics and cloud remote sensing. *J. Appl. Meteor.*, **40**, 1118–1140, doi:10.1175/1520-0450(2001)040<1118:TCONDT>2.0.CO;2.

Tokay, A., D. B. Wolff, and W. A. Petersen, 2014: Evaluation of the new version of the laser-optical disdrometer, OTT Parsivel2. *J. Atmos. Oceanic Technol.*, **31**, 1276–1288, doi:10.1175/JTECH-D-13-00174.1.

Tokay, A., P. G. Bashor, and V. L. McDowell, 2010: Comparison of rain gauge measurements in the Mid-Atlantic region. *J. Hydrometeor.*, **11**, 553–565, doi:10.1175/2009JHM1137.1.

Tokay, A., P. Hartmann, A. Battaglia, K. S. Gage, W. L. Clark, and C. R. Williams, 2009: A field study of reflectivity and Z–R relations using vertically pointing

radars and disdrometers. *J. Atmos. Oceanic Technol.*, **26**, 1120–1134, doi:10.1175/2008JTECHA1163.1.

Tokay, A., W. A. Petersen, P. Gatlin, and M. Wingo, 2013: Comparison of raindrop size distribution measurements by collocated disdrometers. *J. Atmos. Oceanic Technol.*, **30**, 1672–1690, doi:10.1175/JTECH-D-12-00163.1.

Trapp, R. J., 2013: *Mesoscale-Convective Processes in the Atmosphere*. Cambridge University Press, Cambridge, 377 pp.

Trivej, P., and B. Stevens, 2010: The echo size distribution of precipitating shallow cumuli. *J. Atmos. Sci.*, **67**, 788–804, doi:10.1175/2009JAS3178.1.

Trujillo, E., and N. P. Molotch, 2014: Snowpack regimes of the western United States. *Water Resour. Res.*, **50**, 5611–5623, doi:10.1002/2013WR014753.

Wang, Z., and Coauthors, 2012: Single aircraft integration of remote sensing and in situ sampling for the study of cloud microphysics and dynamics. *Bull. Amer. Meteor. Soc.*, **93**, 653–668, doi:10.1175/BAMS-D-11-00044.1.

Weisman, M. L., and R. Rotunno, 2004: "A theory for strong long-lived squall lines" revisited. *J. Atmos. Sci.*, **61**, 361–382, doi:10.1175/1520-0469(2004)061<0361:ATFSLS>2.0.CO;2.

Wetzel, M., and Coauthors, 2004: Mesoscale snowfall prediction and verification in mountainous terrain. *Wea. Forecasting*, **19**, 806–828, doi:10.1175/1520-0434(2004)019<0806:MSPAVI>2.0.CO;2.

White, A. B., and Coauthors, 2013: A twenty-first-century California observing network for monitoring extreme weather events. *J. Atmos. Oceanic Technol.*, **30**, 1585–1603, doi:10.1175/JTECH-D-12-00217.1.

Wick, G. A., P. J. Neiman, and F. M. Ralph, 2013a: Description and validation of an automated objective technique for identification and characterization of the integrated water vapor signature of atmospheric rivers. *IEEE Trans. Geosci. Remote Sens.*, **51**, 2166–2176, doi:10.1109/TGRS.2012.2211024.

Wick, G. A., P. J. Neiman, F. M. Ralph, and T. M. Hamill, 2013b: Evaluation of forecasts of the water vapor signature of atmospheric rivers in operational numerical weather prediction models. *Wea. Forecasting*, **28**, 1337–1352, doi:10.1175/WAF-D-13-00025.1.

Wolff, D. and D. Marks, 2015: GPM ground validation NASA S-band dual polarimetric (NPOL) Doppler radar IPHEx, version 1. NASA EOSDIS Global Hydrology Resource Center Distributed Active Archive Center, accessed 06 May 2015, http://dx.doi.org/10.5067/GPMGV/IPHEX/NPOL/DATA101.

Wurman, J., 2001: The DOW mobile multiple-Doppler network. Preprints, *30th Int. Conf. on Radar Meteor.*, Munich, Germany, Amer. Meteor. Soc., 95–97.

Yu, C.-K., and B. F. Smull, 2000: Airborne Doppler observations of a landfalling cold front upstream of steep coastal orography. *Mon. Wea. Rev.*, **128**, 1577–1603, doi:10.1175/1520-0493(2000)128<1577:ADOOAL>2.0.CO;2.

Yu, C.-K., and N. A. Bond, 2002: Airborne Doppler observations of a cold front in the vicinity of Vancouver Island. *Mon. Wea. Rev.*, **130**, 2692–2708, doi:10.1175/1520-0493(2002)130<2692:ADOOAC>2.0.CO;2.

Yuter, S. E., and R. A. Houze, 1995: Three-dimensional kinematic and microphysical evolution of Florida cumulonimbus. Part II: Frequency distributions of vertical velocity, reflectivity, and differential reflectivity. *Mon. Wea. Rev.*, **123**, 1941–1963, doi:10.1175/1520-0493(1995)123<1941:TDKAME>2.0.CO;2.

Zhu, Y., and R. E. Newell, 1998: A proposed algorithm for moisture fluxes from atmospheric rivers. *Mon. Wea. Rev.*, **126**, 725–735, doi:10.1175/1520-0493(1998)126<0725:APAFMF>2.0.CO;2.